Skolkovo Institute of Science and Technology

Dynamics of exceptional states in many-body systems

Doctoral Thesis
by

Igor Ermakov

DOCTORAL PROGRAM IN PHYSICS

Supervisor
Professor Dr. Boris V. Fine
Supervisor
Senior Research Scientist Dr. Oleg Lychkovskiy

Moscow — 2022

I hereby declare that the work presented in this thesis was carried out by myself at Skolkovo Institute of Science and Technology, Moscow, except where due acknowledgement is made, and has not been submitted for any other degree.

Candidate (Igor Ermakov)

Supervisors (Professor Dr. Boris V. Fine and Senior Research Scientist Dr. Oleg Lychkovskiy)

Abstract

In this thesis, we study the question of thermalization dynamics in classical and quantum many-body systems. Specifically, we investigate the dynamics starting with certain "exceptional" nonequilibrium states. These states are exceptional for two reasons: First, they correspond to a subset of initial conditions of measure zero. Second, their thermalization patterns are noticeably different from that of typical states.

As the first class of exceptional states, we study the stability of many-body periodic trajectories in spin chains and the quantum dynamics of the corresponding initial states. In particular, we consider translationally invariant chains of interacting spins in both quantum and classical cases. As initial conditions, we consider all spins pointed along the same direction. Despite their simple character, such initial conditions lead to a number of interesting equilibration properties. Namely, classical periodic trajectories may exhibit topologically different regimes of motion, and some of them are stable for relatively large system sizes. Furthermore, the stability of a periodic trajectory has highly non-trivial dependence on the system's size. We also uncover the existence of time quasicrystals where the periodic trajectory spontaneously transitions to quasiperiodic time dynamics with lowered translational symmetry. On the quantum side of the aforementioned problem, we discover remnants of periodic classical dynamics in chains of spins-1 and higher. These remnants manifest themselves as "finite-size quantum scars" – the eigenstates in finite systems with anomalously low entanglement entropy. These eigenstates are responsible for the slowed relaxation of initial conditions. We also introduce "quantum separatrix", which by analogy with classical separatrix distinguishes between two topologically different regimes of motion.

As a second class of exceptional states, we introduce Almost Complete Reviving states. Specifically, we consider a lattice of spins 1/2 and demonstrate how to construct a quantum state such that a given spin 1/2 is maximally polarized initially and then exhibits an almost complete recovery of the initial polarization at a later predetermined moment of time. Experimental observation of such revivals may be

utilized to benchmark quantum simulators. We further propose to utilize these revivals for delayed disclosure of a secret.

As a third class of exceptional states, we study a heavy particle interacting with the gas of light particles. It is believed that, in such a setup, the stationary reduced density matrix of a heavy particle should be classical-like due to the interaction with the gas. Therefore, if a heavy particle is initially in a superposition of quantum states localized around two distant points, such an initial state is expected to be highly unstable to decoherence. Nevertheless, we discover that there is a measure-zero subset of eigenstates in the middle of the spectrum corresponding to a heavy particle being in a highly nonclassical state of the kind described above.

Publications

1. Igor Ermakov and Boris V Fine. Almost complete revivals in quantum many-body systems. *Physical Review A*, 104(5):L050202, 2021
2. Ivan V Dudinets, Igor Ermakov, and Oleg Lychkovskiy. Testing eigenstate decoherence hypothesis in a model of collisional decoherence. *EPL (Europhysics Letters)*, 134(6):60004, 2021
3. Igor Ermakov. Generalized almost complete revivals in quantum spin chains. *arXiv preprint arXiv:2205.05584*, 2022 (Accepted to Lobachevsky Journal of Mathematics)

Acknowledgments

My journey to achieving a Ph.D. degree was not accomplished in isolation. The efforts of dozens of people helped me during my studies to become a physicist, and it would be impossible to list them all here. Nevertheless, I am grateful to everyone who played a role in this story.

First, I would like to thank my parents, Tatyana Parfyonova and Vladimir Parfyonov, for their love, care, and support. I especially want to thank my mother for her wise decision to send me to Central School 208 in Ekaterinburg. During my happy time in this school, I had an opportunity to discover and nurture my growing desire to acquire knowledge. My mother also supported me during the toughest times of my life. Without her love and support, I would not have been able to finish my education successfully.

I am incredibly grateful to Professor Dr. Boris V. Fine, for his supervision of the present thesis. Working with Boris over the last four years was a pleasure and honor, and I have gained a significant amount of theoretical knowledge and honed my practical skills under his patient mentorship. I'm especially thankful to Boris for teaching me to address my physical statements more critically.

I am also very grateful to my co-supervisor Oleg Lychkovsky. Oleg taught me the crucial things about quantum mechanics of many-body systems. We had a very fruitful time working and exploring physics together. It deserves mentioning that Oleg was the person who introduced me to Boris and who gave me the idea to join Skoltech, back in 2017.

I also thank my other collaborators and friends from NYU Shanghai: Tim Byrnes, Chandrashekar Radhakrishnan and Lev Birman. Tim was my supervisor there during 2016-2018. I have acquired a new vision of physics and life thanks to Tim. Chandrashekar Radhakrishnan with whom I had the pleasure to work for his friendship and kindness. Lev Birman, who, among other things, helped me edit my application to Skoltech, for a great time and exciting discussions. I am also indebted to Nikolay Bogoliubov from the Saint-Petersburg branch of Steklov's Institute of Mathematics for his productive collaboration and for teaching me the

Quantum Inverse Scattering method.

I'm grateful to my Ph.D. Defense Jury Chair professor Jacob Biamonte and to my Ph.D Defense Jury Members: Vladimir Antonov, Maksym Serbin, Vladimir Gritsev, Anton Trushechkin, Sergey Filippov, and Yevgeny Bar Lev, for their careful reading of my thesis and valuable comments. I sincerely appreciate the time these people devoted to my thesis.

Last but certainly not least, I would like to express my gratitude to my friends who helped me along the way. My girlfriend Anna Lugovaya for her love, care, and patience. My friends from Ural State University, Boris Latosh, and Polina Matveyeva, for great memories and countless discussions, ranging from physics to art. My friend James Oglesby for his assistance with some of the finer points of English. My two best friends of all time, Arseny Lukanin and Sergey Adamov, just because you guys exist. There are many more people I want to mention here; unfortunately, this is impossible due to the length constraints.

I firmly believe that studying physics and being paid for it is a privilege, and I consider myself very fortunate to have had the opportunity to experience this privilege. Therefore, I would like to thank Skolkovo Institute of Science and Technology, Moscow Steklov's Institute of Mathematics and Moscow Institute of Physics and Technology for their substantial material support.

The work was funded by the Ministry of Science and Higher Education of the Russian Federation (grant number 075-15-2020-788); The Russian Science Foundation under the grant N^{o} 17-12-01587; Basis Foundation (Grant No. 18-1-5-19-1).

Contents

List of Figures

Chapter 1

Introduction

1.1 Dynamic thermalization

It is a fundamental thermodynamic assumption that an isolated many-body system must reach the stationary state of thermal equilibrium [5]. The process of reaching thermal equilibrium can be referred to as thermalization. In reality, we observe many out-of-equilibrium systems such as stars, living cells, synthetic quantum systems, or even glacé coffee. From these observations, two questions naturally arise: when will the system reach equilibrium, and what happens during thermalization? Furthermore, there are known many-body systems which do not thermalize at all [6–12]. This raises another question about applicability limits of the thermalization assumption.

Dynamic thermalization research addresses these questions by studying the dynamics of non-equilibrium states in many-body systems. Of particular interest are systems resisting thermalization in one way or another. A number of physical mechanisms are responsible for suppressed thermalization in many-body systems. Understanding these mechanisms may help determine the timescales when we can or cannot expect a certain state to thermalize.

Dynamic thermalization is closely related to the ergodic hypothesis. The system is called ergodic if, during its evolution, any initial equilibrium state eventually comes arbitrarily close to every other equilibrium state with the same energy; if the above phenomena is not observed on a certain time scale, then we can state that on this particular time scale system is not ergodic.

One famous example of unexpectedly non-thermal behavior is known as Fermi-Pasta-Ulam-Tsingou problem [7]. In this problem, a vibrating non-linear string is modeled as a discrete system of nearest-neighbour coupled oscillators with non-linear interaction. Initially, the string has a simple half-sinusoidal form; thus, all but one Fourier modes have zero energy. It is expected that after some time, due to non-linear interactions, the energy of the first mode will be equally distributed over all the others Fourier modes. However, results of the simulation show “very little, if any, tendency towards equipartition of energy among the degrees of freedom” [7].

Unusual thermalization patterns were also discovered in different quantum many-body systems. One of the first experiments which induced significant interest in the thermalization of quantum many-body systems is known as ”A Quantum Newton’s cradle” [6]. In this experiment, a 1D Bose-gas of more than a hundred ^{87}Rb atoms with point-like interactions was observed to remain in the out-of-equilibrium state even after thousands of collisions. The physical mechanism responsible for such a long-living our-of-equilibrium state is rooted in quantum integrability [13–16].

1.1.1 Integrable and chaotic dynamics

Integrable systems are characterized by large amounts of conserved quantities known as integrals of motion. In classical dynamics, integrability leads to the absence of exponential sensitivity to initial conditions. In other words, if the system is integrable, the discrepancy between two initially close trajectories will not grow exponentially with time. In quantum case presence of the extensive amount of integrals of motion often leads to a scenario when dynamical wavefunction is locked in a certain sector of Hilbert space, and thus it cannot access all quantum states with given energy. There are many experimental [6, 17] and theoretical [12, 18–21] examples of suppressed thermalization in integrable systems. Let us also mention that, although observables in integrable systems, in general, do not relax to their thermal values, they can relax to the values predicted by the Generalized Gibbs Ensemble [22–24]. Integrability is not the only physical mechanism that leads to unusual thermalization properties. There are many others, such as, for example, disorder which may lead to many-body localization[25, 26], or long-range interactions which lead to glassy behaviour[9–11, 27], or constraints in Hilbert space which lead to quantum scars, which we will discuss further.

Classical interacting many-body systems, in general, are known to exhibit chaotic dynamics. We will call the system chaotic if it exhibits exponential sensitivity to small deviations of initial conditions. In particular, if the system possesses two initially close phase trajectories which exponentially diverge after some time, then the system is chaotic. To describe the divergence rate quantitatively described, the formalism of Lyapunov exponents [28, 29] is usually employed.

In the present thesis, we focus on chaotic classical and non-integrable quantum systems that, in particular, do not have disorder, long-range interactions or Hilbert space constraints.

1.1.2 Quantum systems away from integrability

Because of the uncertainty principle, the notion of chaos cannot be directly transferred from classical physics to quantum theory. Indeed, to define chaos in classical systems, we use infinitesimally close trajectories, whereas, in quantum theory, the very notion of phase-space trajectory does not make much sense. Furthermore, the evolution of wavefunction is governed by the Schrödinger equation, which is linear and thus does not exhibit exponential sensitivity to initial conditions. Simultaneously, the correspondence principle states that quantum theory shall reproduce classical physics in the limit of large quantum numbers. If the correspondence principle is correct, then there should be some quantum mechanism that would result in exponential sensitivity to initial conditions in the classical limit.

Finding manifestation of quantum chaos or even rigorously defining quantum chaoticity has been a long-standing problem that goes far beyond the scope of the present thesis. There are many ways to introduce a measure of quantum chaos, for example, by utilizing random matrix theory [30–32], or adiabatic gauge potential [33]. We will discuss some of these measures below; for now, let us focus on the dynamical properties of chaotic quantum systems.

The main dynamical feature of chaotic quantum systems is that such systems exhibit a clear tendency toward equilibration. In this regard, the dynamics of chaotic quantum systems are usually quite the different of that of integrable ones. The natural question here is: how do we know if a particular quantum system thermalizes or not? From the point of view of dynamic thermalization research, we shall look at the dynamics of out-of-equilibrium states. If every state we test reaches thermal equilibrium, we can conclude that the system is chaotic (at least for the subset of initial states we considered). Another practical way to determine whether the system is chaotic or not is to look at the system's eigenstates instead of dynamical properties.

Eigenstate thermalization hypothesis

Let us briefly recapitulate the main essence of the Eigenstate Thermalization Hypothesis (ETH) [34–39]. Let us consider some many-body system of size L described by the Hamiltonian H, with eigenstates $|E_n\rangle$, and let $\hat{O}$ be some few-body observable, eigenenergies E_n are ordered. The Hamiltonian H satisfies Eigenstate Thermalization Hypothesis (ETH) if diagonal matrix elements $O_{nn} = \langle E_n|\hat{O}|E_n\rangle$ change slowly with n, and the difference between neighbouring values $O_{nn} - O_{n-1,n-1}$ is exponentially small in L, and the off-diagonal elements $\langle E_m|\hat{O}|E_n\rangle$ are also exponentially small in L.

There is also an assumption that if the Hamiltonian H satisfies the above conditions, then it is expected that any initial out-of-equilibrium state will eventually come to thermal equilibrium. Different many-body Hamiltonians were proven to approximately satisfy the above conditions with good precision once the system size is large enough [40–42]. It also was verified that ETH is violated in integrable systems or systems close to integrability [12, 21, 43]. There are also systematic approaches to constructing counterexamples to ETH [44].

Level spacing statistics

Another practical approach that is utilized as a measure of quantum chaos is level spacing statistics. By analyzing the distribution of eigenenergies of quantum many-body systems, it is often possible to tell if the system will resist thermalization or not.

Methods based on level spacing statistics are relying on random matrix theory [30–32]. The main idea is based on the two following conjectures. First conjecture [45–47] is that if the system is chaotic, its spectrum must exhibit level repulsion, and its level statistics should be described by either Gaussian Orthogonal Ensemble (GOE), Gaussian Unitary Ensemble (GUE) or Gaussian Symplectic Ensemble (GSE). The second conjecture (Berry-Tabor conjecture) [48] is that if the system is integrable, it possesses a vast amount of integrals of motion and, therefore many uncorrelated energy levels which can cross. Thus the system's energy level statistics should be Poisson-like in most cases.

Even when exact diagonalization is numerically doable, two additional steps are required to analyze level spacing statistics correctly. The first step is to remove all the system symmetries, such as translational or reflection symmetries. Otherwise, one can confuse a chaotic spectrum with an integrable one. The second step is to perform the so-called unfolding of the spectrum by resetting eigenvalues to dimensionless values with unit mean spacing.

One statistical quantity which allows easily distinguish between chaotic and integrable spectral statistics is the so-called r-value [49, 50], which is defined as a mean value of the following quantity:

$$\tilde{r}_n = \frac{\min(s_n, s_{n-1})}{\max(s_n, s_{n-1})} = \min\left(r_n, \frac{1}{r_n}\right), \tag{1.1}$$

where $r_n = s_n/s_{n-1}$ and $s_n = E_{n+1} - E_n$, here E_n is eigenenergy. Eigenenergies E_n are supposed to be ordered and non-degenerate. The r-value itself is equal to mean value of $\tilde{r}_n$ for all n, let us denote it as $\langle r \rangle$. If the system is integrable, for large enough system size its r-value must converge to the r-value of Poisson statistics, namely $\langle r \rangle_p \simeq 0.38$. If the system is non-integrable, then depending on the symmetry its r-value should converge to r-value for either GOE $\langle r \rangle_{\text{GOE}} \simeq 0.53$, GUE $\langle r \rangle_{\text{GUE}} \simeq 0.59$ or GSE $\langle r \rangle_{\text{GSE}} \simeq 0.67$. In the present thesis, we mostly study non-integrable systems with spectral statistics similar to that of Gaussian Orthogonal Ensemble.

1.1.3 Quantum scars

Let us review one of the most recent examples of non-thermal behavior in non-integrable quantum many-body systems.

Quantum scars in billiard

To be consistent, let us first discuss regular quantum scars introduced by Heller in [4]. Quantum scars are special eigenstates of classically chaotic quantum systems characterized by probability density concentrated around classical periodic trajectories with short periods.

Historically quantum scars were introduced in chaotic billiards. If we consider eigenstates of a symmetric chaotic billiard with high quantum numbers (far from the ground state), the majority of these states are indistinguishable on the level of observables, such as probability density $|\Psi(\mathbf{r})|^2$. Indeed, from Fig. 1-1 (a), we see that probability density for a typical eigenstate is rather featureless. Examining all eigenstates shows some special eigenstates with a clearly non-uniform probability distribution. In this case, the probability distribution is concentrated around classical unstable periodic trajectories with short periods. In Fig. 1-1 (b), probability density for such scarred eigenstate is plotted as well as the corresponding classical unstable periodic orbit.

Quantum many-body scars

While billiards in which quantum scars were historically discovered possess only two degrees of freedom. There have been a series of recent discoveries of scarred eigenstates in quantum many-body systems. A notion of quantum many-body scars has been introduced in [51]. It refers to atypical non-ergodic many-body eigenstates [52] that violate the strong eigenstate thermalization hypothesis (ETH) [34, 35]. It has been demonstrated in [51] that a natural initial state of the PXP spin model has large overlaps with quantum scars, which results in long-living oscillations observed experimentally in [8].

An explosive interest in quantum many-body scars initiated in 2018 by the pub-

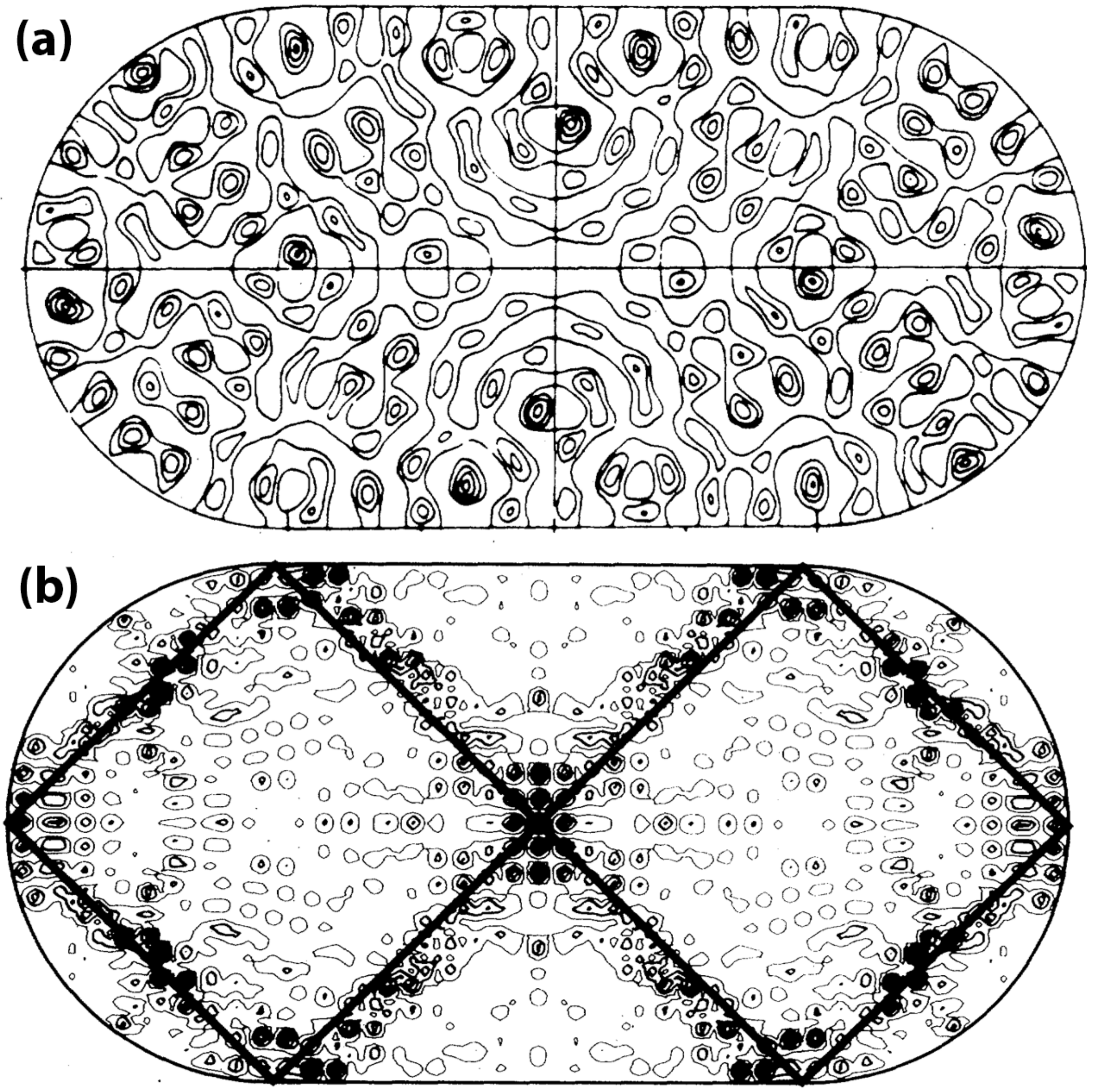

Figure 1-1: Picture from the paper [4]. Probability density $|\Psi(\mathbf{r})|^2$ in chaotic billiard. (a) Close to uniform probability density for a typical eigenstate with high quantum number. (b) Probability density corresponding to the scarred eigenstate. Solid line corresponds to the classical unstable periodic orbit.

lication [51] has led to recent discoveries of quantum many-body scars in a number of models, including kinematically constrained models [53], special configurations of spin-chains [54–56] or optical lattices [57].

Quantum many-body scars offer a very interesting mechanism of non-thermal behavior. If initially out of equilibrium state has high overlap with scarred eigenstates, it might resist thermalization since it can be practically “locked” in a small fraction of the systems’s Hilbert space. Alternatively, if the initial state does not significantly overlap with a scarred state, it is expected that such a state will quickly relax to the thermal equilibrium state as in the usual non-integrable system.

The phenomenon of quantum scars, among other things, clearly demonstrates that thermalization dynamics can be affected not only by the special properties of the system but also by the initial state itself. In other words, there are systems where some specially selected out-of-equilibrium states have significantly different thermalization behaviour than randomly selected out-of-equilibrium states.

1.1.4 Spin systems

In two chapters of the present thesis, we focus on quantum and classical spin systems. Namely, we study the dynamics of special out-of-equilibrium states in such systems. Quantum spin systems are attractive theoretical and experimental platforms for studying various many-body phenomena. Indeed, an enormous amount of theoretical research is devoted to this subject, as well as successful experimental validation of different spin models[10, 11]. A spin system can be integrable [13, 14, 58] or non-integrable [40, 59], there are spin systems which satisfy ETH with great precision [40, 41]. There are quantum spin chains exhibiting quantum many-body scars [54–56], it can exhibit glassy behaviour [11] or many-body localization [60]. It is also important that quantum spin systems have explicit classical counterparts and vice versa. This fact allows one to study quantum to classical transition.

1.2 Unusual equilibration. Role of initial states

As we discussed above, a number of physical mechanisms are responsible for unusual equilibration in many-body systems. In this project, we focus on the initial states and do not put any special restrictions on the systems under consideration. In particular, we consider Hamiltonians robustly non-integrable and possess no properties such as constraints, disorder, or long-range interactions. Initial states under consideration are, on the contrary, special. Let us now briefly preview the settings and the results to be considered in the present thesis.

1.2.1 Fully polarized spin states

First, we study polarized initial states in classical and quantum translationary invariant spin systems. Such states are natural for spin systems, but their thermalization is distinctly different from that starting from a generic initial state. By generic state, we mean states possessing a degree of randomness in initial spin orientation in classical case and thermal states in quantum one.

In the case of classical dynamics, our study reveals a very rich structure behind the Lyapunov spectrum of the system. In particular, we discover a long-living intermediary regime that the system enters before turning into a completely ergodic system. Further, we demonstrate that quantum and classical spins are related when quantum spins are large. In particular, such relation is manifested by the existence of special eigenstates, which are remnants of classical periodic trajectories. We also introduce the so-called quantum separatrix, which distinguishes between different regimes of motion, and we demonstrate that the location of this separatrix may be predicted from classical value with reasonable accuracy. We observe slow thermalization of such initial conditions for values of quantum spin higher than $1/2$. We also observe several eigenstates with values of local observables significantly deviating from equilibrium values.

1.2.2 Almost complete revivals

Secondly, we introduce the phenomenon of almost complete revivals (ACR) of local spin polarization in quantum spin lattices. We consider a non-integrable lattice of interacting spins $1/2$ and show how to construct a quantum state such that a given spin 1/2 is maximally polarized initially and then exhibits an almost complete recovery of the initial polarization at a predetermined moment of time. We refer to such special initial states as “ACR” states.

Such states may be constructed for a wide class of finite non-integrable spin Hamiltonians. Furthermore, let us emphasize that the revival time can also be chosen arbitrarily. We also demonstrate that ACR is present in quantum systems of 5-25 spins.

We further discuss the statistical properties of ACR and its connection to the theory of relaxation. We also show that ACR is suppressed for high quantum spins, which agrees with the classical picture, where such revivals at an arbitrary moment are generally impossible due to the chaoticity of classical many-body systems. In addition, we propose several potential applications of ACR, such as benchmarking of quantum simulators, entanglement-assisted sensing, and delayed disclosures of a secret.

1.2.3 Manifestly non-classical eigenstates in a model of collisional decoherence

Lastly, we address the decoherence of a mesoscopic particle in a gas of microscopic particles. In this last chapter, we focus on special eigenstates which, at first sight, look highly out-of-equilibrium. It is expected that, if the mesoscopic particle is prepared in the so-called “Schrödinger’s cat state”, namely in a highly nonclassical spatial superposition at two distant points, then such a state should be highly out of equilibrium. Indeed, one expects those light particles would quickly “measure” the heavy one, thereby destroying the superposition. Nevertheless, we discover a small subset of eigenstates in the middle of the spectrum in which heavy particle is highly non-classical in the sense mentioned above, contrary to the expectations.

Chapter 2

Fate of periodic trajectories and weakly scarred quantum dynamics in many spin systems

2.1 Preliminary remarks

2.1.1 Stability of periodic trajectories

In a chaotic many-body system, the evolution of a trajectory from randomly selected initial conditions usually manifests exponential instability with respect to small perturbation of the initial conditions. To quantitatively characterize such instabilities, one usually utilizes the formalism of Lyapunov exponents [61] which has been applied successfully for a number of paradigmatic models of many-body physics [62–66]. The maximal Lyapunov exponent $\lambda_{\max}$ (exact definition will be provided later in this section) quantitatively characterize the growth of the distance $d(t) \sim e^{\lambda_{\max} t}$ between two initially close phase trajectories.

Usually, if a system has a positive maximal Lyapunov exponent $\lambda_{\max}$, it means that the almost all randomly selected trajectories in the system are unstable. The periodic trajectories, however, require special consideration. In particular, as we will show below, there are certain cases when a chaotic system possesses a stable periodic trajectory. The stability of such a trajectory cannot be described with the maximal

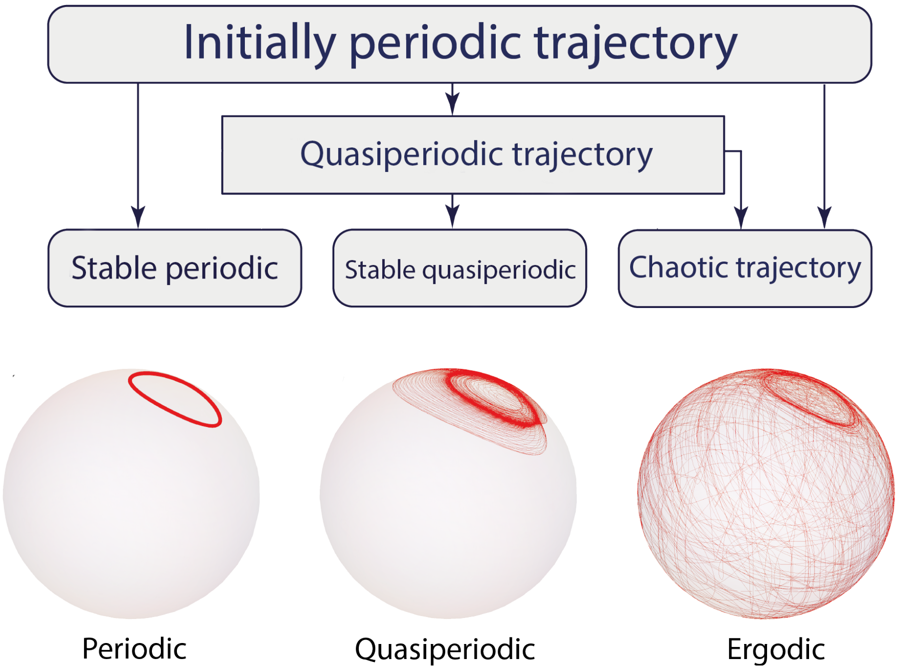

Figure 2-1: Possible scenarios for the evolution of initially periodic trajectory. The time-evolution of initially periodic trajectory was obtained as a solution of (2.4). The dynamics of the first spin $\mathbf{S}_1(t)$ is plotted for $t \in [0, 200]$, $J = 1.76$. (a) $L = 23$ periodic trajectory is stable (b) $L = 6$ periodic trajectory goes to neither periodic nor ergodic transient regime (c) $L = 13$ periodic trajectory is unstable and eventually becomes ergodic.

Lyapunov exponent $\lambda_{\max}$. For this reason, we will introduce a special "periodic" Lyapunov exponent λ_p, describing the stability of the periodic trajectories.

As we will show in this chapter, in a classical chaotic spin system, a trajectory close to the periodic one can have zero Lyapunov exponent $\lambda_p = 0$, thus being perpetually periodic. We will also demonstrate the existence of a remarkable intermediate quasiperiodic regime when the periodicity is lost, but the trajectory becomes stable. Possible scenarios for the evolution of the initially periodic trajectory and all three regimes are illustrated in Fig. 2-1. Spin trajectories to be shown in this figure will be discussed further in detail.

The present research was motivated by our interest in exploring whether the periodic trajectories in many-body classical systems entail any quantum consequences. Specifically, we consider rather generic translationally invariant lattices of interacting spins — classical and quantum, with the former representing the classical limit of the latter. For the classical lattices, we investigate the stability of a class of periodic trajectories with all spins pointing in the same direction and then explore the corresponding dynamics of the quantum lattices. In other words, we describe the “fate of periodic classical trajectories” in two senses: fate in the sense of their stability in purely classical systems and fate in transitioning from classical to quantum dynamics.

At the outset of this investigation, we expected that the signatures of the periodic trajectories have little chance of leading to atypical scar-like eigenstates in the thermodynamic limit because the trajectory would need to close onto itself on the timescale faster than the inverse of the sum of all positive Lyapunov exponents of the system known as the Kolmogorov-Sinai entropy, which grows proportionally to the system size. On the other hand, we hoped that the signatures of the periodic dynamics would survive in the initial relaxation of the system even in the thermodynamic limit and in the appearance of scar-like eigenstates for finite quantum spin systems. Both of the above expectations were largely borne out by our numerical results. Yet, this investigation uncovered rather unexpected stability and the associated rich behavior of the periodic classical trajectories, which supposedly made the quantum signatures of these trajectories more robust.

We considered a lattice of spins well-defined both classically and quantum mechanically. In the model under consideration, periodic trajectories tend to be more stable when the interaction between classical spins is strengthened compared with an external magnetic field. On the quantum side we simulate chains of finite sizes for quantum spins $S = \frac{1}{2}, 1, \frac{3}{2}, 2$. For quantum spins higher than one, we observed the emergence of some peculiar eigenfunctions characterized by a low entanglement entropy which reside in the bulk of the otherwise quantum chaotic spectrum. We refer to these eigenfunctions as “finite size quantum scars” (FSQS). Importantly such scars are responsible for the atypically long relaxation of quantum observables in the thermodynamic limit.

2.2 General formulation

We consider translationally invariant periodic chains of L interacting spins –

classical and quantum – described by the Hamiltonian:

$$\begin{aligned}\mathcal{H} = -\sum_{i=1}^{L} \left(J S_i^x S_{i+1}^x + 2J S_i^y S_{i+1}^y \right) \\ + \sum_{i=1}^{L} \left(h S_i^x + h S_i^y \right), \end{aligned} \tag{2.1}$$

where, in the classical case, S_i^α are the components of 3-dimensional vectors $\mathbf{S}_i = (S_i^x, S_i^y, S_i^z)$ of unit length, and in quantum case S_i^α are spin-S operators, i is the lattice index, $\alpha = x, y, z$ is the spin projection index, J and h are the interaction constant and the local field parameter, respectively. Throughout the chapter, we fix $h = 1$ and consider the following values of quantum spin $S = \frac{1}{2}, 1, \frac{3}{2}, 2$. We also set $\hbar = 1$ where relevant. The above particular form of the Hamiltonian is known to lead to a well-defined non-integrable behavior in the quantum case even for relatively modest system sizes. The anisotropy in the XY plane is responsible for the robust absence of quantum integrability and for the existence of intermediate quasiperiodic classical regime which will be introduced further.

We investigate one special type of nonequilibrium initial conditions corresponding to all spins polarised in the same direction. Specifically, we choose them polarised along the z-direction, which, according to Hamiltonian (2.1), imply that the initial energy E_0 is equal to zero, which, in turn, corresponds to the infinite temperature, implying that the initial state belongs to the energy shell of maximum entropy (maximum density of states quantum mechanically); the latter minimizes the influence of the finite-size effects on our numerical results.

In the classical case, the above initial conditions are represented by $3L$-dimensional vector:

$$\mathcal{S}(0) = \{\mathbf{S}_i(0) = (0,0,1)\}_{i=1}^{L}. \tag{2.2}$$

In the quantum case, the fully polarized "up"-states are described by the initial wavefunction:

$$|\Psi(0)\rangle = |\Psi^{\mathrm{up}}\rangle \equiv \bigotimes_{i=1}^{L} |m_i = S\rangle. \tag{2.3}$$

2.3 Classical spins

2.3.1 Equations of motion

Classical dynamics of the Hamiltonian (2.1) is governed by the system of $3L$ nonlinear differential equations:

$$\frac{dS_j^\alpha}{dt} = \{\mathcal{H}, S_j^\alpha\} \tag{2.4}$$

where $\{...,...\}$ are the Poisson brackets, with $\{S_i^\alpha, S_j^\beta\} = \delta_{ij}\epsilon_{\alpha\beta\gamma}S_i^\gamma$, δ_{ij} is the Kronecker delta, and $\epsilon_{\alpha\beta\gamma}$ is the Levi-Civita epsilon. The system of equations (2.4) can be rewritten as

$$\frac{d\mathbf{S}_j}{dt} = \mathbf{H}_j \times \mathbf{S}_j, \tag{2.5}$$

where

$$\mathbf{H}_j = \begin{pmatrix} -JS_{j-1}^x - JS_{j+1}^x + h \\ -2JS_{j-1}^y - 2JS_{j+1}^y + h \\ 0 \end{pmatrix} \tag{2.6}$$

is the local field acting on the jth spin. The solutions of Eqs.(2.5, 2.6) give $3L$-dimensional vectors $\mathcal{S}(t) = (S_1^x(t), S_1^y(t), S_1^z(t), \ldots, S_L^x(t), S_L^y(t), S_L^z(t))$.

Where necessary, we solve the above set of equations using the 4th-order Runge-Kutta algorithm with discretization step $\Delta t = 0.001$ or smaller.

2.3.2 Periodic trajectories

Due to the translational invariance of both the initial conditions (2.2) and the Hamiltonian (2.1), the classical spins initially polarised in the same direction exhibit the same time evolutions and hence remain parallel to each other at all subsequent moments of time, but the direction of their common polarisation evolves as a function of time. As a result, the calculation of a many-spin trajectory $\mathcal{S}(t)$ is reduced to computing the same one-spin trajectory $\mathbf{S}_j(t) = \mathbf{S}_\mathrm{p}(t)$ for each spin on the lattice. The one-spin trajectory $\mathbf{S}_\mathrm{p}(t)$ is limited to a two-dimensional manifold - the surface of a unit sphere $|\mathbf{S}_\mathrm{p}| = 1$. On a two-dimensional manifold a phase-space trajectory normally cannot avoid closing onto itself, which means that it becomes periodic. The corresponding many-spin trajectory, to be denoted as $\mathcal{S}_\mathrm{p}(t)$, also becomes periodic.

Since all spins during this dynamics point in the same direction, the projections of $\mathbf{S}_{j-1}$ and $\mathbf{S}_{j+1}$ in Eq.(2.6) can be replaced by those of $\mathbf{S}_j$, and, as a result, the periodic one spin trajectories $\mathbf{S}_\mathrm{p}(t)$ can be computed with the help of one-spin Hamiltonian

$$\mathcal{H}_\mathrm{p} = -J(S_\mathrm{p}^x)^2 - J(S_\mathrm{p}^y)^2 + hS_\mathrm{p}^x + hS_\mathrm{p}^y. \tag{2.7}$$

Initial conditions (2.2) correspond to zero energy, indeed if $\mathbf{S}_p(0) = (0, 0, 1)$ then $\mathcal{H}_\mathrm{p} = 0$. The quadratic equation $\mathcal{H}_\mathrm{p} = 0$ in terms of S^x and S^y, together with the condition $|\mathbf{S}_\mathrm{p}| = 1$, defines an energy shell, which is represented by a line on the unit sphere. In Figure 2-2 we plot one-spin trajectories $\mathbf{S}_p(t)$ for different values of J. As expected $\mathbf{S}_p(t)$ closes onto itself and thus becomes periodic.

2.3.3 Librations and rotations

Dependent on the parameters of the Hamiltonian $\mathcal{H}_\mathrm{p}$ and the initial orientation of the spins $\mathbf{S}_\mathrm{p}(0)$, there are two possible kinds of periodic trajectories $\mathbf{S}_\mathrm{p}(t)$, which, by analogy with the description of a pendulum, we call “librations” and “rotations” [29]. Librations are realised by a single trajectory on the spherical surface $|\mathbf{S}_\mathrm{p}| = 1$ connecting all points having the same energy. Two disconnected trajectories realize the rotations corresponding to the same energy. Librations and rotations transition to each other as a function of Hamiltonian parameters and/or initial energy through a separatrix, as illustrated in Fig.2-2.

When a periodic trajectory is considered as a function of J for fixed $h = 1$ and fixed energy $E = 0$ (associated with our initial conditions “all-spins-up”), the

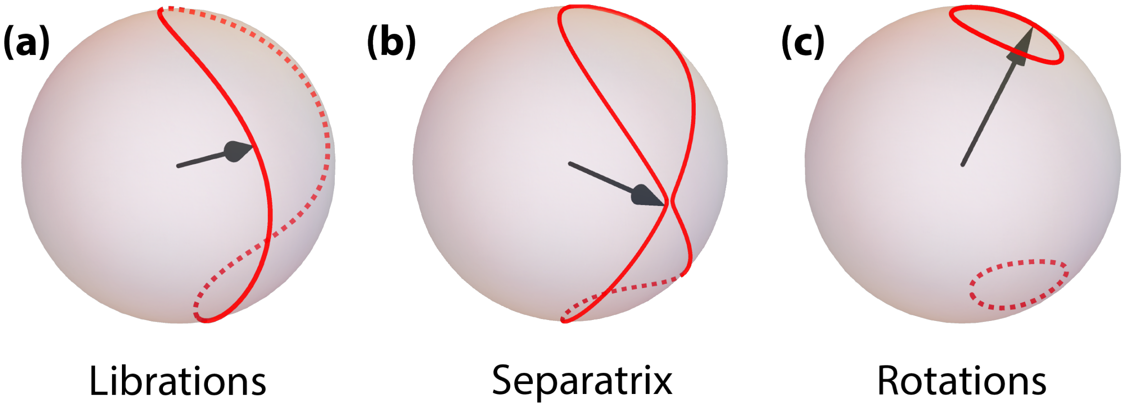

Figure 2-2: Periodic solutions corresponding to the one-body Hamiltonian (2.7) (a) $J = 0.79$ Librations, trajectory oscillates between two poles (b) $J \simeq J^* = 1.15041$ Vicinity of the separatrix distinguishing between two regimes (c) $J = 1.76$ Rotations, trajectory is confined inside the upper hemisphere. There is an identical trajectory inside the bottom hemisphere obtained from $\mathbf{S}_p(0) = (0, 0, -1)$.

separatrix corresponds to $J = J^* \simeq 1.15$. Librations are realized for $J < J^*$, and rotations for $J > J^*$.

As we see later, rotations appear to be more stable and have a stronger tendency to evolve into a quasiperiodic motion.

2.3.4 Lyapunov instabilities

Instabilities of phase space trajectories cause chaos in nonlinearly interacting classical systems with respect to small deviations of initial conditions. The instability of a phase trajectory in a $2L$-dimensional phase space is characterized by a spectrum of $2L$ Lyapunov exponents $\{\lambda_k\}$. Some Lyapunov exponents corresponding to integrals of motion or other directions not exhibiting *exponential* sensitivity to small deviations may be zero. A phase space trajectory is chaotic when its maximum Lyapunov exponent $\lambda_{\max}$ is greater than zero. Another commonly used characteristic of chaos is the sum of all positive Lyapunov exponents $K \equiv \sum_k^{\lambda_k>0} \lambda_k$, also known as the Kolmogorov-Sinai entropy.

To compute $\lambda_{\max}$, one chooses a reference phase space trajectory $\mathcal{S}(t)$ and an infinitesimally close one $\mathcal{S}(t) + \delta\mathcal{S}(t)$, then traces the growth of $\delta\mathcal{S}(t)$, which is eventually overtaken by the largest Lyapunov exponent. This implies that

$$\lambda_{\max} = \lim_{\substack{t\to\infty,\\ |\delta\mathcal{S}(0)|\to 0}} \frac{1}{t} \log \frac{|\delta\mathcal{S}(t)|}{|\delta\mathcal{S}(0)|}. \tag{2.8}$$

Practical numerical computation of $\lambda_{\max}$ requires one to perform a large number of resets (contractions) of $|\delta\mathcal{S}(t)|$ as described in Refs. [61, 62].

Largest Lyapunov exponents $\lambda_{\max}$ and the entire Lyapunov spectra $\{\lambda_k\}$ of classical spin systems have previously been investigated [62] but only in the vicinity of ergodic trajectories, which nonperiodically cover the entire energy shell of the system. If a trajectory is ergodic, it is supposed to pass in the vicinity of every point on the energy shell, thereby "collecting" all possible local growth rates of $|\delta\mathcal{S}(t)|$ and averaging over them. As a result, $\lambda_{\max}$ and the entire Lyapunov spectrum do not depend on the choice of the initial conditions $|\mathcal{S}(0)|$. The convergence of the procedure for computing $\lambda_{\max}$ is, in fact, a good measure of the ergodisation time of the underlying dynamics.

The periodic phase space trajectories in many-body systems are rather exceptional as they correspond to a subset of initial conditions of measure zero. Periodic trajectories are not ergodic; hence they do not cover the entire energy shell and thus are not supposed to have the same Lyapunov spectrum as the ergodic trajectories. Moreover, it cannot be excluded *a priori* that they are Lyapunov-stable even when their ergodic counterparts are unstable.

The periodic trajectories considered in this chapter have one further defining property: they are translationally invariant in a system where the Hamiltonian is also translationally invariant. To explore the consequences of this property, let us define the operator $\mathcal{L}_t$ governing the growth of small deviations in the Lyapunov problem by the relation

$$\delta\mathcal{S}(t) = \mathcal{L}_t(\delta\mathcal{S}(0)) \tag{2.9}$$

The operator $\mathcal{L}_t(\delta\mathcal{S}(0))$ is linear with respect to $\delta\mathcal{S}(0)$. The problem of computing the Lyapunov spectrum is an eigenvalue problem for $\mathcal{L}_t$. The eigenvalues have the form $e^{\lambda_k t + i\omega_k t}$, where the frequency ω_k controls the phase factor when present. Each eigenvalue corresponds to an eigenvector $\delta\mathcal{S}_k$. Since both the underlying Hamiltonian and the reference trajectory are translationally invariant on the lattice, the operator $\mathcal{L}_t$ must also be translationally invariant. In such a case, the eigenvectors of this operator realize irreducible representations of the lattice translational symmetry group, which have the form $e^{i\mathbf{qr}}$, where $\mathbf{r}$ the coordinate of the lattice site and $\mathbf{q}$ is the wave vector. In other words, each Lyapunov exponent λ_k, corresponds to instability around the reference periodic trajectory $\mathcal{S}_{\mathrm{p}}(t)$, which develops with a well-defined wave vector $\mathbf{q}_k$ with the allowed values of the wave number $q_k = \frac{2\pi}{L}k$, where $k = 0, 1, ..., L-1$.

Generically, different wave vectors $\mathbf{q}_k$ are supposed to correspond to different values of λ_k with the exception of symmetry-related degeneracies or accidental degeneracies. A symmetry-related degeneracy occurs, particularly when the lattice has inversion symmetry (as is the case for our investigation), and, as a result, pairs of wave vectors $\pm\mathbf{q}_k$ correspond to the same λ_k. In such a case, a generic Lyapunov exponent is at least double-degenerate, the possible exceptions correspond to $q_k = 0$ and $q_k = \pi/L$.

The symmetry considerations further imply that different irreducible representations are not supposed to mix in the linear approximation, which, in turn, means that the linear stability problem in many-dimensional phase space is decomposed into a set of stability problems in low-dimensional subspaces. The latter brings back the concerns based on the KAM (Kolmogorov–Arnold–Moser) [29] theorem that the periodic trajectory may turn out to be Lyapunov-stable.

All these interesting possibilities can be investigated by the direct numerical calculation of the largest positive Lyapunov exponent in the vicinity of the periodic trajectories $\mathcal{S}_{\mathrm{p}}(t)$, which we denote as λ_{p}.

From now on, we focus on our one-dimensional lattice, where symmetry representations are characterized by wave numbers q rather than wave vectors, and so are the Lyapunov instabilities. The above discussion implies that when the periodic trajectory $\mathcal{S}_{\mathrm{p}}(t)$ is Lyapunov unstable, the instability corresponding to the largest Lyapunov exponent λ_{p} generically develops as a standing wave in real space characterized by a pair of wave numbers $\pm q_{\mathrm{p}}$.

The numerical algorithm for computing λ_{p} is the same as the computing $\lambda_{\max}$

for an ergodic trajectory. The only practical difference is that the reference periodic trajectory is to be computed semi-analytically, such that the long runs along it are not the subject of growing numerical error. In particular, we compute periodic trajectory $\mathbf{S}_p(t)$ by numerically solving equations corresponding to the one-spin Hamiltonian (2.7). After that we construct "perfect" many-spin trajectory $\mathcal{S}_p(t)$ by periodically copying $\mathbf{S}_p(t)$ over time such that $\mathbf{S}_p(t+Tn) = \mathbf{S}_p(t)$ for an arbitrary integer n.

2.3.5 Results: Dependence of λ_p on J and L

The dependence of λ_p on the interaction strength J for several system sizes L is plotted in Fig. 2-3. The dependence of λ_p on L for three different values of J is presented in Fig. 2-5. We now describe and discuss these results.

As explained in Section 2.3.3, the periodic trajectory that starts from the all-spins-up state of our spin chain undergoes a transition from the libration to the rotation regime as a function of the interaction parameter J for fixed $h = 1$ at $J = J^* \approx 1.15$, which corresponds to a separatrix.

Figures 2-3 and 2-5(a) illustrate that the periodic motion in the libration regime $J < J^*$ is, generally, unstable, except for a finite set of small values of L, for which $\lambda_\mathrm{p} = 0$. We observed that $\lambda_\mathrm{p} > 0$ for $J > 0.3$ and $L > 10$ for all simulated librations. The typical dependence of λ_p on J is a monotonic growth diverging at the separatrix $J < J^*$. We further note in Fig.2-5(a) the weak oscillatory dependence of λ_p on L.

The rotation regime $J > J^*$ has a richer phenomenology, which can be observed in Figs. 2-3 and 2-5(b,c). In this regime, the unstable character of the periodic motion is less robust than in the libration regime in the sense that the occurrence of $\lambda_\mathrm{p} = 0$ extends to significantly larger values of L, and also appears in the limit $J \to \infty$ for all simulated chains except for those whose lengths L are multiples of 6. As one can further see in Fig. 2-3, λ_p on the rotation side of the plots, when not equal to zero, decreases monotonically as a function of J starting from the infinite value at $J = J^*$ but, in comparison with librations, it exhibits a more diverse functional dependence on J with a characteristic switching character. Also, as seen in Figs.2-5(b,c), λ_p for rotations exhibits a much stronger oscillatory dependence on

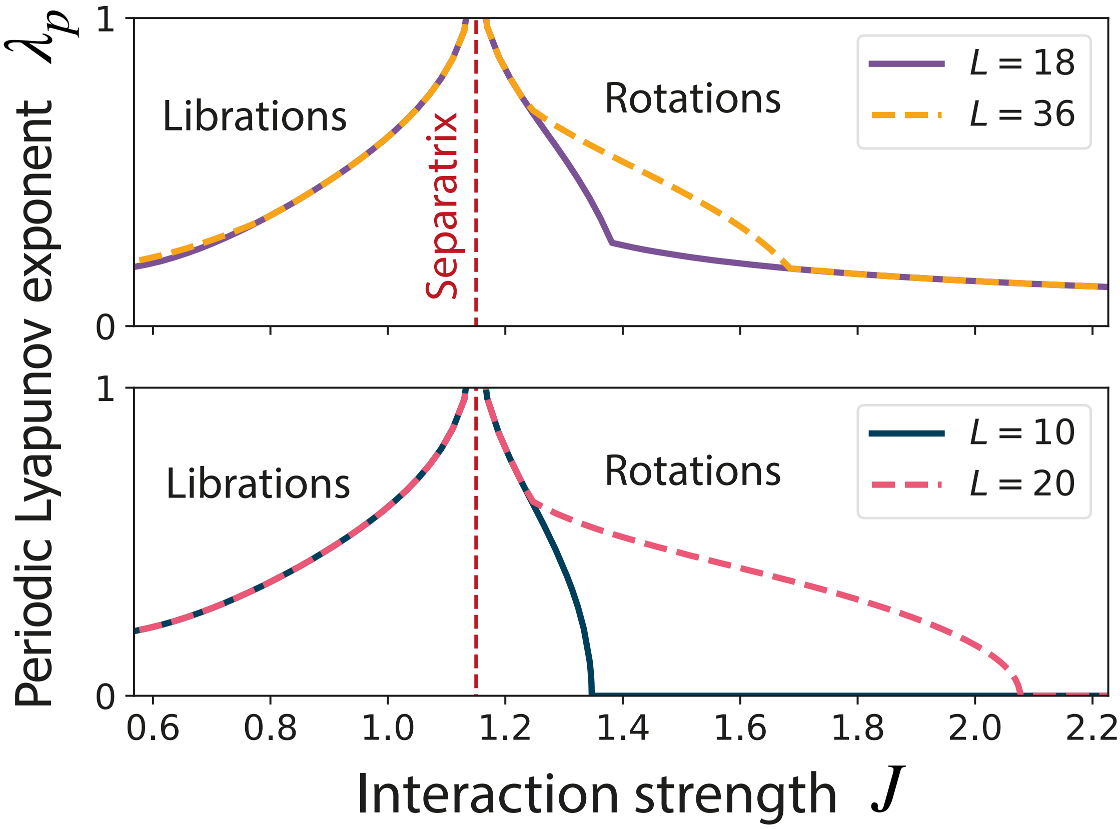

Figure 2-3: Dependence of periodic Lyapunov exponent λ_p on the value of J for the spin chains of different sizes L with $h = 1$. The separatrix between the libration and the rotation regimes corresponds to $J = J^* \approx 1.15$. Chains of different lengths L that are multiples of each other often exhibit intervals of equal λ_p, which indicates the underlying spatial periodicity of the Lyapunov vectors corresponding to λ_p. We further note that $\lambda_p \to 0$ when J is sufficiently large unless L is a multiple of 6.

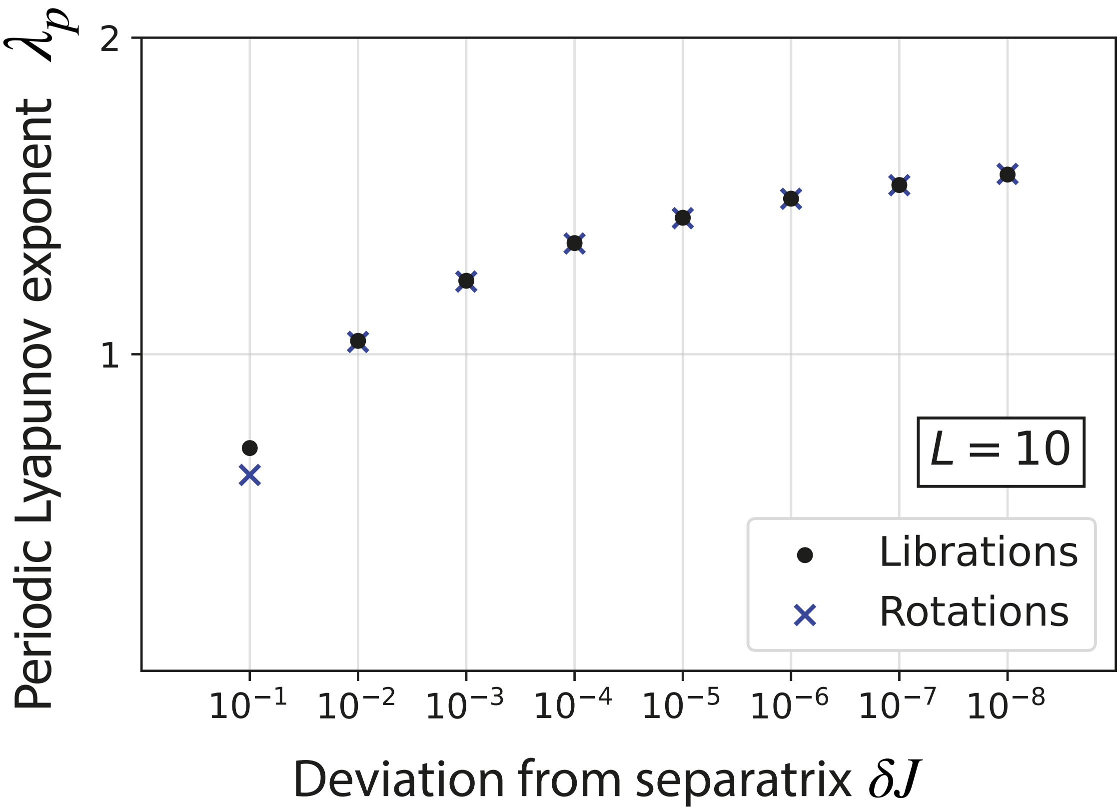

Figure 2-4: Lyapunov exponent λ_p in the vicinity of separatrix $J = J^* \pm \delta J$. The value of separatrix is approximately $J^* \simeq 1.1504059085$. Minimal value of δJ is equal to 10^{-8}. Values $J = J^* - \delta J$ correspond to the regime of librations, while $J = J^* + \delta J$ correspond to rotations.

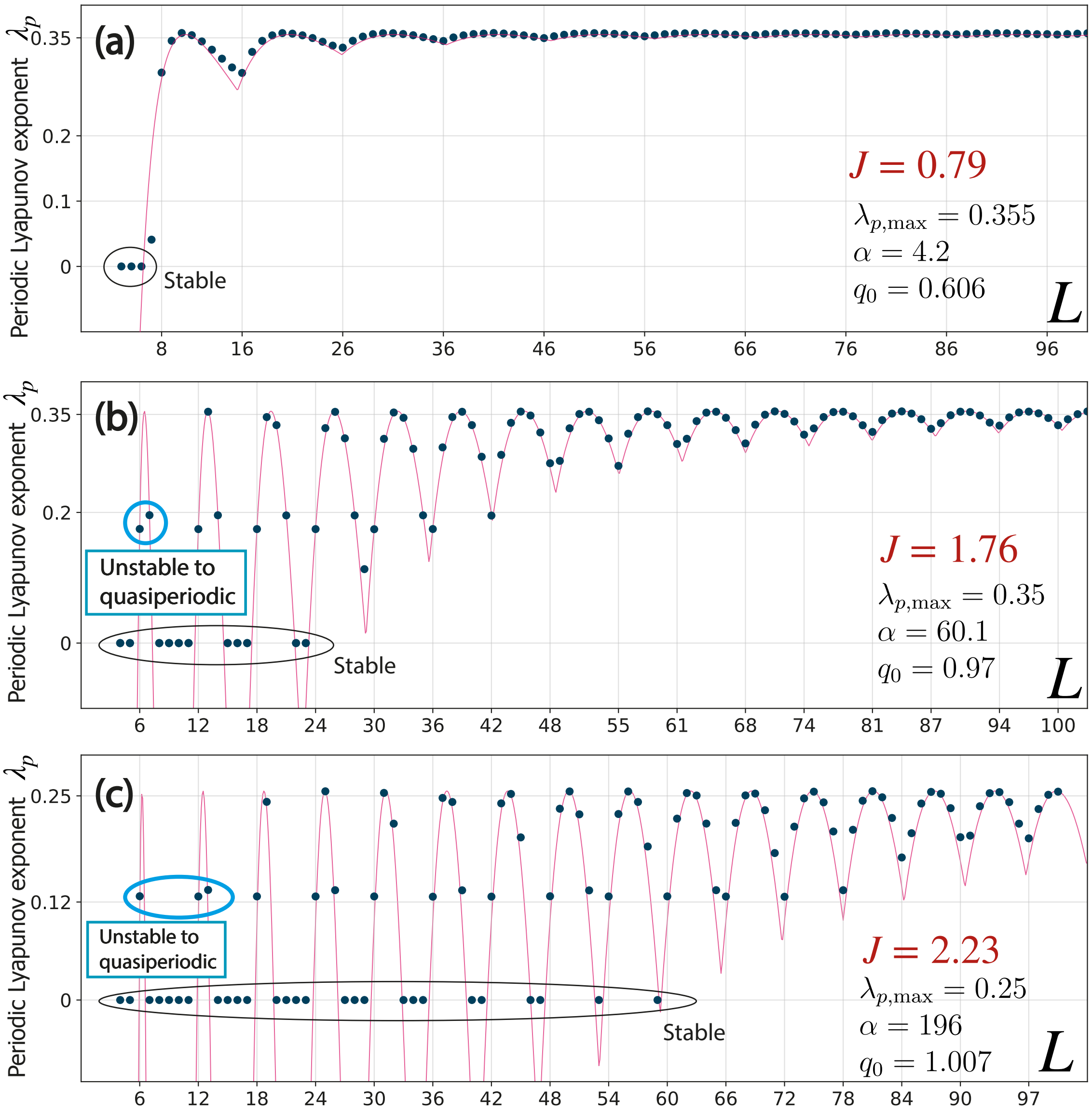

Figure 2-5: Lyapunov exponents λ_p versus different system size L, for fixed values of J (a) $J = 0.79$ regime of librations $\lambda_\mathrm{p}(L)$ quickly saturates, (b,c) regime of rotations $J = 1.76$ and $J = 2.23$ correspondingly. The dependence of $\lambda_\mathrm{p}(L)$ is non-monotonic.

L.

The standard algorithms of calculation of Lyapunov exponents do not work in the close vicinity of separatrix $J = J^*$. Indeed, as we approach separatrix closer, we need to take smaller values of initial perturbations $\delta\mathcal{S}$. In real calculations, however, we are always limited by selected machine precision (the smallest difference between two numbers which computer recognizes). Therefore, in practice, we cannot approach separatrix arbitrarily close.

To analyze the behavior of periodic Lyapunov exponents near separatrix, we have computed them for different small violations from J^* such that $J = J^* \pm \delta J$, see Fig. 2-4. This figure shows that λ_p growth in the vicinity of separatrix, yet this growth is slow.

Although we cannot compute λ_p on the separatrix or arbitrarily close to it, we expect that it has a finite value. The following argument supports this expectation. Points in the phase space move with limited speed; therefore, $\lambda_p(J)$ must be confined from above for all finite J, including J^*. Also, from Fig. 2-4, we can see that in the vicinity of separatrix, the Lyapunov exponent is an even function of perturbation, such that $\lambda_p(J^* - \delta J) = \lambda_p(J^* + \delta J)$. This fact hints that λ_p shall be continuous in the point $\lambda_p(J^*)$.

Let us finally mention here that the numerically computed largest Lyapunov exponent for an ergodic trajectory of a system with $J = 1.76$ and large $L = 100$ on the infinite-temperature energy shell is $\lambda_{\max} \approx 1.18$, which is significantly larger than the Lyapunov exponents $\lambda_{\rm p}$ reported in Fig.2-5. Yet the value of $\lambda_{\rm p}$ would easily exceed $\lambda_{\max}$ once J approaches the separatrix value J^*.

Translational symmetry breaking by Lyapunov vectors.

The above-described phenomenology is rather diverse, but it can be brought into a single perspective based on the considerations of Section 2.3.4, that the Lyapunov vectors lower the full translational symmetry of the system to the one characterized by a particular wave number q.

In Fig 2-6, we plot the spatial Fourier transforms of the Lyapunov vectors corresponding to $\lambda_{\rm p}$ for two chain lengths $L = 18$ and $L = 20$ and for two interaction constants J representing the libration and the rotation regimes for each length. In

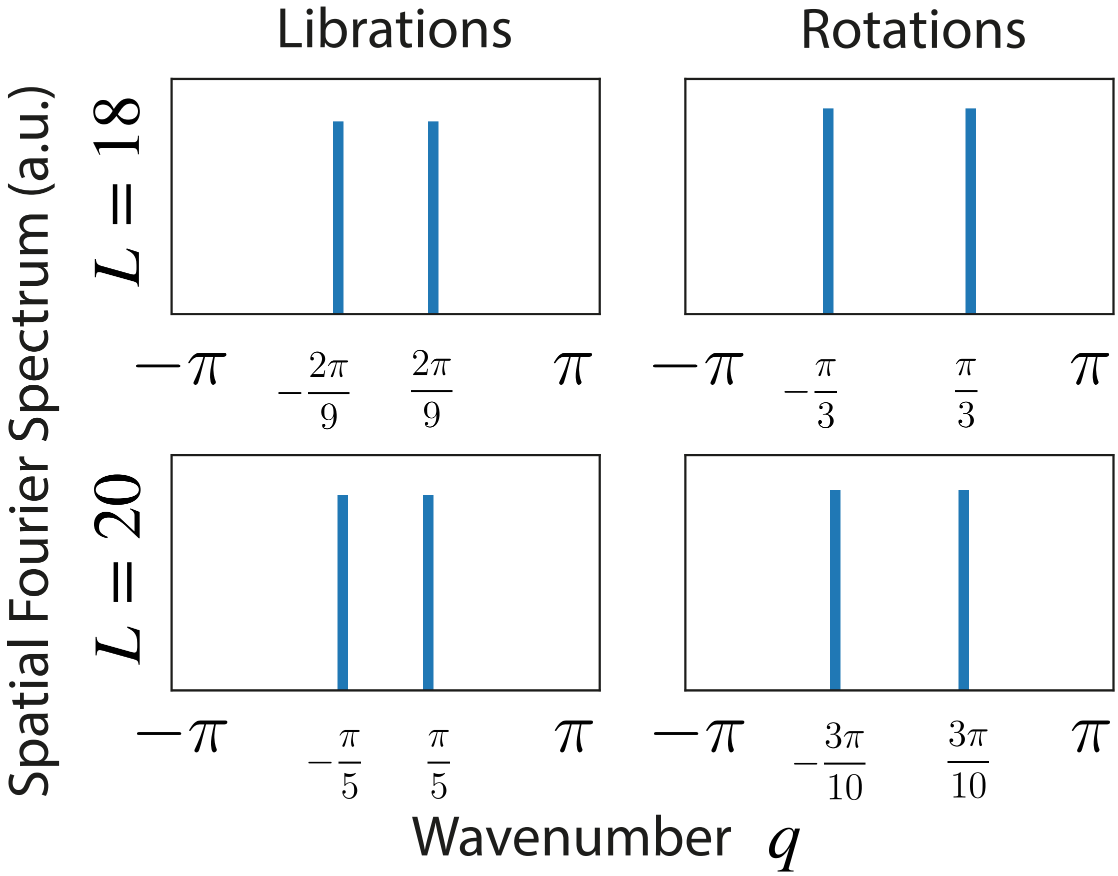

Figure 2-6: Fourier transformation of the Lyapunov vectors corresponding to λ_p for chain lengths $L = 18, 20$. Regime of librations corresponds to the $J = 0.79$, regime of rotations $J = 1.76$.

all four cases, one can see two dominant Fourier peaks corresponding to $\pm q$.

The underlying translational symmetry breaking helps us to explain the distinct switching behavior of plots in Fig.2-3 on the rotation side, where there are ranges of the values of J, where the Lyapunov exponents λ_p for the chains of different lengths coincide, and there are ranges, where they suddenly become different. The two pairs of plots in Fig. 2-3 correspond to chain lengths such that one chain is twice the length of the other. Therefore, the two chains have a set of allowed wave numbers q that are equal to each other, but then the longer chain has additional wave numbers that are unavailable for the shorter one. Thus, if the largest Lyapunov exponent for the longer chain corresponds to q available for the shorter chain, then the two Lyapunov exponents λ_p are equal to each other. If, however, the above q for the longer chain is not available for, the shorter one, then the values of λ_p become different, with the larger λ_p necessarily corresponding to the longer chain.

Analytical approximation for $\lambda_p(L)$.

We now convert the qualitative understanding of the role of the translational symmetry breaking into an analytical formula describing the entire dependence $\lambda_\mathrm{p}(L)$.

The oscillatory dependence of λ_p on L in Fig.2-5, presumably, originates from the fact that, for a chain of a given length L, the allowed values of the wave number $q = \frac{2\pi}{L}n$, where $n = 0, 1, ..., L-1$ cannot exactly match a certain value q_0 that is optimal for the strongest Lyapunov instability $\lambda_\mathrm{p,max}$. As the length of the chain increases, the allowed values of q come increasingly closer to q_0, and, as a result, the oscillatory part of $\lambda_\mathrm{p}(L)$ becomes gradually suppressed. We are dealing with a supposedly small difference between q_0 and the nearest allowed value $q_\mathrm{p} = \frac{2\pi}{L}$ round $\left(\frac{q_0 L}{2\pi}\right)$, where function “round(...)” rounds its argument to the nearest integer value. It is thus reasonable to parameterize the departure from $\lambda_\mathrm{p,max}$ by a quadratic dependence on the above difference:

$$\lambda_\mathrm{p}(L) = \lambda_\mathrm{p,max} - \alpha \left[q_0 - \frac{2\pi}{L} \,\mathrm{round} \left(\frac{q_0 L}{2\pi} \right) \right]^2, \tag{2.10}$$

where $\lambda_\mathrm{p,\,max}$, q_0 and α are three adjustable parameters.

The remarkably good performance of formula (2.10) in describing the numerically computed $\lambda_{\mathrm{p}}(L)$ is demonstrated in Fig.2-3. The one can observe that it gives an excellent quantitative description also in the regime of large differences between $\lambda_{\mathrm{p}}(L)$ and $\lambda_{\mathrm{p,max}}$. In this large-deviations regime, the formula (2.10) has to be further supplemented by the condition that, if it predicts $\lambda_{\mathrm{p}} < 0$, then $\lambda_{\mathrm{p}} = 0$ should be substituted instead, implying that the periodic motion is Lyapunov stable. With such a modification, the formula (2.10) turns into an excellent predictor of the lengths L corresponding to the stable periodic motion. The quality of the approximation (2.10) can be improved further by adding there terms with higher-order powers of $(q_0 - q_{\mathrm{p}})$.

2.3.6 Results: Quasiperiodic regime

While computing the Lyapunov exponents for periodic trajectories, we discovered that, as the Lyapunov instability develops and the deviations from the reference periodic trajectory become large and no longer describable by Lyapunov exponents, the dynamics do not immediately become chaotic —rather, it enters a quasiperiodic regime, which often has a rather long lifetime, especially when it is entered from a rotation-type periodic trajectory. One example of the transition to a stable quasiperiodic motion and one example of the transition to the chaotic regime through a long-living quasiperiodic regime are shown in Figs.2-7 (a) and (b), respectively. In a few computed cases indicated in Fig.2-5(b,c), ($J = 1.76$ with $L = 6, 7,$ and $J = 2.23$ with $L = 6, 12, 13$), the quasiperiodic regime is numerically stable, which means that on rather long timescale $t \simeq 10^5$ covered by the simulations, the system does not enter the chaotic regime see Fig. 2-8. We have also computed the Lyapunov exponents of these stable quasiperiodic trajectories and found them equal to zero.

The frequency spectrum of a periodic motion consists of discrete peaks at frequencies, all of which are the multiples of a fundamental frequency. For a chaotic motion, the spectrum is supposed to be continuous. The spectrum of a quasiperiodic motion inherits a discrete peak structure from the periodic motion, but the peaks are determined by the combinations of two or more frequencies, whose ratio is an

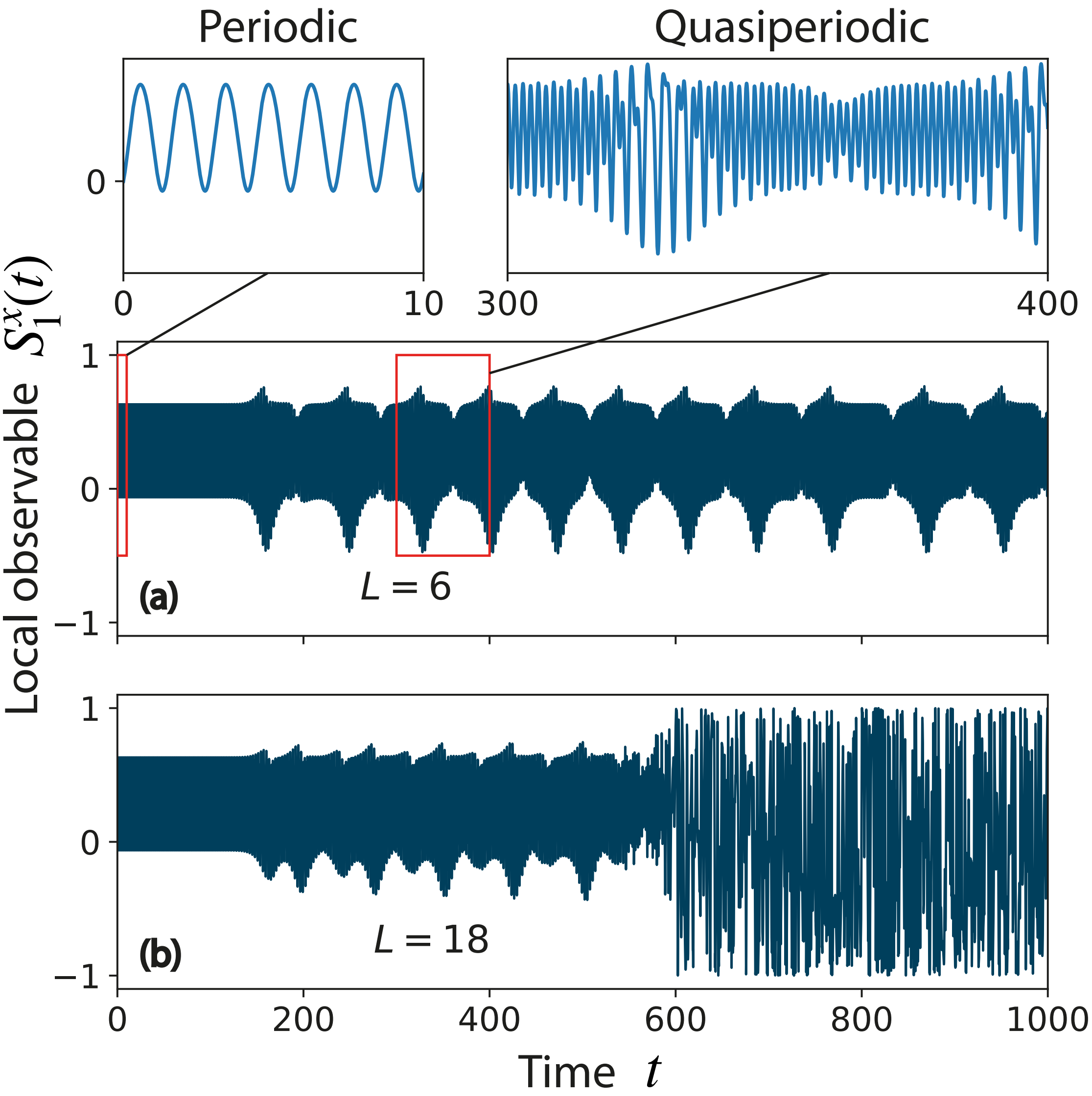

Figure 2-7: Quasiperiodic dynamics of $S_1^x(t)$ observable for $J = 1.76$. Top row: $L = 6$ unstable periodic motion comes to a stable transient regime. Bottom row: $L = 18$ transient regime is also unstable and eventually becomes chaotic.

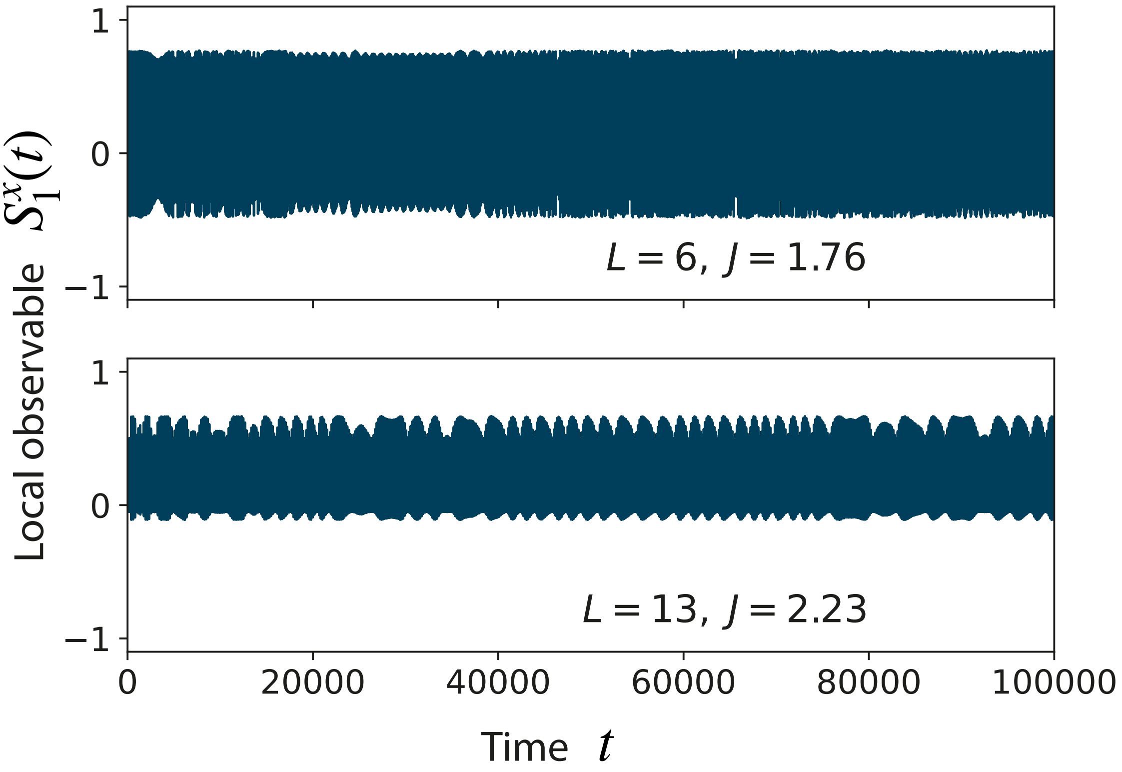

Figure 2-8: Very long-time dynamics of $S_1^x(t)$ observable in stable quasiperiodic regime. Top row: $L = 6, J = 1.76$. Bottom row: $L = 13, J = 2.23$.

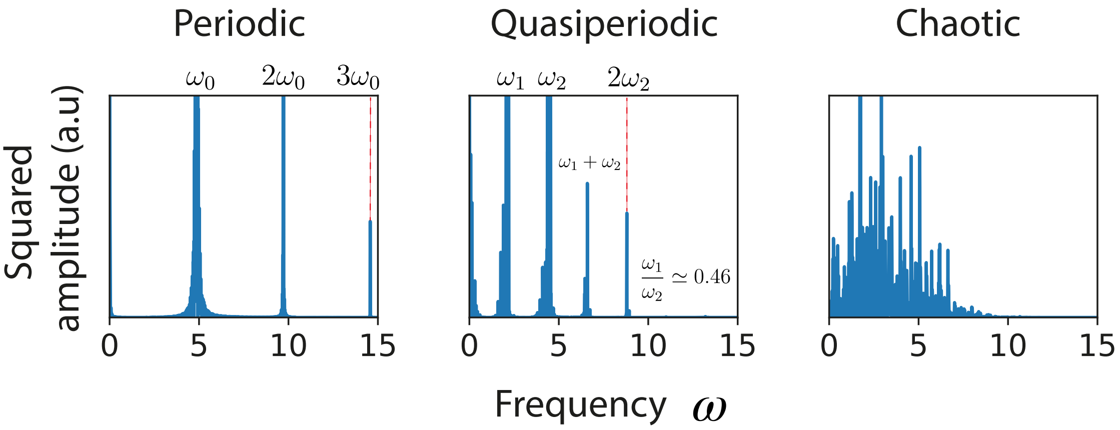

Figure 2-9: Fourier spectrum of the observable $S_1^z(t)$ for different regimes of motion. The spectrum is calculated for the finite time interval of $t \in [100, 1100]$.

irrational number. In Fig.2-9, we show the numerically computed frequency spectra for one variable within a system exhibiting periodic, quasiperiodic, and ergodic motion.

Figure.2-9(b) is particularly important for our identification of the quasiperiodic motion. There we identify two primary peaks with frequencies ω_1 and ω_2, and two secondary peaks at frequencies $\omega_1 + \omega_2$ and $2\omega_2$. The numerically accessed approximate ratio ω_1/ω_2 is 0.46, consistent with the expectation that the true value of ω_2/ω_1 is an irrational number.

Given the discussion in the previous subsection of the translational symmetry breaking accompanying Lyapunov instabilities, the explanation of the basic quasiperiodic character of the emerging motion can be the following. The initial periodic motion corresponds to a certain fundamental frequency, and the wave number $q = 0$. The motion that emerges as a result of the Lyapunov instability is characterized by wave vector $q = q_{\mathrm{p}} \neq 0$ and by another frequency. As the Lyapunov instability develops, the spectral weight shifts from the wave number $q = 0$ to the wave number $q = q_{\mathrm{p}}$. After a while, the two spectral components become comparable to each other, and the process becomes quasiperiodic with two incommensurate fundamental frequencies — one inherited from the original periodic motion with $q = 0$ and the other one characterising the motion with $q = q_{\mathrm{p}}$. As the amplitude of the motion with $q = q_{\mathrm{p}}$ grows, the interaction between the two modes renormalizes the frequencies of each of them. This change of frequencies naturally slows down once their ratio reaches the value corresponding to the most stable motion. The latter would be further destroyed when and if a mode with yet another frequency develops in the dynamics.

We call the above regime a “time quasicrystal” by analogy with quasicrystals in space. The latter has a fully broken translational symmetry and yet exhibit discrete Brag peaks in the wave-vector space. Likewise, the time quasicrystal emerges spontaneously, is not invariant with respect to any time shift, and yet exhibits the discrete peaks in the frequency space. It also exhibits discrete peaks in the wave-vector space, but those are commensurate with a fundamental wave vector of the underlying lattice.

2.4 Quantum spins

As discussed in the introduction, the present project was largely motivated by an attempt to explore whether periodic orbits in classical spin systems lead to scar-like eigenstates in their quantum counterparts. The expectation was that, on the one hand, the special scar eigenstates are unlikely to survive in the thermodynamic limit, but, on the other hand, they may appear in finite systems; also, the special initial thermalization behavior of observables may be inherited from the scar states in the thermodynamic limit.

Our classical investigation of the previous subsection indicates that the chances of observing the scar effects in many spin systems are, actually, somewhat better than what one would expect *a priori* from the knowledge of the Lyapunov spectra of ergodic trajectories. The reason is that one can choose the parameters of the Hamiltonian such that the largest Lyapunov exponent for a periodic trajectory is significantly smaller than that for an ergodic trajectory, and, moreover, there exist rather long spin chains for which the Lyapunov instabilities in the vicinity of the periodic trajectories are completely suppressed.

Below, we first consider the special initial condition (2.3) - "all spins up" , which in the classical limit gives the periodic trajectory, and check whether the evolution starting from that condition exhibits an anomalously slow thermalization. Then we decompose those initial conditions into the energy eigenstates of the systems and check whether any of the eigenstates prominently present in the above initial state also violate the eigenstate thermalization hypothesis.

This investigation is based on the exact diagonalization of the system's Hamiltonian (2.1) (periodic boundary conditions are implied same as in classical case). It involves quantum spins with $S = \frac{1}{2}, 1, \frac{3}{2}, 2$. Quantum spin vectors have length $\sqrt{S(S+1)}$, while, in the classical simulations, this length was set to 1. Spin length affects the relative strength of different terms in the Hamiltonian (2.1). We set $h = 1$ and $J = 0.91$ where not specified otherwise.

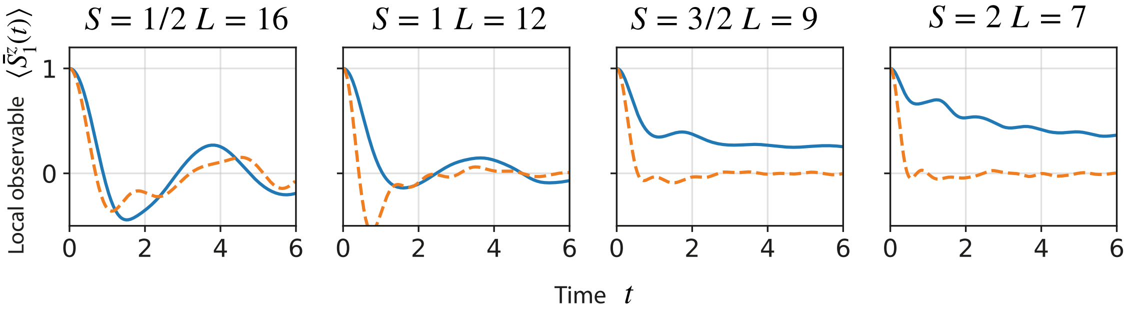

Figure 2-10: Time-evolution of a single spin $\langle \bar{S}_1^z(t) \rangle$ for $|\Psi^{\rm up}\rangle$ (solid line) and $|\Psi^{\rm inf}\rangle$ (dashed line) states, for different values of quantum spin. Value of $J = 0.91$.

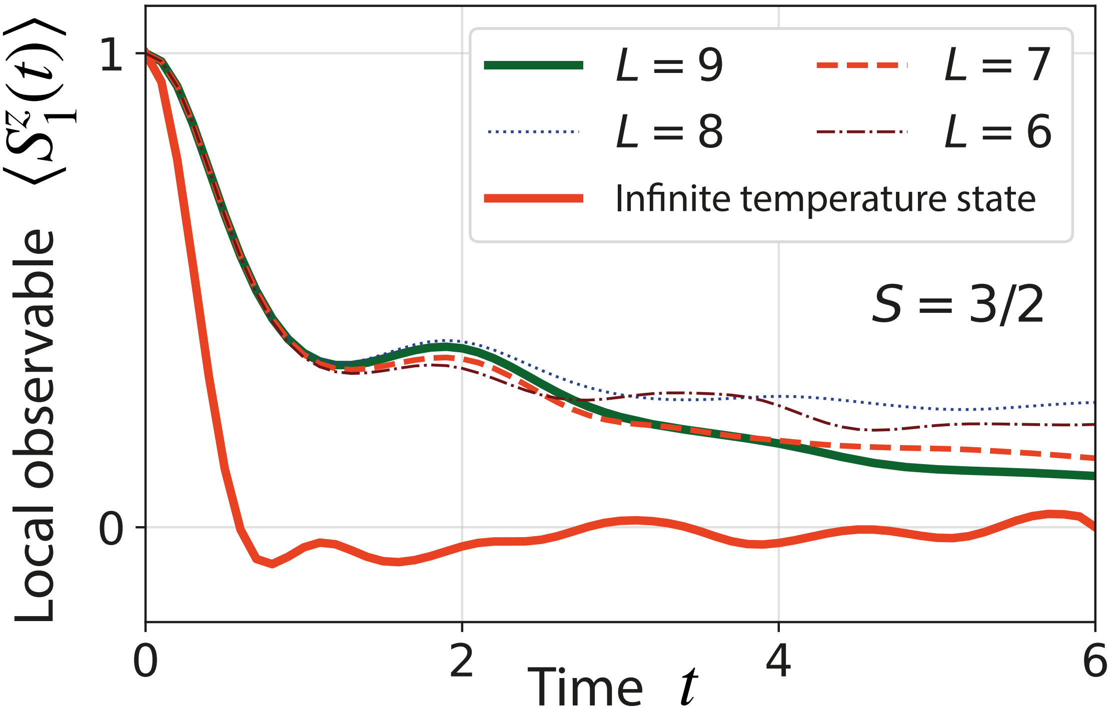

Figure 2-11: Thermalization dynamics of the observable $\langle \bar{S}_1^z(t) \rangle$ in case of fully polarized “up” states $|\Psi^{\rm up}\rangle$ and infinite temperature initial state $|\Psi^{\rm inf}\rangle$. In case of $|\Psi^{\rm up}\rangle$ initial states dynamics is calculated for different system sizes. Value of quantum spin $S = 3/2$ and $J = 0.91$. Dynamics of infinite temperature state is calculated for $L = 7$.

2.4.1 Results: Suppressed initial thermalization

We compute the thermalisation behavior of the observable $\langle \bar{S}_1^z(t)\rangle \equiv \langle S_1^z(t)\rangle/S$ for different values of S starting from the fully polarized state $|\Psi^{\rm up}\rangle$ given by Eq.(2.3). We also compute the thermalization of the same observable starting from a more generic initial condition where the spin S_z^1 is fully polarised, but the rest of the system is in the infinite temperature state. The latter initial state reads $|\Psi^{\rm inf}\rangle = |S\rangle_1 \otimes |{\rm inf}\rangle_{L-1}$, where $|{\rm inf}\rangle_{L-1}$ is a pure state sampled to represent the infinite temperature equilibrium [1].

The dynamics of $\langle \bar{S}_1^z(t)\rangle$ for $S = 1/2, 1, 3/2, 2$ is plotted in Fig.2-10. There one can observe that the thermalisation process for $S \geq 3/2$ starting from the initial condition $|\Psi^{\rm up}\rangle$ is noticeably slower than the the one starting from $|\Psi^{\rm inf}\rangle$. Such a difference makes one suspect that atypical scarlike eigenstates are prominently present in the expansion of $|\Psi^{\rm up}\rangle$. At the same, the difference between the two thermalization curves for $S = 1/2$ is rather small — suggestive of the absence of scarlike states in the expansion of $|\Psi^{\rm up}\rangle$. The case of $S = 1$ is a transitional between $S = 1/2$ and $S \geq 3/2$.

Figure 2-11 further illustrates the anomalous slowdown of the thermalization for spin-3/2 chains as a function of chain length L. The coincidence of the initial slowed-down behavior for the chains of different lengths indicates that the slowdown of the thermalization process starting from the state $|\Psi^{\rm up}\rangle$ is a feature that is also present in the thermodynamic limit $L \to \infty$ irrespective of whether or not the system still possesses the scarlike energy eigenstates in that limit.

2.4.2 Results: Finite-size quantum scars

In this section we calculate the bipartite entanglement entropy $\mathcal{E}(|E_n\rangle)$ between the sites from 1 to $L/2$ (rounded down for odd L) and the rest of the chain, for every eigenstate $|E_n\rangle$. To conveniently compare $\mathcal{E}(|E_n\rangle)$ between different system

---

[1] Infinite-temperature state is defined as $|{\rm inf}\rangle = \sum_{n=1}^{N} c_n |b_n\rangle$, here $|b_n\rangle$ are basis vectors and $c_n = |c_n| e^{i\phi_n}$ are complex amplitudes with phases chosen randomly from the interval $[0, 2\pi)$ and absolute values chosen from the distribution $P(|c_n|^2) = N e^{-N|c_n|^2}$, where N is the dimension of the Hilbert space (see Ref.[67, 68])

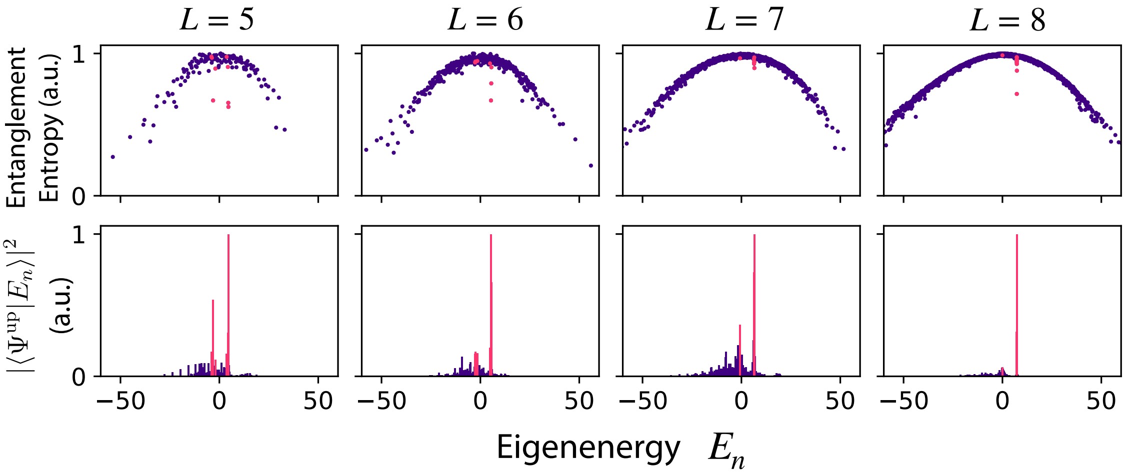

Figure 2-12: Top row: normalized half-chain entanglement entropy $\overline{\mathcal{E}}(|E_n\rangle)$ versus eigenenrgies E_n in a zero momentum sector. $S = 3/2$ and system sizes $L = 5, 6, 7, 8$. Bottom row: normalized overlaps $\bar{\mathcal{F}}_n$ of fully polarized "up" state $|\Psi^{\mathrm{up}}\rangle$ with eigenstates $|E_n\rangle$. Magenta points correspond to first several eigenstates with higest overlapls with $|\Psi^{\mathrm{up}}\rangle$.

$\overline{\mathcal{E}}(|E_n\rangle) = \mathcal{E}(|E_n\rangle)/\mathcal{E}_{\max}$, where $\mathcal{E}_{\max} = \max_{|E_n\rangle} \mathcal{E}(|E_n\rangle)$.

First, we scan the systems of $S = \frac{1}{2}$ for eigenstates with low entanglement entropy. We consider values of $J \in [0.4, 3]$ and system sizes $L = \overline{5, 18}$. We find that for these conditions, $\overline{\mathcal{E}}(|E_n\rangle)$ quickly converges to 1 in the middle of the spectrum with no outliers at all. This result is by no means surprising because (2.1) is far from integrability and supposed to satisfy the Eigenstate Thermalization Hypothesis in the thermodynamic limit.

As we increase the value of quantum spin S the system still comes to an agreement with ETH but not as quickly as in case of $S = 1/2$. Indeed, once we consider $S > \frac{1}{2}$, for some values of J we start observing special eigenstates $|\mathrm{FSQS}\rangle_j$ close to the middle of the spectrum, which normalized Entanglement Entropy $\overline{\mathcal{E}}(|\mathrm{FSQS}\rangle_j)$ is significantly lower than 1. We refer to the states $|\mathrm{FSQS}\rangle_j$ as to "Finite Size Quantum Scars" or FSQS, index $j = \overline{1, K}$ enumerates these states. The number of FSQS states K is typically small $K = 3 - 10$, whereas for the rest of the eigenstates in the middle of the spectrum, we also observe great convergence of $\overline{\mathcal{E}}(|E_n\rangle)$ to one.

As an example of FSQS states, let us consider the case of $S = \frac{3}{2}$. In the top row of the Fig. 2-12 we see that for the majority of eigenstates near the middle of the spectrum, values of $\overline{\mathcal{E}}(|E_n\rangle)$ are close to one, yet there are several pronounced outliers corresponding to the $|\text{FSQS}\rangle_j$ states. FSQS states are noticeably different from the majority of eigenstates near the middle of the spectrum. We will show further that FSQS states have a significant impact to the dynamics of $|\Psi^{\text{up}}\rangle$ states.

FSQS states are connected with fully polarized states $|\Psi^{\text{up}}\rangle$ as follows. The most pronounced outlier of Entanglement Entropy $|\text{FSQS}\rangle_{\text{max}}$ corresponds to the maximal overlaps of $|\Psi^{\text{up}}\rangle$ state with eigenstates:

$$|\text{FSQS}\rangle_{\text{max}} = \text{argmax}_{|E_n\rangle} |\langle\Psi^{\text{up}}|E_n\rangle|. \tag{2.11}$$

In the bottom row of the Fig. 2-12 we plot normalized overlaps $\bar{\mathcal{F}}_n = |\langle\Psi^{\text{up}}|E_n\rangle|/\mathcal{F}_{\text{max}}$, where $\mathcal{F}_{\text{max}} = \max_{|E_n\rangle} |\langle\Psi^{\text{up}}|E_n\rangle|$. Thus $\bar{\mathcal{F}} = 1$ corresponds to the maximal overlap of $|\Psi^{\text{up}}\rangle$ with eigenstates. We observe the same picture for $S = 1$ and $S = 2$, see Fig 2-13.

From finite size scaling we see that the maximal overlap $|\langle\Psi^{\text{up}}|E_n\rangle|$ naturally goes to zero with the system size L, yet it always corresponds to the $|\text{FSQS}\rangle_{\text{max}}$ state. The value of $\overline{\mathcal{E}}(|\text{FSQS}\rangle_{\text{max}})$ also converges to 1 in the thermodynamic limit, which is in agreement with the fact that the system is non-integrable and eventually supposed to satisfy ETH. In this regard, FSQS states do not violate ETH like genuine quantum many-body scars, yet as we will show further, their presence in finite-size systems is sufficient to suppress initial thermalization even in the thermodynamic limit.

FSQS states can be viewed as remnants of classical periodic trajectories. In a large S limit, quantum spins are expected to demonstrate classical-like behavior. Therefore such systems should possess periodic trajectories with short period T, meaning that the wavefunction $|\Psi^{\text{up}}(t)\rangle$, shall repeat itself after this period such that $|\langle\Psi^{\text{up}}(0)|\Psi^{\text{up}}(T)\rangle| \to 1$. On the other hand, quantum spins $S = \frac{1}{2}$ is the limit opposite to classical spins. In this limit, the very concept of trajectory does not have much sense, thus, “quantumness” is destroying periodic trajectories.

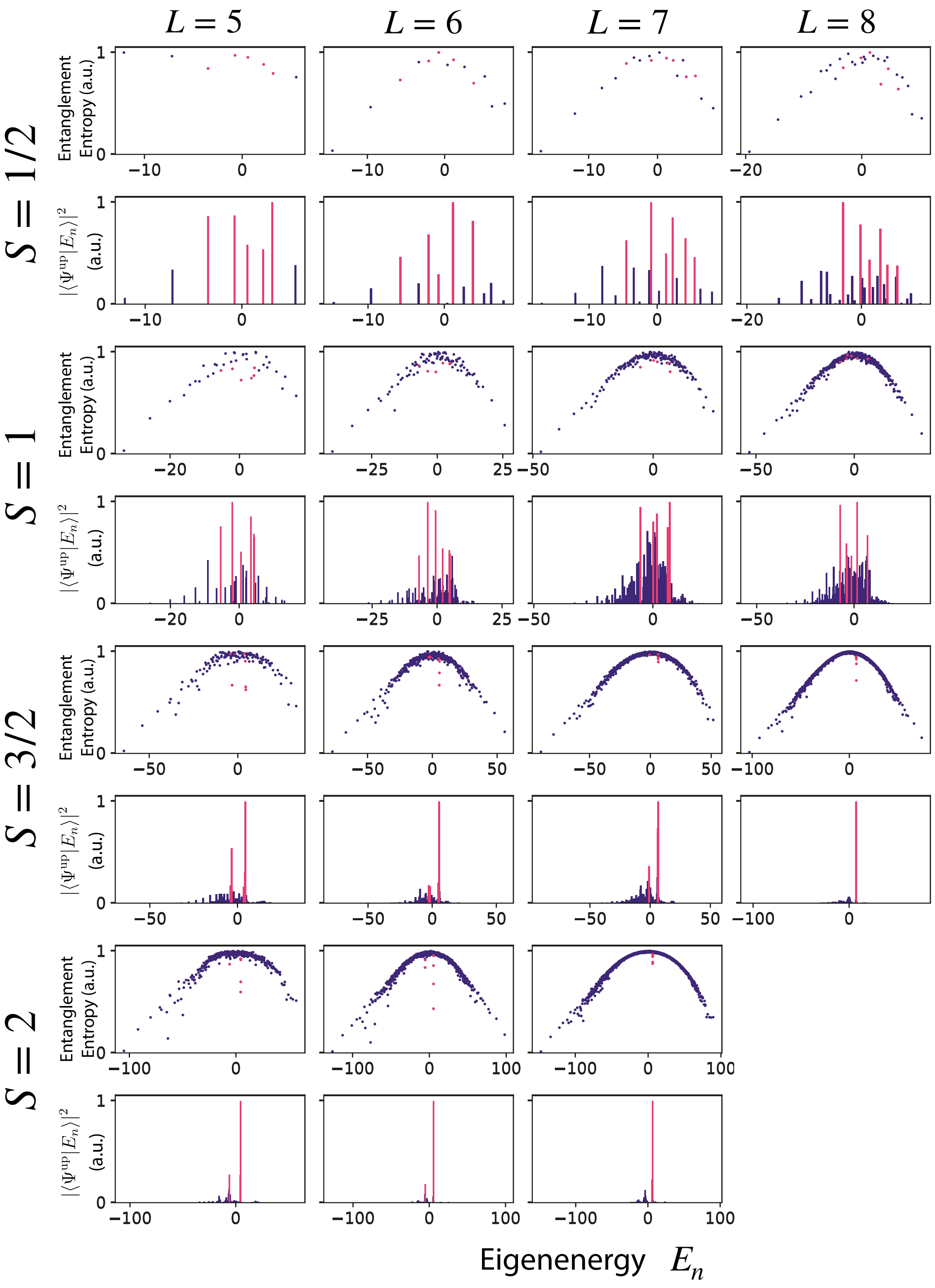

Figure 2-13: Normalized half-chain entanglement entropy $\overline{\mathcal{E}}(|E_n\rangle)$ versus eigenenergies E_n in a zero momentum sector and normalized overlaps $\bar{\mathcal{F}}_n$ of fully polarized "up" state $|\Psi^{\rm up}\rangle$ with eigenstates $|E_n\rangle$. For system sizes $L = 5, 6, 7, 8$ and for different S. Magenta points correspond to first 6 eigenstates with highest overlaps with $|\Psi^{\rm up}\rangle$. The value is fixed as $J = 1.76$.

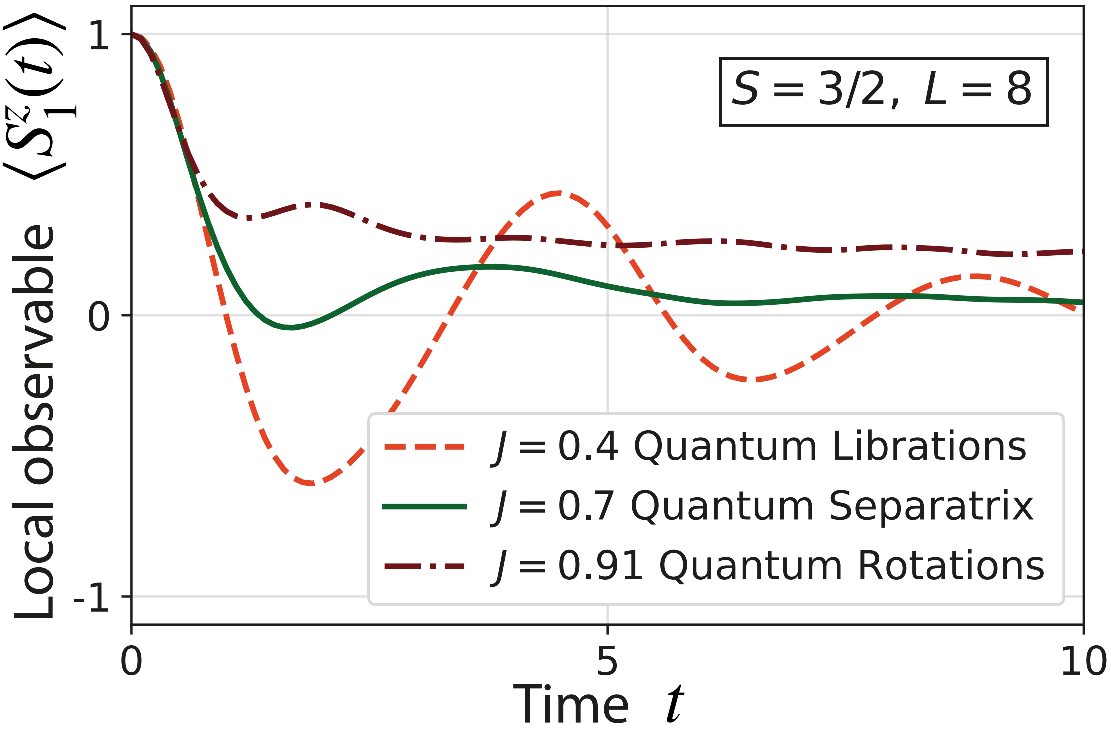

Figure 2-14: Time-evolution of a single spin $\langle \bar{S}^z_1(t) \rangle$ for $|\Psi^{\mathrm{up}}\rangle$ for different values of J in case of $S = 1$ and $L = 10$.

2.4.3 Results: Quantum separatrix

It was shown in the previous section that classical separatrix corresponding to $J = J^*$ distinguishes between two different regimes of motion. Analogously to the classical picture let us take a look at the dynamics of $\langle \bar{S}^z_1(t) \rangle$ for different J in case of $|\Psi^{\mathrm{up}}\rangle$ initial state. From the Fig. 2-14, we can distinguish between clearly between the oscillatory behaviour of $\langle \bar{S}^z_1(t) \rangle$ which we refer as "quantum librations", and between slowly thermalizing "quantum rotations" when $\langle \bar{S}^z_1(t) \rangle > 0$ for sufficiently long time. We can find a value of $J = J_Q$, such that the corresponding dynamics of $\langle \bar{S}^z_1(t) \rangle$ is neither oscillating nor slowly thermalizing. We refer to the value of J_Q as "quantum separatrix".

Same as in classical case "quantum librations" correspond to $J < J_Q$ whereas "quantum rotations" correspond to $J > J_Q$. When J is in the vicinity of separatrix J_Q the observable $\langle \bar{S}^z_1(t) \rangle$ thermalizes almost as quickly as in the case of an infinite temperature state. This is in agreement with the classical picture when periodic motion gets extra unstable in the vicinity of the separatrix.

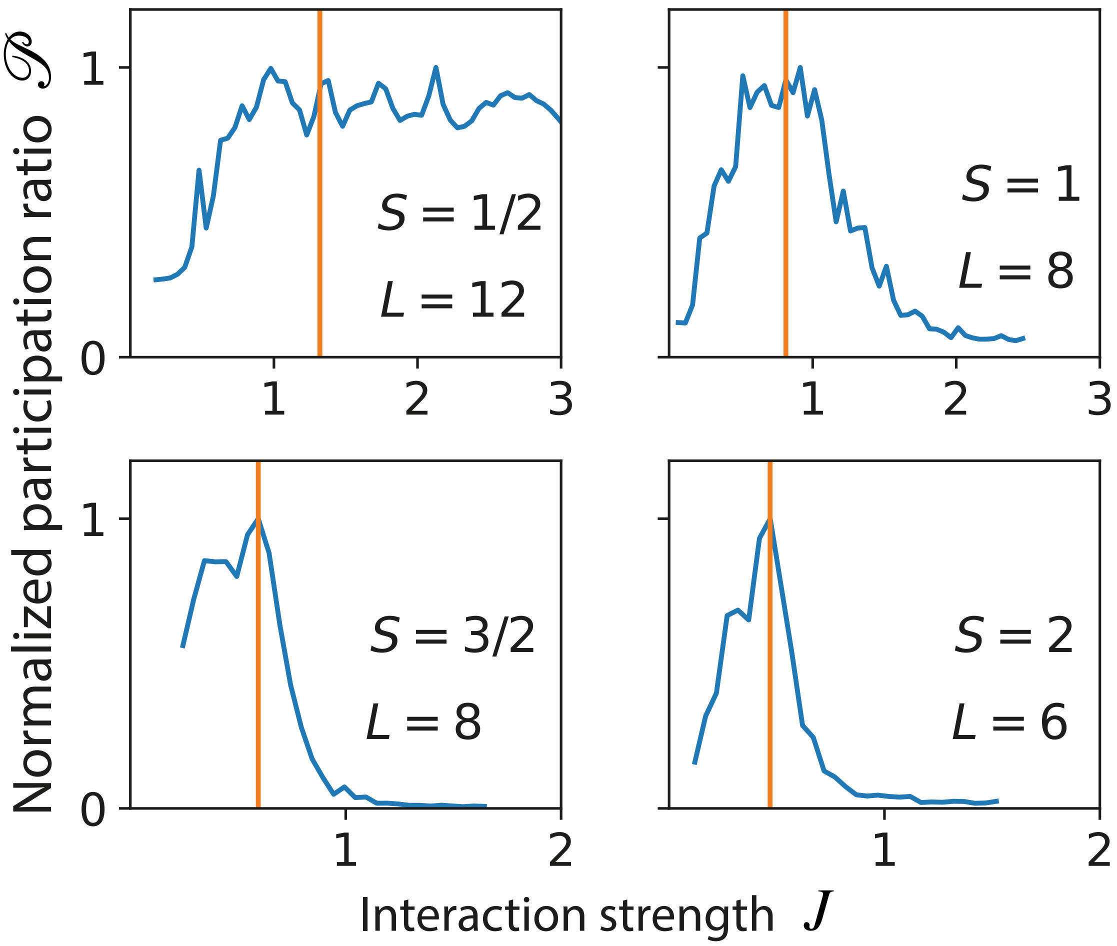

Figure 2-15: Normalized participation ratio $\bar{\mathcal{P}}$ vs J for different values of $S = 1/2, 1, 3/2, 2$. Vertical lines correspond to the values of separatrix $J^*/\sqrt{S(S+1)}$ predicted classically with $J^* = 1.15$.

It is remarkable that the approximate value of J_Q corresponding to the quantum separatrix may be obtained from the classical one J^* as $J_Q \simeq J^*/\sqrt{S(S+1)}$. In order to demonstrate this, let us introduce participation ratio:

$$\mathcal{P} = 1\Big/\sum_{n=1}^{\mathcal{N}} |\langle \Psi^{\text{up}}|E_n\rangle|^4, \tag{2.12}$$

where $\mathcal{N}$ is the number of eigenstates in a zero-momentum sector. Participation ratio $\mathcal{P}$ counts the number of states which are accessible from the initial state $|\Psi^{\text{up}}\rangle$, thus it can be utilized to characterize its stability. Indeed, if $\mathcal{P}$ is of the order of $\mathcal{N}$ it means that $|\Psi^{\text{up}}(t)\rangle$ decomposes into a superposition of an exponential number of eigenstates with approximately equal amplitudes. Thus the fidelity $|\langle \Psi^{\text{up}}(0)|\Psi^{\text{up}}(t)\rangle| \to 0$ at exponential rate. On the contrary, if $\mathcal{P} \ll \mathcal{N}$, it will result in oscillations of fidelity and thus in slower thermalization of local observables such as $\langle \bar{S}_1^z(t)\rangle$.

Let us study the dependence of $\mathcal{P}(J)$ on J for different S. To conveniently compare different systems let us use the normalized quantity $\bar{\mathcal{P}}(J) = \mathcal{P}(J)/\mathcal{P}_{\text{max}}$, where $\mathcal{P}_{\text{max}} = \max_J \mathcal{P}(J)$. In Fig. 2-14 we plot $\bar{\mathcal{P}}(J)$ for different S and classically predicted values $J^*/\sqrt{S(S+1)}$ as vertical lines. We immediately observe that, for $S = 3/2$ and $S = 2$, the maxima of $\bar{\mathcal{P}}(J)$ approximately coincides with $J^*/\sqrt{S(S+1)}$ with a good precision. Further, we observe that for $S = 1$ there is no pronounced maximum of $\bar{\mathcal{P}}(J)$, instead, we observe some intervals of J corresponding to the maximal values of $\bar{\mathcal{P}}(J)$. Nevertheless, the classically predicted value falls within this interval. Lastly, we see that, in the case of $S = 1/2$, there is no maximum of $\bar{\mathcal{P}}(J)$ at all, and the system does not enter the regime of quantum rotations. This last observation is in agreement with the fact that we found no FSQS states for systems of $S = 1/2$.

Similarly to the classical results presented in Fig. 2-3, we see that for $S > 1/2$, the state which corresponds to the classical periodic trajectory $|\Psi^{\text{up}}\rangle$ is most unstable near the separatrix and gets more and more stable as J increases. This behaviour is quite opposite to the stability of $\langle S_1^z(t)\rangle$ for $|\Psi^{\text{inf}}\rangle$ initial state. In the latter case the thermalization time of $\langle S_1^z(t)\rangle$ decreases linearly with J similarly to the "ergodic" Lyapunov exponent λ_{max}.

2.4.4 Dynamics of entanglement entropy

In section 2.4.2 we used the value of entanglement entropy for the eigenstates of the system as the test of ETH. The entanglement entropy of the system as such was not the principal concern of the present investigation: instead we could have used the expectation value of a different physical observable, for example, the expectation value of S_1^x. Yet, in this subsection, for the sake of completeness, we present the time-evolution of entanglement entropy for initial state $|\Psi^{\text{up}}\rangle$.

In the Figure 2-16, we plot normalized entanglement entropy $\mathcal{E}(|\Psi(t)\rangle/\log\mathcal{M}$, where $\mathcal{M}$ is the dimensionality of the Hilbert space of subsystem. We investigated the entanglement entropies of a single spin and of a half of the chain ($\frac{L}{2}$ spins for even L, and $\frac{L-1}{2}$ spins for odd L). In both cases we see that $\mathcal{E}(|\Psi(t)\rangle/\log\mathcal{M}$ slowly converges to some saturation value, which in its turn close to 1. Initially $\mathcal{E}(|\Psi(t)\rangle/\log\mathcal{M}$ exhibits linear growth, which is slowed down after some time.

2.5 Lyapunov exponents: technical details

2.5.1 Calculation of the larges Lyapunov exponent for ergodic motion

The full form of equations (2.4) reads:

$$\begin{aligned}
\frac{dS_j^x}{dt} &= S_j^z + 2J(S_{j-1}^y + S_{j+1}^y)S_j^z, \\
\frac{dS_j^y}{dt} &= S_j^z + J(S_{j-1}^x + S_{j+1}^x)S_j^z, \\
\frac{dS_j^z}{dt} &= S_j^y + J(S_{j-1}^x + S_{j+1}^x)S_j^y \\
&\quad - S_j^x - 2J(S_{j-1}^y + S_{j+1}^y)S_j^x.
\end{aligned} \tag{2.13}$$

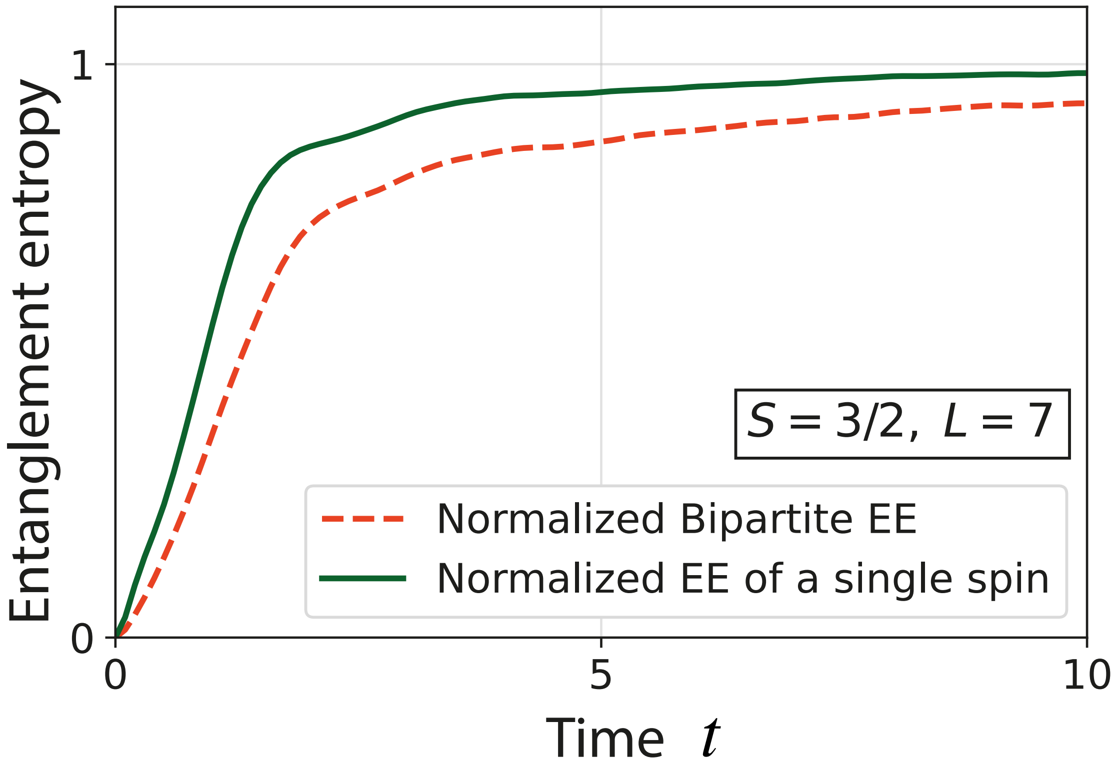

Figure 2-16: Time-evolution of entanglement entropy for initial $|\Psi^{\text{up}}\rangle$ state. Entanglement is normalized by the quantity $\log \mathcal{M}$, where $\mathcal{M}$ is total number of states in subsystem. For a single spin $S = 3/2$, $\mathcal{M} = 4$, for the chain of three spins (bipartite division) $\mathcal{M} = 4^3$.

In general the solution of this system is a $3L$-dimensional vector $\mathcal{X}(t) = \{\mathbf{S}_i(t)\}_{i=1}^{L}$. Let us first calculate the value $\lambda_{\max}$, which corresponds to the maximal value of the Lyapunov spectrum of (2.1). To calculate $\lambda_{\max}$ we employ standard procedure described, for example, in [61, 62]. Let us briefly recapitulate the main steps of this procedure.

1. Fix the values of the initial error d_0, reset time T_R, and a number of resets M.
2. Pick initial conditions $\mathcal{X}(0) = \{\mathbf{S}_i(0)\}_{i=1}^{L}$ as a random configurations of spins $\mathbf{S}_i(0)$. Perturb initial conditions by a random vector of small length $\|\delta R\| = d_0$.
3. By solving (2.13) obtain two trajectories $\mathcal{X}_1(T_R)$ and $\mathcal{X}_2(T_R)$ for initial conditions $\mathcal{X}(0)$ and $\mathcal{X}(0) + \delta R$ correspondingly, up to the reset time T_R. Evaluate the distance between them $d_1 = \|\mathcal{X}_1(T_R) - \mathcal{X}_2(T_R))\|$.
4. As a new initial conditions take $\mathcal{X}(0) = \mathcal{X}_1(T_R)$, and as a displacement vector take a vector with a direction along $\delta R = \mathcal{X}_2(T_R) - \mathcal{X}_1(T_R)$ and renormalize it such that preserves direction, but its norm $\|\delta R\| = d_0$.
5. Obtain new trajectories $\mathcal{X}_1(T_R)$ and $\mathcal{X}_2(T_R)$, and the distance between them $d_n = \|\mathcal{X}_1(T_R) - \mathcal{X}_2(T_R))\|$, here index n corresponds to the number of performed resets
6. Go to step 4 and repeat it until $n = M$ resets.
7. Calculate $\lambda_{\max}$ by using the following formula:

$$\lambda_{\max} = \frac{1}{MT_R} \sum_{n=1}^{M} \log \left| \frac{d_n}{d_0} \right| . \tag{2.14}$$

The maximal Lyapunov exponent $\lambda_{\max}$ converges constant value with M. In principle one must set the values of $d_0 \to 0$ and $T_R \to \infty$. However, in practice, we are limited to finite numbers. The value of $\lambda_{\max}$ should not depend on the values of d_0 and T_R, however if T_R is too large the distance between trajectories

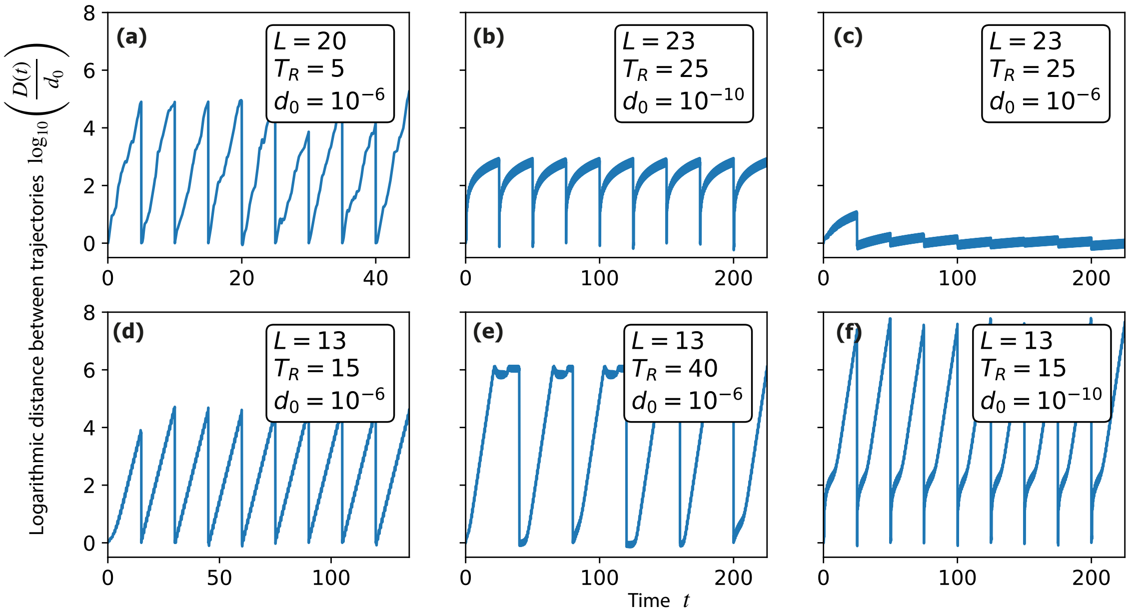

Figure 2-17: Logarithmic growth of the distance between trajectories $\log_{10}\left(\frac{D(t)}{d_0}\right)$ for $J = 1.76$, and different reset times T_R initial errors d_0 and lengths L. (a) Random initial conditions corresponding to the $\lambda_{\max} \simeq 1.17$ (b-f) Periodic initial conditions. (b-c) $\lambda_p = 0$ stable periodic trajectory. (d,f) $\lambda_p = 0.351$, periodic trajectory is unstable. (e) same as (d), but reset time T_R is too big.

$d(t) = \|\mathcal{X}_1(t) - \mathcal{X}_2(t))\|$ can reach saturation because of finite size of the phase space. The growth of the distance $d(t)$ is shown in Fig. 2-17 (a).

Below are values of $\lambda_{\max}$ for the Hamiltonian (2.1) in case $h = 1$, $L = 100$ and different J.

J	0.79	1.15	1.76
$\lambda_{\max}$	0.512	0.76	1.18

2.5.2 Calculation of the largest Lyapunov exponent for periodic motion

The many-body periodic trajectory $\mathcal{S}_p(t)$ is perfectly periodic and thus stable. However, this trajectory can be practically implemented neither in experiment nor in computer simulations. Indeed in both of the above cases we can set up initial conditions (and all the other parameters) only with some finite precision. In the case of chaotic systems, any finite discrepancy between initially close trajectories may lead to the exponential growth of the distance between these trajectories. For this reason we shall distinguish between the stable "perfectly periodic" trajectory $\mathcal{S}_p(t)$ and practically implemented trajectory $\mathcal{S}(t)$ which we just refer as "periodic".

The practical algorithm for calculating λ_p is similar to the one used for calculating $\lambda_{\max}$. The main difference is that instead of calculating the dynamics of two trajectories simultaneously, we fix a reference trajectory $\mathcal{S}_p(t)$, which is perfectly periodic. Below we provide the step-by-step algorithm for calculating λ_p:

1. Fix the values of the initial error d_0, reset time T_R, and the number of resets M.

2. Generate a displacement vector δR randomly directed in a phase space, with the norm $\|\delta R\| = d_0$.

3. On the n-th reset, $n = 1, \ldots, M$, obtain a trajectory $S(T_R)$ corresponding to the initial conditions $\mathcal{S}(0) = \mathcal{S}_p((n-1)T_R) + \delta R$. Evaluate the divergence of this trajectory from the periodic one $d_n = \|\mathcal{S}(T_R) - \mathcal{S}_p(nT_R)\|$.

4. Perform a reset: update the displacement vector as $\delta R = \mathcal{S}(T_R) - \mathcal{S}_p(nT_R)$, and renormalize it such that $\|\delta R\| = d_0$. Go to the step 3 until $n = M$.

5. Evaluate λ_p by using the formula:

$$\lambda_p = \frac{1}{MT_R} \sum_{n=1}^{M} \log \frac{d_n}{d_0}. \tag{2.15}$$

Let us note that values of λ_p calculated by the above algorithm are always positive because of finite values of M and d_0, which ideally should be set to infinity and zero correspondingly. To distinguish zero Lyapunov exponents $\lambda_p \to 0$ from finite but small ones, we shall look at the dependence of λ_p on the reset time T_R. In the case of finite Lyapunov, exponents λ_p do not depend on the reset time as long as it is not too big. When λ_p decreases with T_R as $\lambda_p \sim \log T_R / T_R$, it means that it actually converges to zero, and therefore there is no exponential instability of the trajectory.

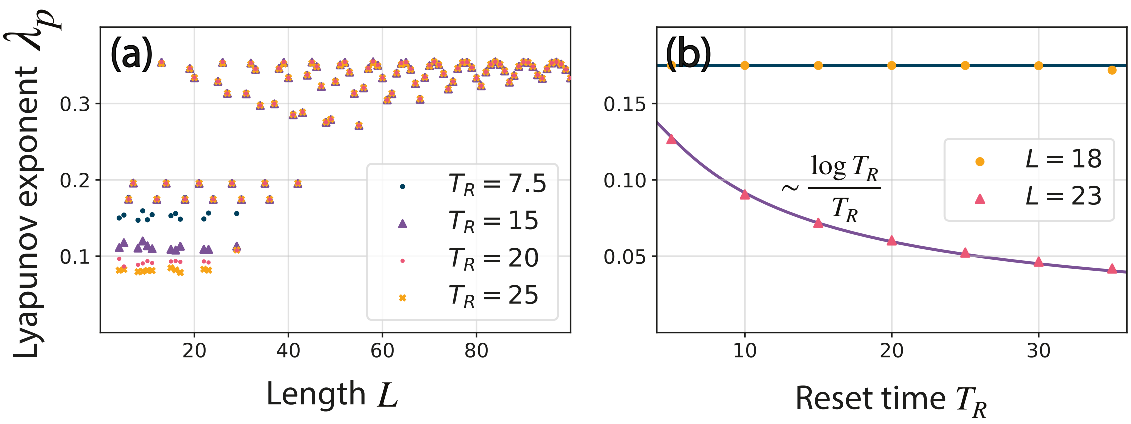

Figure 2-18: (a) Periodic Lyapunov exponents λ_p for different system sizes L and different reset times T_R. (b) λ_p vs T_R for stable $L = 23$ and unstable $L = 18$ periodic motion.

2.6 Summary and discussion

2.6.1 Summary of the classical results

1. Periodic trajectories can remain stable in fairly large finite systems but not in the thermodynamic limit.

2. Instability of periodic orbits often leads to the spontaneous formation of states that we call “time-quasicrystals”: these states exhibit *quasiperiodic* dynamics in time and broken translational symmetry in space. Time quasicrystals typically appear as long-lived transient regimes followed by a transition to an ergodic regime, but in some cases, they are found to be stable to the extent our numerical simulations afford. The observed connections between periodic, quasiperiodic, and ergodic regimes are summarised in Fig.2-1.

3. The largest Lyapunov exponents around an initial periodic trajectory exhibit a nontrivial dependence on the size of the system.

4. The periodic trajectories exhibit two topologically different regimes, which we name “librations” and “rotations” by analogy with the similar-called regimes of a pendulum.

2.6.2 Discussion of the classical results

We have demonstrated that the fate of classical periodic trajectories in spin systems is a rather rich subject. The stability of periodic motion depends crucially on whether it is in the regime of librations or rotations. The regime's choice is determined by the magnitude of the interaction strength between spins. Lower interaction strength leads to librations when the trajectory oscillates between the poles, and higher interaction strength leads to rotations when the trajectory is confined inside the upper hemisphere. There is also a value of interaction strength which corresponds to the separatrix distinguishing between librations and rotations. We discovered that librations are always unstable, except for a few marginal cases. The rotations, on the contrary, demonstrate better (often perfect) stability, especially for higher interaction strength. Periodic trajectories near separatrix demonstrate extraordinary instability; in particular, they are even less stable than randomly selected many-body trajectories.

We have calculated "periodic" Lyapunov exponents around perfectly periodic trajectories to characterize their stability. We have discovered the non-universal dependence of periodic Lyapunov exponent on the system size. We presented many examples when the periodic motion in a system of bigger size is perfectly stable, whereas it is unstable in a system of a significantly smaller size. Such behavior is somewhat counterintuitive. Indeed in many-body problems, one can reasonably expect that adding extra degrees of freedom will only make stability worse, not better. Surprisingly our example with periodic trajectories demonstrates that such logic is not always correct.

In the regime of rotations, as system size increases, periodic Lyapunov exponents slowly converge to its saturation values. Furthermore, they exhibit long-lasting quasiperiodic damped oscillations around these values. Such behavior is atypical for Lyapunov exponents, which are usually regarded as intensive quantities. Another manifestation of non-universality is that if the system size is a multiple of 6, then the periodic motion is always unstable in such a system, regardless of the interaction strength. While in all the other cases, one can always choose interaction strength big enough to make a periodic trajectory stable.

We have also uncovered the existence of a quasiperiodic regime that spontaneously breaks time-space translational invariance. Trajectory in a quasiperiodic regime often has a longer lifetime than the periodic trajectory it originated from. The dynamics of the discovered quasiperiodic regime is neither periodic nor ergodic. One can always make quasiperiodic regime stable by increasing interaction strength. In this regard, this lower symmetry regime is indeed more stable than some periodic trajectories.

The above results about periodic trajectories were obtained for the specific setting. Nevertheless, we believe they are extendable for a broader class of non-integrable translationary invariant Hamiltonians.

2.6.3 Summary of the quantum results

For quantum spin lattices, we find that the signatures of periodic classical dynamics are largely absent for spin-1/2 lattices but then appear already for spin-1 lattices and become rather prominent for spins 3/2 and higher. These signatures include:

Signature 1: Slowdown of the initial relaxation that survives in the thermodynamic limit.

Signature 2: Finite-size quantum scars, which means the eigenstates in finite systems with anomalously low entanglement entropy. The state are prominently present in the initial quantum states corresponding to the classically periodic motion.

Signature 3: Presence of two regimes – quantum librations and quantum rotations with a separatrix between them.

2.6.4 Discussion of the quantum results

Our work has been driven by the idea of studying how stable short-period trajectories in classical spin chains can manifest themselves in the quantum counterpart of the system, particularly in the case of higher quantum spins, when the system is expected to exhibit more classical-like features. We discover that quantum chains of spin $S > 1/2$ possess special ”Finite size quantum scars” FSQS eigenstates in the middle of the spectrum characterized by lower entanglement entropy. Furthermore, FSQS states are connected with fully polarized “up” states which results in suppressed initial thermalization of the latter on the level of local observables.

We calculated the dynamics of spin polarization in the case of fully polarized “up” initial states. We showed that thermalization of spin polarization is suppressed if the system possesses FSQS states. Although FSQS states can only be distinguished in the finite size systems, their impact on initial dynamics of fully polarized “up” states remains in the thermodynamic limit. In this regard, FSQS states play a bridging role between quantum scars in chaotic billiards [4], and genuine quantum many-body scars [51, 52].

It also turns out that in the case of $S > 1/2$, analogously to classical systems, one can distinguish between two regimes of motion for an initially fully polarized “up” state. Namely “quantum librations” in which spin polarization exhibits oscillatory behavior, and “quantum rotations” in which spin exhibits slow thermalization. Analogously to classical spins, the choice of the regime depends on the interaction strength between spins. Also, analogously to the classical picture, we have introduced a notion of “Quantum separatrix”, which distinguishes between two regimes of motion. In the case of quantum separatrix, fully polarized “up” states exhibit the quickest thermalization.

Another exciting discovery is that the value of interaction strength corresponding to the quantum separatrix can be predicted with good precision from the classical value. In other words, fully polarized “up” states in a quantum system can sense the existence of classical separatrix. Because of this remarkable property, periodic trajectories can also serve as a tangible connection between classical and quantum spin systems.

Chapter 3

Almost complete revivals

The content of this chapter is mostly based on the papers [1, 3].

3.1 States out of equilibrium at predetermined moment of time

Local observables of non-integrable quantum many-body systems are expected to quickly reach their equilibrium values. This process of reaching thermal equilibrium is also known as thermalization. It is also usually implied that once some observable has reached thermal equilibrium, it stays there practically forever, exhibiting only meaningless fluctuations upon its equilibrium value. There is however a number of physical mechanisms when thermalization is either slowed down or not present at all. Among such mechanisms are many-body localization [25], spin-glasses [9, 27], systems with long-range interactions [10, 11] or systems with constraints [8, 51, 52]. All these mechanisms, however, are associated with the properties of the system under consideration. An alternative approach to obtaining unusual thermalization patterns is to consider specially designed initial states without putting significant restrictions on the system itself.

One example of the latter kind was recently mentioned by Dymarsky [69]: namely, for an isolated many-body system, where a local observable $\hat{O}$ has equilibrium expectation value $\langle \hat{O} \rangle_{\mathrm{eq}} = 0$ but initially deviates from it, one can initiate a revival of

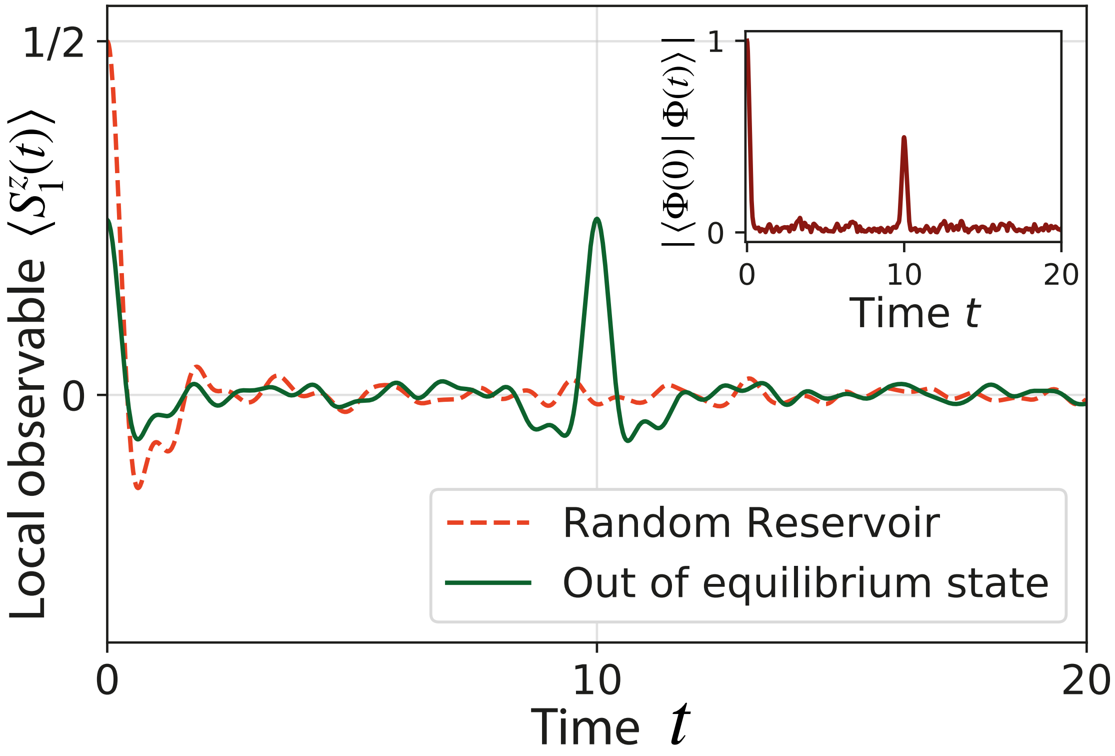

Figure 3-1: Time evolution of the local observable $\langle S_1^z\rangle$, for a system of $L = 12$ spins 1/2 governed by the Hamiltonian (2.1). The solid green line corresponds to the state (3.1) devised to obtain the revival at time $\tau = 10$, and the dashed orange line corresponds to the random reservoir (see the text). The inset shows the recovery in fidelity of the ACR state $|\langle\Phi_{\mathrm{ACR}}(0)|\Phi_{\mathrm{ACR}}(t)\rangle|$.

a non-equilibrium value of $\langle\hat{O}\rangle$ at any given moment of time τ by using the initial state:

$$|\tilde{\Psi}(0)\rangle = \frac{|\Psi(0)\rangle + |\Psi(-\tau)\rangle}{\sqrt{2}}, \tag{3.1}$$

where $|\Psi(0)\rangle$ is a many-body wave function representing a "conventional" nonequilibrium state such that $\langle\Psi(0)|\hat{O}|\Psi(0)\rangle$ is equal to its maximally possible value $\langle\hat{O}\rangle_{\max}$, and $|\Psi(-\tau)\rangle$ is the state that the system should have at time $t = -\tau$ in order to arrive to $|\Psi(0)\rangle$ at $t = 0$. For the initial state $|\tilde{\Psi}(0)\rangle$, both the initial value $\langle\hat{O}(0)\rangle$ and the revived one $\langle\hat{O}(\tau)\rangle$ are close to $\langle\hat{O}\rangle_{\max}/2$. An example of such behavior for a specific system is presented in Fig. 3-1.

In [1], we proposed a mechanism of constructing special initial states such that the selected local observable after relaxation exhibits almost complete revival (ACR)

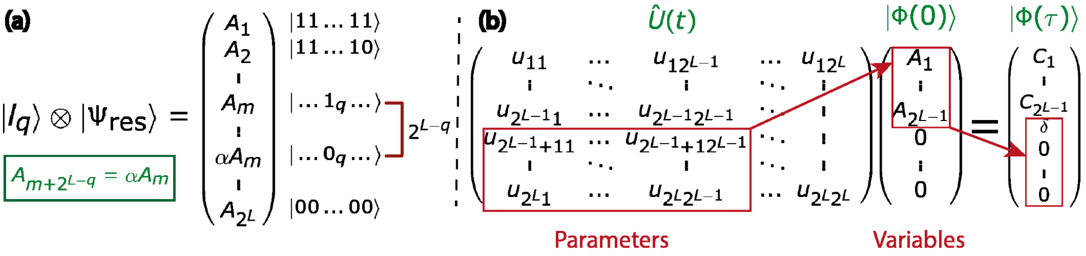

Figure 3-2: (a) Schematic representation of the ansatz (3.17) in the many-body Hilbert space. (b) Example of revival conditions (3.25) in case of $q = p = 1$ and $\vec{S}_1 = \vec{S}'_1 = (0, 0, 1/2)$. Matrix $\hat{V}$ coincides with the bottom-left submatrix u of size 2^{L-1}, states (3.17) and (3.20) have simple structure in the basis (3.16).

to its initial value at the predetermined moment of time. In a closed many-body system $C = A \cup B$ for a small subsystem A in a pure state, the rest of the system B usually serves as a thermal reservoir, which leads to the equilibration of A. However, the reservoir B can be finely tuned such that at some predetermined revival time τ, subsystem A will be out of equilibrium. So in fact, the reservoir can work both ways: thermalize the subsystem or, on the contrary, push it out of equilibrium. The latter, however, is an exponentially rare event, yet if one can have access to sufficiently many degrees of freedom of B, then the B can be tuned such that this event will take place at any desired time τ.

We also consider spin chains with spin $S > 1/2$, and show that in this case, ACR is suppressed by a factor $1/S$. This result agrees with the classical picture where the ACR is impossible due to the fact that classical spin chains are generally chaotic.

3.1.1 Revivals along z-axis

In this section, we construct the revival of spin polarization along z-axis because this case is particularly simple. The main idea of the ACR construction procedure is illustrated in Fig. 3-2 (b). A general prescription for constructing arbitrary revivals will be provided further.

Let us consider a lattice of L interacting spins 1/2 described by spin operators $\{S_i^\alpha\}$, where i is the lattice index and $\alpha = x, y, z$ the spin projection index. As a local observable, we choose the z-projection of the spin on an arbitrary site labeled by index 1, i.e., $\hat{O} = S_1^z$. We refer to the other $L - 1$ spins as the "reservoir".

Let us denote the bases of one-spin Hilbert spaces as $|1_i\rangle$ and $|0_i\rangle$, such that $\langle 1_i|S_i^z|1_i\rangle = 1/2$ and $\langle 0_i|S_i^z|0_i\rangle = -1/2$. We define the basis $\mathcal{B}$ for the entire lattice as $\mathcal{B} = \mathcal{B}^+ \cup \mathcal{B}^-$, where

$$\mathcal{B}^+ = \{|1_1\ 1_2 \dots 1_L\rangle,\ \dots\ , |1_1\ 0_2 \dots 0_L\rangle\}, \tag{3.2}$$

$$\mathcal{B}^- = \{|0_1\ 1_2 \dots 1_L\rangle,\ \dots\ , |0_1\ 0_2 \dots 0_L\rangle\}. \tag{3.3}$$

represent the subspaces with the first spin being "up" or "down" respectively. Each of the two subspaces thus has dimension $N = 2^{L-1}$. For the entire basis $\mathcal{B}$ we also use the notation $\{|\varphi_n\rangle\}$, where $n = 1, ..., N$ represents the basis $\mathcal{B}^+$ and $n = N+1, ..., 2N$ the basis $\mathcal{B}^-$.

We search for the ACR state such that it initially has the form of a tensor product $|\Phi_{\text{ACR}}(0)\rangle = |1_1\rangle \otimes |\Psi_{\text{res}}\rangle$, where $|\Psi_{\text{res}}\rangle$ is the state of the reservoir. Such a state can be parameterized as

$$|\Phi_{\text{ACR}}(0)\rangle = \sum_{n=1}^{N} A_n |\varphi_n\rangle, \tag{3.4}$$

where A_n are the complex amplitudes to be determined later. As follows from our indexing convention, amplitudes A_n have non-zero values only for the basis states belonging to $\mathcal{B}^+$. This choice guarantees that $\langle S_1^z(0)\rangle$ is equal to its maximum possible value $\langle S_1^z\rangle_{\max} = 1/2$.

To obtain ACR at time τ, we now find such A_n that $|\Phi_{\text{ACR}}(\tau)\rangle$ has the form:

$$\begin{aligned} |\Phi_{\text{ACR}}(\tau)\rangle \ &\equiv\ e^{-i\mathcal{H}\tau}|\Phi_{\text{ACR}}(0)\rangle \\ &=\ \sum_{n=1}^{N} C_n|\varphi_n\rangle \ +\ \delta\ |\varphi_{N+1}\rangle, \end{aligned} \tag{3.5}$$

where $\mathcal{H}$ is the Hamiltonian of the system, while $\{C_n\}$ and δ are some complex amplitudes. The principal feature of the ansatz (3.5) is that only one of N basis vectors of $\mathcal{B}^-$ participates in the expansion with amplitude δ, while the basis $\mathcal{B}^+$ is fully represented by the set of amplitudes $\{C_n\}$. As we show below, this leads to the ACR.

Ansatz (3.5) implies an unambiguous prescription for finding $\{A_n\}$, $\{C_n\}$, and δ. In order to do this, one needs first to define the matrix u_{mn} of the time evolution operator $u \equiv e^{-iH\tau}$ in the basis $\mathcal{B}$. Then, to make sure that only state $|\varphi_{N+1}\rangle$ from the subspace $\mathcal{B}^-$ contributes to $|\Phi_{\text{ACR}}(\tau)\rangle$ one needs to satisfy the following system of N equations:

$$\begin{cases} u_{N+1,1}A_1 + \cdots + u_{N+1,N}A_N = \delta \\ u_{N+2,1}A_1 + \cdots + u_{N+2,N}A_N = 0 \\ \cdots \\ u_{2N,1}A_1 + \cdots + u_{2N,N}A_N = 0. \end{cases} \tag{3.6}$$

From this system one can find N variables $\{A_n\}$ as a function of yet unknown parameter δ, and then find δ by normalizing $\{A_n\}$. Finally, one can substitute the result into the system of equations

$$\begin{cases} u_{1,1}A_1 + \cdots + u_{1,N}A_N = C_1 \\ u_{2,1}A_1 + \cdots + u_{2,N}A_N = C_2 \\ \cdots \\ u_{N,1}A_1 + \cdots + u_{N,N}A_N = C_N, \end{cases} \tag{3.7}$$

thereby obtaining the set of amplitudes $\{C_n\}$.

The central result of the present work is that the above prescription implies ACR because, generically, the values $|\delta|$ and all $|C_n|$ are of the order of $1/\sqrt{N}$, and, as a result,

$$\langle S_1^z(\tau)\rangle = \frac{1}{2}\left(\sum_{i=1}^{N} |C_i|^2 - |\delta|^2\right) = 1/2 - \mathcal{O}(1/N), \tag{3.8}$$

which, in turn, means that the revived $\langle S_1^z(\tau)\rangle$ is exponentially close to $\langle S_1^z\rangle_{\max}$.

3.1.2 Estimation of revival's imperfection

While the estimate $|C_n| \sim 1/\sqrt{N}$ in the above construction is by no means surprising, the generic validity of $\delta \sim 1/\sqrt{N}$ requires a justification. Our justification is based mainly on the direct numerical solution of the system (3.6), but also it is supported by the following analytical argument.

The argument is based on the assumption that, in a generic non-integrable system, the time evolution operator u for sufficiently large times τ is similar to a random rotation in the $2N$-dimensional Hilbert space. The matrix u_{mn} can then be viewed as being composed of a set of $2N$ normalized vectors $\{u_{1n}\}$, $\{u_{2n}\}$, etc., where the typical matrix element has absolute value $|u_{mn}| \sim 1/\sqrt{2N}$ and a largely random phase. The system of equations (3.6) involves only half of the components of each vector $\{u_{N+1,n}\}$, $\{u_{N+2,n}\}$, etc. It implies that the N-dimensional vector $\{A_n^*\}$ must be orthogonal to $N-1$ "half-vectors" $\{u_{N+2,n}\}$, ..., $\{u_{2N,n}\}$, while the value of δ is the projection of the half-vector $\{u_{N+1,n}\}$ onto the direction of $\{A_n^*\}$. If the half-vector $\{u_{N+1,n}\}$ were uncorrelated with "half-vectors" $\{u_{N+2,n}\}$, ..., $\{u_{2N,n}\}$, then it should also be uncorrelated with $\{A_n^*\}$, which means that the relative orientation of $\{u_{N+1,n}\}$ and $\{A_n^*\}$ is random and thus the left-hand-side of the first equation in system (3.6) can be estimated as $A_0 u_0 \sqrt{N}$, where $A_0 \sim 1/\sqrt{N}$ and $u_0 \sim 1/\sqrt{2N}$ are the RMS values of A_n and u_{mn} respectively. Such an estimate indeed gives $|\delta| \sim 1/\sqrt{N}$. The same kind of estimate can also be used for each line of the system (3.7), which would give $|C_n| \sim 1/\sqrt{N}$.

If the above assumptions were fully correct, they would imply that, once the RMS values of $|C_n|$ and $|\delta|$ averaged over different not-too-small τ were exactly equal to each other. However, our numerical tests show that, even though both C_n and δ are indeed of the order $1/\sqrt{N}$, there is a systematic difference between them, which is, presumably, related to subtle correlations between u_{mn}, for which we have no explanation.

Considering the limitations of the above ACR scheme, one may be concerned with the very unlikely possibility that the matrix of the coefficients u_{mn} in the system of equations (3.6) has zero determinant and, therefore, the system has no solution for $\delta \neq 0$. In such a case, however, one can find the solution for $\delta = 0$, which, according to Eq.(3.8), means a complete recovery for $\langle S_1^z(\tau) \rangle$ instead of an "almost complete" one.

The real limitation of the scheme is rather associated with the possibility that the solution of (3.6) exists but implies that $\delta \sim 1$, and, as a result, the recovery falls short of being “almost complete". The character of our argument crucially relies on the assumption that the operator u is similar to a random rotation, which suggests that our ACR scheme would perform better for non-integrable quantum systems in comparison with the integrable ones.

Assuming that the system is non-integrable, one can further ask how large the recovery time τ should be for one to be able to speak of an "almost complete" recovery. Theoretically, the ACR should already be observable when the unitary transformation mixes large sectors of the Hilbert space but not all of it, which should happen after a few characteristic one-spin times. Our numerical results presented below are consistent with such an expectation.

In addition, let us introduce Matrix Participation Ratio (MPR):

$$\mathrm{MPR} = \frac{1}{2\sum\limits_{ij} |u_{ij}|^4}. \tag{3.9}$$

This quantity allows us to numerically characterize the evolution operator’s proximity u to the random rotation in Hilbert space. If given unitary u the value of MPR $\to 1$, it is close to the random rotation. In Fig. 3-3 (b) we plot MPR for the Hamiltonian (3.14) for different system sizes. This figure confirms the above assumption about the evolution operator.

The interesting direction is to study ACR for more experimentally relevant unitaries. It is particularly interesting to look at unitaries that can be implemented on existing quantum computers.

3.1.3 *Case of large $|\delta|$

In the above section, we argued that the parameter $|\delta|$ should be small for a regular ”physical” Hamiltonian. It is also interesting to look at the structure when the $|\delta|$ is always big. Consider the random initial state:

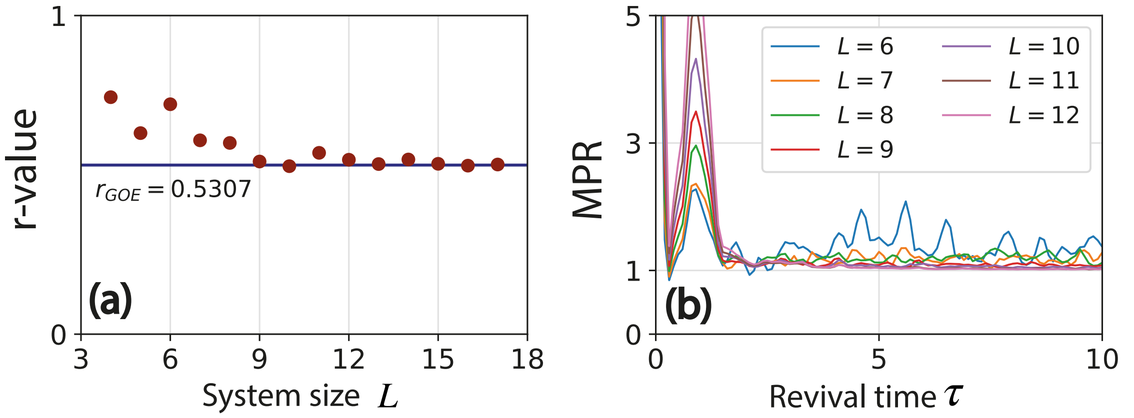

Figure 3-3: (a) r-value for the Hamiltonian (3.14) for different system sizes. Zero-momentum sector of the Hilbert space is considered. (b) Value of MPR (3.9) for evolution operator $u \equiv e^{-iH\tau}$, for different system sizes.

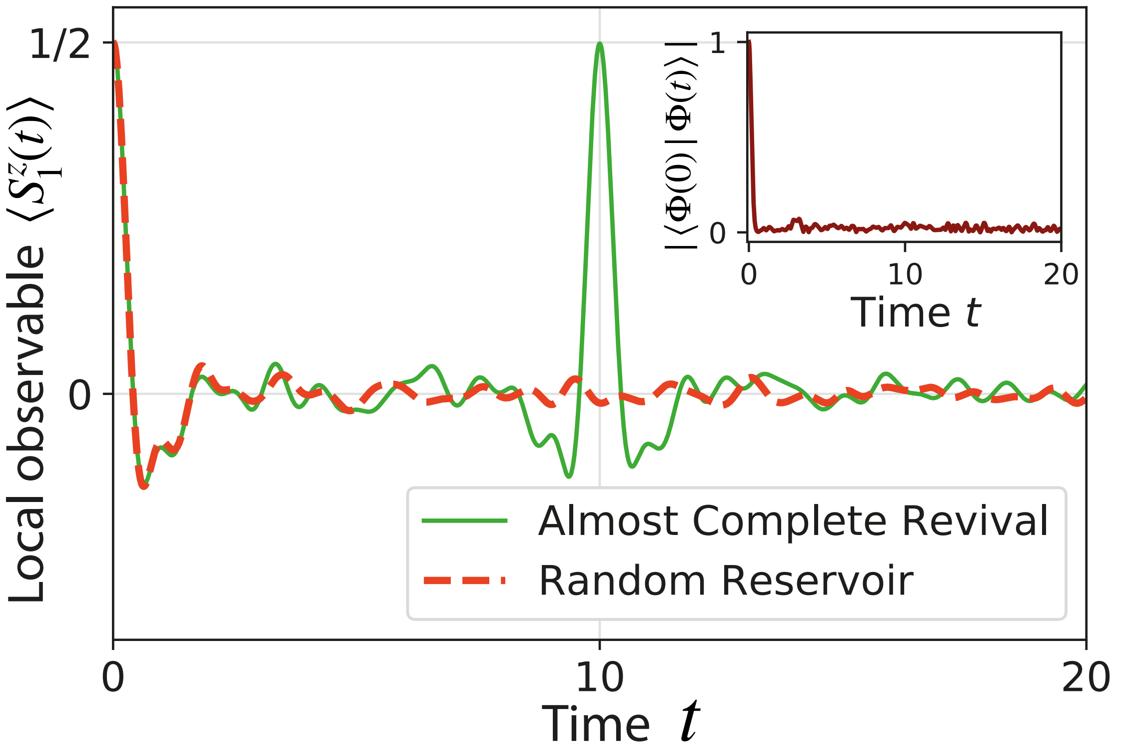

Figure 3-4: Time evolution of the local observable $\langle S_1^z \rangle$, for a system of $L = 12$ spins 1/2 governed by the Hamiltonian (3.14). The solid green line corresponds to the ACR state devised to obtain the revival at time $\tau = 10$; the dashed orange line corresponds to the random reservoir (see the text). The inset shows the fidelity of the ACR state $|\langle \Phi_{\text{ACR}}(0) | \Phi_{\text{ACR}}(t) \rangle|$.

$$|\Phi_{\mathrm{rnd}}\rangle = |\uparrow\rangle \otimes \sum_{n=1}^{2^{L-1}} A_n |\varphi_n\rangle, \tag{3.10}$$

where $|\varphi_n\rangle$ are elements of the many-body basis $\mathcal{B}_r = \{|\varphi_n\rangle\}_{n=1}^{2^{L-1}}$ on the sublattice of length $L-1$. Notice that coefficients A_n are random complex numbers, so no revival is implied. At the time τ:

$$e^{-iH\tau}|\Phi_{\mathrm{rnd}}\rangle \; = \; |\uparrow\rangle \otimes \sum_{n=1}^{2^{L-1}} C_n |\varphi_n\rangle \; + \; |\downarrow\rangle \otimes \sum_{n=2^{L-1}+1}^{2^L} C_n |\varphi_n\rangle. \tag{3.11}$$

Let us now choose the new basis $\bar{\mathcal{B}}_r = \{\phi_n\}_{n=1}^{2^{L-1}}$ for the sublattice as following. Let us consider the vector:

$$|\bar{\phi}_1\rangle = \sum_{n=2^{L-1}+1}^{2^L} C_n |\varphi_n\rangle. \tag{3.12}$$

The first vector $|\phi_1\rangle$ of the $\bar{\mathcal{B}}_r$ is constructed as $|\phi_1\rangle = |\bar{\phi}_1\rangle / \sqrt{\langle\bar{\phi}_1|\bar{\phi}_1\rangle}$. The rest of $2^{L-1}-1$ vectors are constructed by applying the Gram-Schmidt procedure. Now we can rewrite (3.11) as:

$$e^{-iH\tau}|\Phi_{\mathrm{rnd}}\rangle \; = \; |\uparrow\rangle \otimes \sum_{n=1}^{2^{L-1}} C_n |\varphi_n\rangle \; + \; \delta |\downarrow\rangle \otimes |\phi_1\rangle, \tag{3.13}$$

where $\delta = \sqrt{\langle\bar{\phi}_1|\bar{\phi}_1\rangle}$. Since A_n are chosen randomly scalar product $\sqrt{\langle\bar{\phi}_1|\bar{\phi}_1\rangle}$ should be the order of $1/\sqrt{2}$.

This exercise shows that by changing the basis appropriately, we can always have any wavefunction in the form (3.13) at the moment τ.

3.1.4 Example of ACR

Let us now construct ACR for a translationally invariant periodic chain of L spins 1/2 described by the Hamiltonian:

$$\begin{aligned} H =& \sum_{j=1}^{L} \left(J_x\, S_j^x S_{j+1}^x + J_y\, S_j^y S_{j+1}^y \right) \\ &+ \sum_{j=1}^{L} \left(h_x\, S_j^x + h_y\, S_j^y \right), \end{aligned} \tag{3.14}$$

where $(J_x, J_y, h_x, h_y) = (-2.0, -4.0, 2.2, 2.2)$ are dimensionless interaction constants, we imply that $\hbar = 1$. The above values are chosen such that the Hamiltonian (3.14) is far from integrability, as evidenced by the energy level-spacing statistics [50, 70].

An example of the ACR behavior for the observable S_1^z in a 12-spin chain is presented in Fig. 3-4. The initial state, in this case, was obtained by solving the system of equations (3.6) for the revival time $\tau = 10$, and, indeed, the expected revival at $t = \tau$ was observed.

In the same figure, we compare the ACR behavior with the one of a fully polarized spin in a "random reservoir" associated with the initial state $|\Phi_{\text{in}}\rangle = |1_1\rangle \otimes |\Psi_{\text{inf}}\rangle$, where $|\Psi_{\text{inf}}\rangle$ is sampled from the infinite temperature ensemble for the remaining $L-1$ spins [67, 71]. For the complex amplitudes in Eq.(3.4) $A_n = |A_n| e^{i\phi_n}$, the infinite temperature ensemble in the limit $N \gg 1$ implies that phases ϕ_n are randomly sampled from interval $[0, 2\pi)$ and the squares of the absolute values are sampled according to the probability distribution $P(|A_n|^2) = N e^{-N|A_n|^2}$ followed by the overall normalization. As seen in Fig. 3-4, the value of $\langle S_1^z(t) \rangle$ in the case of a random reservoir quickly relaxes to zero as expected for the infinite temperature equilibrium. We note that the $\langle S_1^z(t) \rangle$ for the ACR state and the random reservoir state nearly coincide over an extended initial time interval, yet the former evolves to exhibit a revival at time $t = \tau$, while the latter shows just featureless equilibrium fluctuations. Another remarkable observation is that the almost complete revival around $t = \tau$ has the character of a nearly complete time reversal, even though the time reversal as such was not explicitly targeted by the procedure based on system

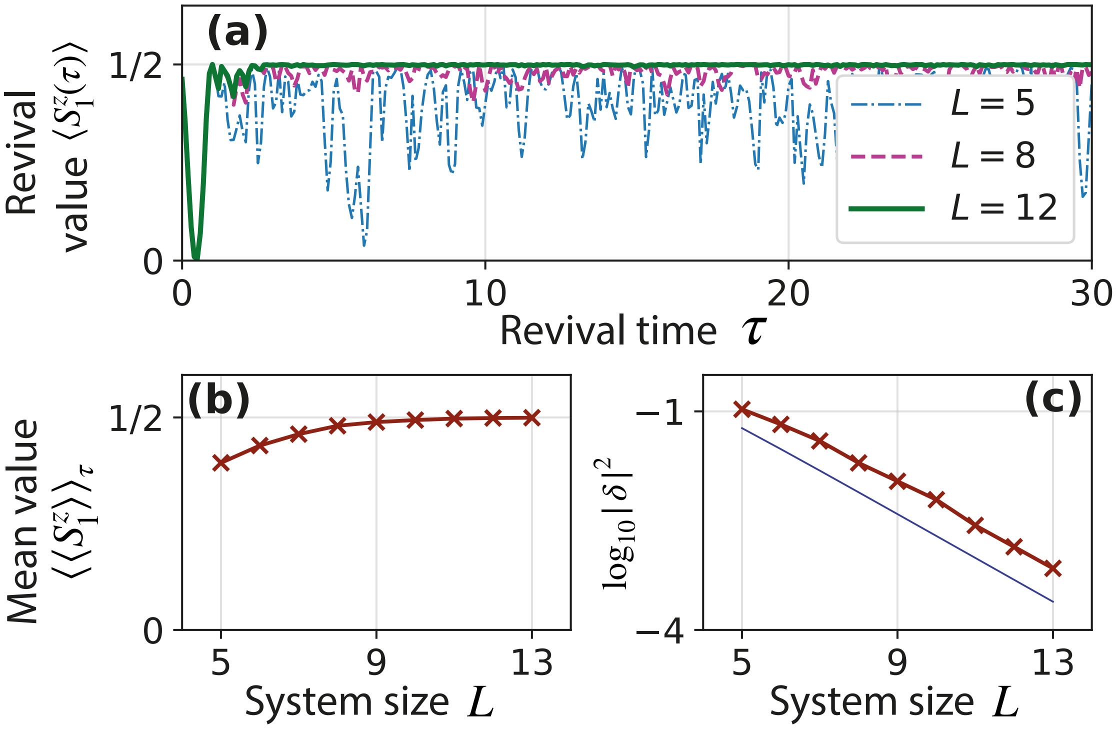

Figure 3-5: (a) Dependence of revival value $\langle S_1^z(\tau)\rangle$ on the revival time τ for the Hamiltonian (3.14). (b) Finite-size scaling of the τ-averaged revival value $\langle\langle S_1^z(\tau)\rangle\rangle_\tau$ given by equation (3.15). (c) Finite-size scaling of $|\delta|^2$. Crosses represent the numerical simulations, the solid blue line is the scaling $|\delta| = 1/\sqrt{N}$. Averaging is performed for an interval of $\tau \in [5, 30]$ with the step $\Delta t = 0.01$, for $L = 13$ with $\Delta t = 1.0$.

(3.6). We note in this regard that, as shown in the inset of Fig. 3-4, the fidelity of the many-body wave function $|\langle\Phi_{\rm ACR}(0)|\Phi_{\rm ACR}(t)\rangle|$ does not exhibit a revival at $t = \tau$. However, the observed time-reversed behavior of $\langle S_1^z(t)\rangle$ during ACR is consistent with the statistical argument of Ref.[72] that the most likely behavior of strong fluctuations is that of a time-reversed relaxation. Especially remarkable is the fact that such a symmetry appears on the fastest natural timescale of the system.

The dependence of the revived value of $\langle S_1^z\rangle$ on the revival time τ and on the size of the lattice is illustrated in Fig. 3-5(a): different points of the plot $\langle S_1^z(\tau)\rangle$ are obtained from different initial states $|\Phi_{\rm ACR}(0)\rangle$ computed for the fixed time τ with the help of Eqs.(3.6). There, one can observe that, for smaller systems, the revived values of $\langle S_1^z\rangle$ exhibit stronger fluctuations as a function of τ. However, the amplitude of these fluctuations rapidly decreases with the system size L. To quantify this decrease, we further observe that the fluctuation amplitudes for all system sizes L are already stationary for $\tau > 5$, which allows us to characterize the typical fluctuations of $\langle S_1^z(\tau)\rangle$ by a τ-averaged quantity $1/2 - \langle\langle S_1^z\rangle\rangle_\tau$, where

$$\langle\langle S_1^z\rangle\rangle_\tau = \frac{1}{\tau_1 - \tau_0}\int\limits_{\tau_0}^{\tau_1} \langle S_1^z(\tau)\rangle d\tau \tag{3.15}$$

with $\tau_0 = 5$ and $\tau_1 = 30$. The dependence of $\langle\langle S_1^z\rangle\rangle_\tau$ on the system size is plotted in Fig. 3-5(b). Finally, in Fig. 3-5(c), we present the semi-logarithmic plot of the τ-averaged value $\langle|\delta|^2\rangle_\tau = 1/2 - \langle\langle S_1^z\rangle\rangle_\tau$ as a function of L. This is an important plot because it shows that, for sufficiently large revival times τ, the typical value of δ decreases exponentially with the system size.

3.2 General revival scheme in chains of spin 1/2

In this section, we generalize the prescription offered in [1] such that the initial and revived values of selected local spin are both arbitrary points on a Bloch Sphere. Furthermore, we show that the revival may occur on a site different from the initial one.

Let us consider a lattice of L interacting spins 1/2. Each spin is described by the operator $\{S_i^\alpha\}$ where i is the lattice index and $\alpha = x, y, z$ is the spin projection index. As a collapsing observable, we pick the spin $\vec{S}_q$ and $\vec{S}'_p$ as a reviving one. Notice that while values of q and p as well as $\vec{S}_q$ and $\vec{S}'_p$ are different in general, there are no restrictions for them to coincide.

One-spin Hilbert spaces are defined as $|1_i\rangle$ and $|0_i\rangle$, such that $\langle 1_i|S_i^z|1_i\rangle = 1/2$ and $\langle 0_i|S_i^z|0_i\rangle = -1/2$. Let us introduce the basis $\mathcal{B} = \{|\varphi_j\rangle\}_{j=1}^{2^L}$, here $|\varphi_j\rangle$ is a many-body basis vector. Let us use the following ordering for the basis $\mathcal{B}$:

$$\mathcal{B} = \{|1_1\ 1_2 \ldots 1_L\rangle, |1_1\ 1_2 \ldots 0_L\rangle,\ \ldots\ , |0_1\ 0_2 \ldots 1_L\rangle, |0_1\ 0_2 \ldots 0_L\rangle\}. \tag{3.16}$$

Choice of basis determines further construction of ACR states. In our case, it is convenient to quantize the basis along z-axis and order it such as each many-body vector $|\varphi_j\rangle$ corresponds to the base-2 form of an integer j.

Let us use the following parametrization of the ACR state:

$$|\Phi_{\mathrm{ACR}}(0)\rangle = \sum_{k=1}^{2^{q-1}} \sum_{n=1}^{2^{L-q}} \left(A_{s(k,n)} |\varphi_{s(k,n)}\rangle + \alpha A_{s(k,n)} |\varphi_{s(k,n)+2^{L-q}}\rangle \right), \tag{3.17}$$

here q is the collapsing site, α - complex parameter defining the state of the collapsing site on a Bloch Sphere, and function $s(k,n)$ is defined as:

$$s(k,n) = 2^{L-q+1}(k-1) + n. \tag{3.18}$$

The ansatz (3.17) for the initial wavefunction guarantees that it has a form of tensor product $|\Phi_{\mathrm{ACR}}(0)\rangle = |l_q\rangle \otimes |\Psi_{\mathrm{res}}\rangle$, where $|l_q\rangle$ is the wavefunction of the q-th site which has the form:

$$|l_q\rangle = \frac{|0_q\rangle + \alpha|1_q\rangle}{\sqrt{1+|\alpha|^2}}, \tag{3.19}$$

$|\Psi_{\mathrm{res}}\rangle$ describes the rest of the system, we refer to $|\Psi_{\mathrm{res}}\rangle$ as to a 'reservoir'. The parameter α is a complex number that determines the position of q-th spin on a Bloch sphere as below:

$$\langle S_q^x\rangle = \frac{\mathrm{Re}\alpha}{1+|\alpha|^2}, \qquad \langle S_q^y\rangle = \frac{\mathrm{Im}\alpha}{1+|\alpha|^2}, \qquad \langle S_q^z\rangle = -\frac{1}{2}\cdot\frac{1-|\alpha|^2}{1+|\alpha|^2}.$$

Let us take a closer look at the expression (3.17). In general, a wavefunction in a form of tensor product $|l_q\rangle \otimes |\Psi_{\mathrm{res}}\rangle$ has 2^{L-1} independent parameters $\mathcal{A} = \{\{A_{s(k,n)}\}_{n=1}^{2^{L-1}}\}_{k=1}^{2^{q-1}}$. Function (3.18) gives us pairs of basis vectors $|\varphi_{s(k,n)}\rangle$ and $|\varphi_{s(k,n)+2^{L-q}}\rangle$ such that these two vectors are identical for all but one q-th site. For example if we set $q = L$, then for $k = 1$ we will have $|\varphi_{s(1,1)}\rangle = |1_1\ 1_2 \ldots 1_L\rangle$ and $|\varphi_{s(1,1)+1}\rangle = |1_1\ 1_2 \ldots 0_L\rangle$, taking all the $k = \overline{1, 2^{q-1}}$ we will end up with 2^{L-1}

basis vectors which are different only for the L-th site. Now to have a q-th spin in a pure state (3.19) we need to demand that $A_{s(k,n)+2^{L-q}} = \alpha A_{s(k,n)}$. If this condition is satisfied, then initial wavefunction always has a form of tensor product $|\Phi_{\rm ACR}(0)\rangle = |l_q\rangle \otimes |\Psi_{\rm res}\rangle$ for any set of parameters $\mathcal{A}$. In Figure 3-2 (a) we schematically illustrate the ansatz (3.17).

The set of parameters $\mathcal{A}$ defines the state of the reservoir $|\Psi_{\rm res}\rangle$. If all the parameters are chosen randomly, then the q-th spin will quickly entangle with the reservoir and remain entangled virtually forever, the same applies to all other spins. Our goal is to choose such set $\mathcal{A}$ that at the specified "revival" time τ wavefunction would split into a tensor product again $|\Phi_{\rm ACR}(\tau)\rangle = |\bar{l}_p\rangle \otimes |\bar{\Psi}_{\rm res}\rangle$.

Let us demand:

$$|\Phi_{\rm ACR}(\tau)\rangle = e^{-iH\tau}|\Phi_{\rm ACR}(0)\rangle = \sum_{k=1}^{2^{p-1}} \sum_{n=1}^{2^{L-p}} \left(C_{\bar{s}(k,n)}|\varphi_{\bar{s}(k,n)}\rangle + \beta C_{\bar{s}(k,n)}|\varphi_{\bar{s}(k,n)+2^{L-p}}\rangle \right), \tag{3.20}$$

this wavefunction has a form similar to (3.17), with the difference that now it is p-th spin in the pure state. The state $|\bar{l}_p\rangle$ is parametrized by the complex number β similarly to (3.19):

$$|l_q\rangle = \frac{|0_q\rangle + \beta|1_q\rangle}{\sqrt{1+|\beta|^2}},$$

we also modified $s(k,n)$ to $\bar{s}(k,n) = 2^{L-p+1}(k-1)+n$, to have a revival on p-th site.

To find such set $\mathcal{A}$ that (3.20) is satisfied we need to know the full form of the evolution operator at the revival moment $u \equiv e^{-iH\tau}$. Let us take a look at the full form of the condition (3.20):

$$
\begin{aligned}
&u_{1,1}A_1 + \cdots + u_{1,2^L}A_{2^L} = C_1\\
&u_{2,1}A_2 + \cdots + u_{2,2^L}A_{2^L} = C_2\\
&\vdots\\
&u_{2^L,1}A_2 + \cdots + u_{2^L,2^L}A_{2^L} = C_{2^L}.
\end{aligned}
\tag{3.21}
$$

By substituting $A_{s(k,n)+2^{L-q}} = \alpha A_{s(k,n)}$ into (3.21), for $n = \overline{1, 2^{L-q}}$ and $k = \overline{1, 2^{q-1}}$, we eliminate 2^{L-1} variables from the system (3.21). We can also eliminate 2^{L-1} equations from (3.21) by using the fact that $C_{\bar{s}(k,n)+2^{L-p}} = \alpha C_{\bar{s}(k,n)}$. Thus we obtain a set of conditions:

$$
\hat{V}\mathcal{A} = 0,
\tag{3.22}
$$

where the matrix $\hat{V}$ is given by:

$$
V_{ki} = u_{d[k],\bar{d}[i]} - \beta^{-1}u_{d[k]+2^{L-p},\bar{d}[i]} + \alpha u_{d[k],\bar{d}[i]+2^{L-q}} - \alpha\beta^{-1}u_{d[k]+2^{L-p},\bar{d}[k]+2^{L-q}},
\tag{3.23}
$$

where indexes $k, j = \overline{1, 2^{L-1}}$, and sets of indexes d and $\bar{d}$ are ordered sets:

$$
\begin{aligned}
d &= \{\{s(k,n)\}_{k=1}^{2^{q-1}}\}_{n=1}^{2^{L-q}},\\
\bar{d} &= \{\{\bar{s}(k,n)\}_{k=1}^{2^{p-1}}\}_{n=1}^{2^{L-p}}.
\end{aligned}
\tag{3.24}
$$

If matrix (3.23) is degenerate, then (3.22) has a solution and therefore (3.20) is satisfied exactly. However we argued in [1] that in case of interacting non-integrable Hamiltonian (3.23) must always be non-degenerate. In this case, the only solution of $\mathcal{A} = 0$, which is irrelevant. Let us allow one equation from (3.22) have non-zero right-hand side

$$\hat{V}\mathcal{A} = (\delta, 0, \ldots, 0)^T, \tag{3.25}$$

here δ is a parameter which will be determined from normalization condition on (3.19).

Let us assume that typical matrix element of v have absolute value $|v_{ki}| \sim 1/\sqrt{2^L}$ and a largely random phase. In this case we can estimate typical values of $\mathcal{A}$ and $\mathcal{C}$ as$|A_0| \sim 1/\sqrt{2^{L-1}}$ and $|C_0| \sim 1/\sqrt{2^{L-1}}$. Now if we substitute these typical values into the left-hand side of the first equation in (3.25) we obtain $\delta \sim 1/\sqrt{2^{L-1}}$. This is a key assumption for the existence of ACR, we will discuss it further in the chapter.

Let us formulate the procedure of ACR construction as step by step algorithm. In order to construct ACR one needs to:

1. Pick a collapsing q and reviving p sites.
2. Choose a position of collapsing $\vec{S}_q$ and reviving $\vec{S}'_p$ spins on a Bloch Sphere. Determine corresponding parameters α and β.
3. Compute sets of indexes d and $\bar{d}$ (3.24).
4. Compute matrix (3.23).
5. Solve set of equations (3.25). In practice one can set $\delta = 1$ to obtain a non-normalized solution.
6. When set of parameters $\mathcal{A}$ is determined, construct wavefunction (3.17) and normalize it.

In Figure 3-2 (b) we illustrate a particular example of obtaining conditions (3.25). In this example we imply that $p = q$ and that $\vec{S}_p = \vec{S}'_q = (0, 0, 1/2)$, which corresponds to $\alpha, \beta \to \infty$ or simply $|l_q\rangle = |1_q\rangle$. In this case matrix (3.23) is simply bottom-left block of size 2^{L-1} and wavefunctions (3.17) and (3.20) are easy to construct. This example corresponds to the one considered in [1].

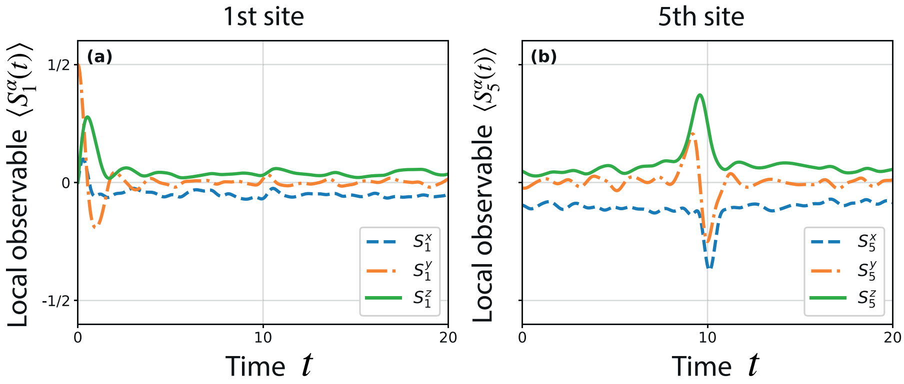

Figure 3-6: Time evolution of local observables S_m^α for the Hamiltonian (3.26). The dynamics on the 1st site $m = 1$ is shown in (a) and of the 5th $m = 5$ in (b). Revival time $\tau = 10.0$, system size $L = 12$, $\alpha = i$, $\beta = -\sqrt{2/9} - 1/3i$.

3.2.1 Example of generalized ACR

Let us now construct ACR for the Hamiltonian:

$$H_1 = \sum_{j=1}^{L} \left(g\sigma_j^x + h\sigma_j^z + J\sigma_j^z\sigma_{j+1}^z \right), \tag{3.26}$$

here parameters $(g, h, J) = (0.9045, 0.8090, 1)$ are used. Periodic boundary conditions $\sigma_i^\alpha = \sigma_{i+L}^\alpha$ are imposed. For the system sizes where exact diagonalization is available, it was tested thoroughly in [40, 73] that this Hamiltonian is in great agreement with Eigenstate Thermalization Hypothesis (ETH) [34, 35].

Consider the initial state $|\Phi_{\rm ACR}(0)\rangle = |l_1\rangle \otimes |\Psi_{\rm res}\rangle$, here $\alpha = i$ therefore $\vec{S}_1 = (0, 1/2, 0)$. Let us set the revival time as $\tau = 10$, and pick $p = 5$ and $\beta = -\sqrt{2/9} - 1/3i$. By solving the system of equations (3.25) for the system of $L = 12$ spins we find such $|\Phi_{\rm ACR}(0)\rangle$ that $\vec{S}_5 = (-0.353611, -0.249662, 0.249849)$, see Fig. 3-6. The norm of $|\vec{S}_5|^2 = 0.499797$ is close to 1/2, therefore the 5-th spin is almost at the pure state at the revival moment. We showed in [1] that the discrepancy between perfect revival and ACR vanishes exponentially with the system size.

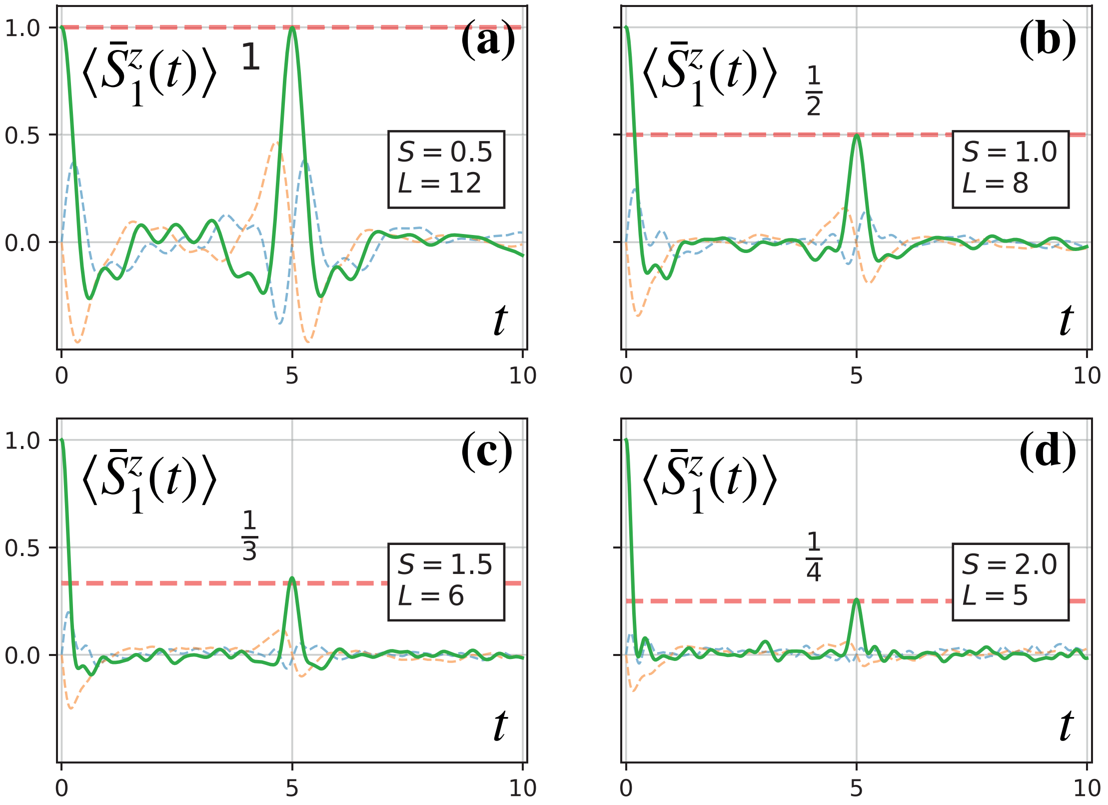

Figure 3-7: Time evolution of the local observables $\langle \bar{S}_1^\alpha \rangle = \langle S_1^\alpha \rangle / S$, for the Hamiltonian (3.27) for different quantum spins $S = \frac{1}{2}, 1, \frac{3}{2}, 2$. The green line corresponds to the z projection, dotted blue and orange lines to x and y correspondingly. Revival time $\tau = 5$.

3.2.2 Higher spins

In this section, we apply the mechanism of ACR construction for the case of quantum spins S higher than $\frac{1}{2}$. Let us consider the case when collapsing and reviving sites coincide $q = p = 1$ and when $|l_1\rangle = |1_1\rangle$. Let us consider the Hamiltonian:

$$H_2 = \sum_{j=1}^{L} \left(J_x \, S_j^x S_{j+1}^x + J_y \, S_j^y S_{j+1}^y \right) + \sum_{j=1}^{L} \left(h_x \, S_j^x + h_y \, S_j^y \right), \tag{3.27}$$

Periodic boundary conditions are imposed and parameters $(J_x, J_y, h_x, h_y) = (-2.0, -4.0, 2.2, 2.2)$ are used. Since this Hamiltonian acts in XY plane, then the equilibrium values of $\langle S_j^z \rangle = 0$. The Hamiltonian (3.27) is far from integrability, as evidenced by energy-level-spacing statistics [50].

For spins S it is convenient to order the basis $\mathcal{B}_S = \{|\varphi_j^S\rangle\}_{j=1}^{g^L}$ as $\mathcal{B}_S = \{g_g^L, ..., 2_g, 1_g, 0_g\}$ here $g = 2S + 1$ and j_g is a base-g form of an integer j. The initial state $|\Phi_{\text{ACR}}(0)\rangle$ has the form:

$$|\Phi_{\text{ACR}}(0)\rangle = \sum_{n=1}^{g^{L-1}} A_n |\varphi_n^S\rangle. \tag{3.28}$$

conditions for observation ACR in the basis $\mathcal{B}_S$ changes to:

$$\begin{aligned}
&\sum_{n=1}^{g^{L-1}} u_{g^{L-1}(g-1)+1,n} A_n = \delta \\
&\sum_{n=1}^{g^{L-1}} u_{g^{L-1}(g-1)+2,n} A_n = 0 \\
&\cdots \\
&\sum_{n=1}^{g^{L-1}} u_{g^L,n} A_n = 0.
\end{aligned} \tag{3.29}$$

The system (3.29) has g^{L-1} variables and equations, $\delta \neq 0$ to be determined from normalization conditions. The dimensionality of the Hilbert space is $\mathcal{D} = g^L$, the system (3.28) allows us to set to zero at the moment τ only $g^{L-1} - 1$ of the coefficients. There are also $p = g^{L-1}(g-1) + 1$ of non-zero coefficients left in $e^{-iHt}|\Phi_{\text{ACR}}(0)\rangle$, so $\langle S_1^z(\tau)\rangle$ can not exhibit almost complete revival for spins higher than $S > \frac{1}{2}$. With increasing system size its revival value converges to:

$$\langle S_1^z(\tau)\rangle \simeq \frac{1}{2S}.$$

In a Fig. 3-7 we plot the time evolution of $\langle \bar{S}_1^\alpha \rangle = \langle S_1^\alpha \rangle / S$ for different values of spin S. The $\langle \bar{S}_1^z(\tau) \rangle$ decreases with S which is in agreement with the classical picture in which one can not predict trajectory for arbitrary time if the system is chaotic.

3.3 Possible applications

3.3.1 Benchmarking quantum simulators

One possible application of ACR is to benchmark the performance of engineered many-qubit systems, such as quantum computers or quantum simulators. The observation of ACR amounts to a comprehensive test of quantum coherence and quantum control of the system. The larger the revival time τ, the more stringent the test and the greater the coverage of the many-qubit Hilbert space probed by the wave function in the course of the dynamical evolution. In particular, for non-integrable systems, one can hope that the time evolution of the many-qubit wavefunction before ACR would amount to a reasonably fair sampling of the system's Hilbert space. We further note that the observation of ACR of only one qubit for sufficiently large τ indicates that the overlap between the desired initial many-qubit state and the experimentally prepared one is close to 1.

Let us remark that for sufficiently long time delays τ, the ACR state is strongly entangled, which makes it difficult to prepare. Yet such difficulty is obviously much less than that of performing the full process tomography for a quantum simulator[74]. We further note that implementing ACR with relatively short τ should be less challenging, which turns τ into a parameter controlling the robustness of the ACR-based benchmarking.

Finally, the ability to prepare the ACR state requires one's ability to compute it on classical computers. This leaves ACR-based benchmarking as a tool for testing relatively small near-term quantum simulators or smaller parts of larger simulators when the qubits belonging to these parts can be physically decoupled from the rest.

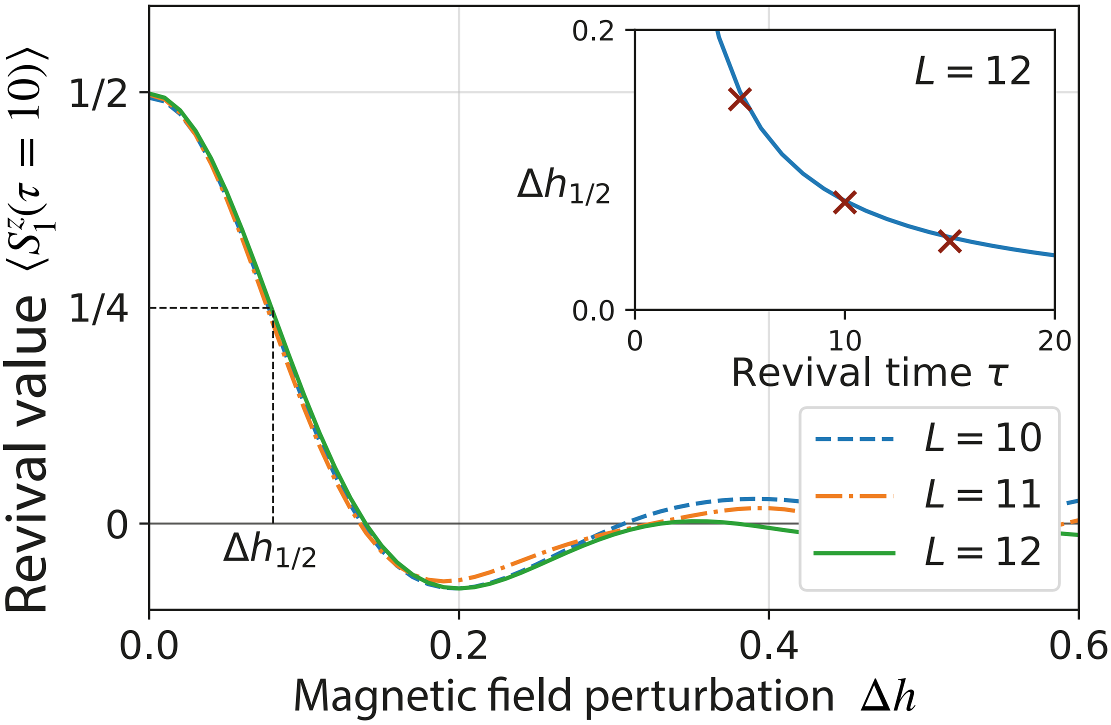

Figure 3-8: Dependence of revival value $\langle S_1^z(\tau = 10)\rangle$ on the magnetic field perturbation Δh. Revival time is fixed at $\tau = 10$, perturbation is introduced as $(h_x, h_y) = (2.2 - \Delta h, 2.2 - \Delta h)$. The inset shows the dependence of resolution $\Delta h_{1/2}$ on the revival time τ. Solid line corresponds to the fit $\Delta h_{1/2} = c_0/\tau$, where $c_0 = 0.3895$.

3.3.2 ACR as a part of sensor design

ACR is rather fragile to the changes in the Hamiltonian parameters. This fragility can be exploited to devise a sensor monitoring those parameters. To be specific, let us describe how the ACR states computed earlier for the Hamiltonian (2.1) can be used to monitor the values of the field parameters (h_x, h_y). We take the initial wave functions obtained to generate ACRs at $\tau = 10$ for spin chains of different lengths and then compute what happens if the field parameters $(h_x, h_y) = (2.2, 2.2)$ are modified to $(h_x, h_y) = (2.2 - \Delta h, 2.2 - \Delta h)$. Fig. 3-8 shows that, as expected, the revived value of $\langle S_1^z \rangle$ quickly decreases with increasing Δh. A sensor can thus use the departure of this revived value from the maximum one to monitor Δh. We define the selectivity range of such a sensor, $\Delta h_{1/2}$, as the value of Δh corresponding to the decrease of $\langle S_1^z(\tau) \rangle$ by 50 percent. As illustrated in Fig. 3-8, $\Delta h_{1/2}$ depends very little on the number of spins L in the system; however, it decreases inversely proportionally to the revival time τ (see the inset). This means that the selectivity of such a sensor can be increased by increasing the value of τ, thereby making the sensor very selective. The resolution within the selectivity range can be increased by repeated measurements followed by the fitting to the curve in Fig. 3-8.

The performance of the above ACR sensor based on an L-spin cluster can be compared with that of L noninteracting spins. The latter can also be very accurate, especially in the entangled state [75]. The principal advantage of the ACR sensor is not in the resolution but in the selectivity range. The "noninteracting" sensor produces a sinusoidal response as a function of the measured field and, therefore, requires an additional precalibration placing the sensor within the central fringe of the measured field. The ACR sensor does not have such an issue. Its non-zero signal would guarantee that the measured field has a value within the selectivity range.

3.3.3 Delayed disclosure of a secret

Imagine that one needs to share a piece of valuable information in the form of a string of K classical bits. However, the information must not be disclosed to anyone before a certain moment of time in the future. Below we propose a scheme that

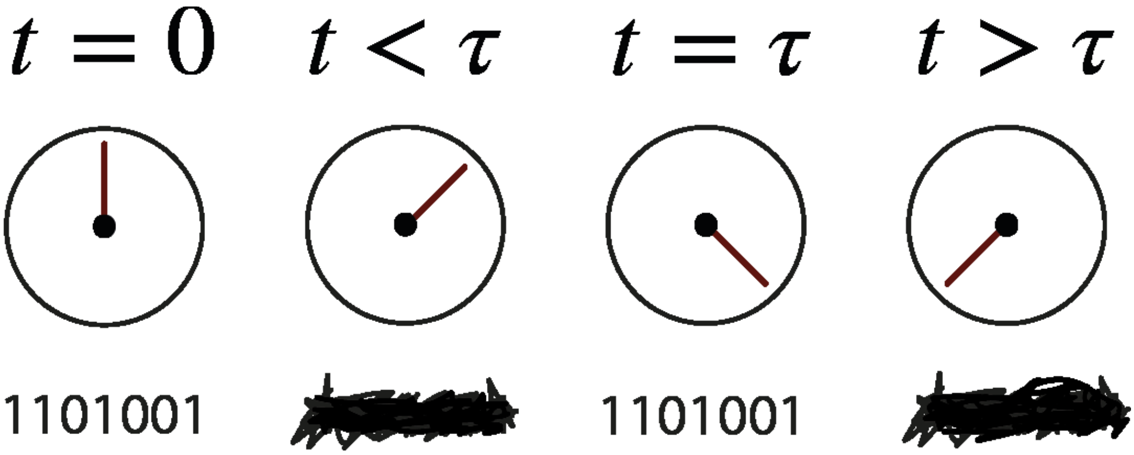

Figure 3-9: Schematic illustration of delayed disclosure of a secret. The information is available only at two moments of time $t = 0$ and $t = \tau$. Any attempt to extract the information before the τ leads to its destruction

allows one to implement such a delayed disclosure of a secret with the help of the ACR states.

Let us first consider only one classical bit. The state of this bit is to be encoded as $S_1^z = \pm 1/2$ for a given spin 1/2 (a qubit), interacting with a finite "reservoir" of 10-50 other spins 1/2. The state of the reservoir $|\Psi_{\text{res}}\rangle$ is to be prepared using the solutions of the system of equations (3.6) such that $\langle S_1^z(t)\rangle$ exhibits a revival at $t = \tau$ (see Fig. 3-10). After the quantum evolution is launched, there are two possible scenarios: Either one measures S_1^z at $t = \tau$ and thereby obtains the encoded bit value with probability close to one, or the measurement is performed at a wrong time (or someone has interfered with the evolution of the system) and, therefore, the measured value of S_1^z is, most likely, uncorrelated with the encoded one.

If one were to be transmitting only one bit of information, then one realization of the above procedure would not be sufficient: the occurrence of ACR on a single spin 1/2 would need to be verified either by repeating the procedure several times, or by running it simultaneously for several identical groups of spins 1/2. In this regard, the need to transmit a larger number of bits makes the verification of ACR more efficient: namely, one only needs to transmit two copies of the string of K bits. If K is sufficiently large and the two recovered strings are identical, then this indicates that the information was transmitted as intended.

Can the delayed disclosure of a secret be implemented classically? Although

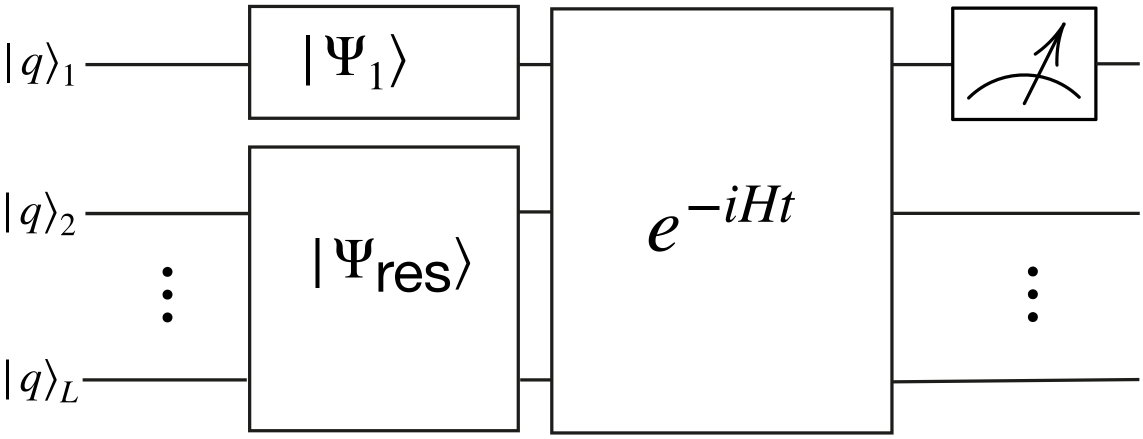

Figure 3-10: Scheme for implementing the delayed disclosure of a secret: a classical bit is encoded into a local observable $S_1^z = \pm 1/2$. The rest of the system (a reservoir) is prepared in a state $|\Psi_{\mathrm{res}}\rangle$ constructed to generate a revival at time τ. The bit is retrieved when the measurement time t is equal to τ. Measurements at times t outside of a narrow interval around τ would lead to random outcomes.

ACR can, in principle, be implemented classically, it cannot be used for a delayed disclosure of a secret, because the classical variables can be measured nondestructively, which means that the information is not protected by a physical principle. Let us further remark here that classical ACRs are much more difficult to realize than quantum ones, because the classical spin dynamics is, typically, chaotic[62] and hence exponentially sensitive to the uncertainties of initial conditions and Hamiltonian parameters, while non-integrable spin-1/2 systems, normally, do not have such a problem[76].

In conclusion, we have shown how to generate an almost complete recovery of a fully polarized state of a given spin 1/2 belonging to a larger lattice of interacting spins 1/2. We have discussed possible applications of ACR to the benchmarking of quantum simulators and also proposed to utilize ACR for a delayed disclosure of a secret.

Chapter 4

Manifestly non-classical eigenstates in a model of collisional decoherence

In this section, contrary to the previous two, we study not out-of-equilibrium initial states but special eigenstates in a model of collisional decoherence. We test the hypothesis that every eigenstate in a large system is locally classical-like. We find that it is true for most eigenstates, yet we find some eigenstates in the middle of the spectrum which violate the above hypothesis. The content of this chapter is mostly based on the paper [2].

4.1 Decoherence theory

Quantum many-body Hilbert space allows for all sorts of superpositions, for example, the famous Schrödinger's cat states. Such superpositions, however, are entirely absent on the macroscopic level. A thoughtful explanation of why this is happening is required to explain the so-called quantum-classical transition.

Decoherence theory [77–82] provides the following explanation. One cannot completely isolate any system from everything else. When the interaction between the system and the environment is taken into account, many-body superpositions become extremely fragile. In the above studies usually some out-of-equilibrium initial state of the form $|\Psi(0)\rangle = |\psi_S\rangle \otimes |\psi_B\rangle$ is considered, here $|\psi_S\rangle$ describes the state of the system $\mathcal{S}$ and $|\psi_B\rangle$ represents the environment $\mathcal{B}$.

We provide a complementary view by considering the eigenstates of the combined system $\mathcal{H} = \mathcal{S} \otimes \mathcal{B}$. The eigenstate decoherence hypothesis (EDH) introduced in [83], suggests that eigenstates of $\mathcal{H}$ should be locally classical. In this section, we test EDH for a model of collisional decoherence and discover that it holds for the majority of eigenstates. Yet we discover a small subset of eigenstates violating EDH.

4.2 Eigenstate Decoherence Hypothesis

The Eigenstate decoherence hypothesis may be formulated as follows. Consider the total Hamiltonian H which describes the system $\mathcal{H}$, for any eigenstate $|\Phi_E\rangle$, the corresponding reduced density matrix

$$\rho_E^S \equiv \mathrm{tr}_{\mathcal{B}} |\Phi_E\rangle\langle\Phi_E|, \tag{4.1}$$

is classical-like according to a suitable quantumness measure, or, in other words, free of any weird quantum Schrödinger-cat-type superpositions.

The EDH is motivated by the eigenstate thermalization hypothesis (ETH) [34–36]. According to the ETH if the system reaches thermal equilibrium, then any local observable $\langle \hat{O}_E^S \rangle$ of $\mathcal{S}$, as well as ρ_E^S are smooth functuons of E. Various case studies have suggested that it is indeed true for generic nonintegrable systems without disorder [36, 40, 42].

4.2.1 Specific test of EDH

So far, there are not many specific tests of the EDH except for a central spin model case [83]. Here we consider a more natural setup, namely a heavy particle (subsystem $\mathcal{S}$) in a gas of light particles $\mathcal{B}$. In particular, consider a heavy particle prepared in some superposition state, for example $|\Psi_S\rangle = 1/\sqrt{2}(|\psi(\vec{r}_1)\rangle + |\psi(\vec{r}_2)\rangle)$, where $|\vec{r}_2 - \vec{r}_2| \gg l_{\mathrm{mfp}}$, here l_{mfp} is a mean free path. In this case, one can reasonably expect that such a state has a lifetime of the order of mean free time. In other words, it should be a highly out-of-equilibrium state, and one cannot expect it to be stable. Our studies demonstrate that this is indeed true most of the time. Yet, surprisingly, we find that non-classical eigenstates exist where such a heavy particle is in a superposition of two distant wavefunctions forever.

4.3 Model of collisional decoherence

Let us consider a heavy particle in a gas of light particles. We employ exact diagonalization to find rare special eigenstates distinct from thermal ones. Exact diagonalization limits us to a one-dimensional version of this problem. Let us consider N fermions and a single heavy particle on a linear lattice consisting of L sites:

$$\begin{aligned} H = & \left(-J \sum_{i=1}^{L-1} c_i^\dagger c_{i+1} - J' \sum_{i=1}^{L-1} a_i^\dagger a_{i+1} + h.c. \right) \\ & + \sum_{i=1}^{L} U a_i^\dagger a_i c_i^\dagger c_i + \delta H. \end{aligned} \tag{4.2}$$

Here $c_i^\dagger$ creates a fermion, and $a_i^\dagger$ – the particle, $J > 0$ and $J' \geq 0$ are hopping constants for fermions and the particle, respectively, $U > 0$ is the coupling constant between a fermion and the particle. The term

$$\delta H = \epsilon \sum_{j=1}^{L} (j/L) c_j^\dagger c_j \tag{4.3}$$

describes the linear on-site potential felt by fermions. It is introduced to break the otherwise present reflection symmetry of the Hamiltonian for a purpose to be discussed later. When considering a relatively large system size, we will imply the thermodynamic limit with the fixed fermionic density $n \equiv N/L$.

In order to separate time scales of decoherence and thermalization, we assume that the distinguished particle is heavy as compared to the fermions [84, 85], which amounts to $J \gg J'$.

In the limiting case of the infinitely heavy particle, $J' = 0$, the model becomes trivially integrable with the eigenstates of the form

$$\Phi_E = |j\rangle \otimes |F_E^j\rangle, \tag{4.4}$$

where $|j\rangle$ is the state of the particle localized on the site j and $|F_E^j\rangle$ is an eigenstate of the j-dependent quadratic fermionic Hamiltonian

$$H_j = \left(-J \sum_{i=1}^{L-1} c_i^\dagger c_{i+1} + h.c. \right) + U c_j^\dagger c_j + \delta H. \tag{4.5}$$

Note that if $\delta H = 0$, the spectrum acquires degeneracies due to the reflection symmetry of the Hamiltonian.

4.3.1 Coherence length

Now we need to choose some physical quantity, to quantitatively characterize the quantumness of the heavy particle. For a set up described above the most natural quantity is the coherence length [86, 87]

$$l(\rho^S) \equiv \sqrt{\frac{2 \sum_{ij=1}^{L} |\langle i|\rho^S|j\rangle|^2 (i-j)^2}{\sum_{ij=1}^{L} |\langle i|\rho^S|j\rangle|^2}}, \tag{4.6}$$

Here $\rho^S = \mathrm{tr}_B |\Psi\rangle\langle\Psi|$ is a reduced density matrix of the particle obtained from a pure state $|\Psi\rangle$ of the closed particle-gas system and $\langle i|\rho^S|j\rangle = \langle\Psi|a_j^\dagger a_i|\Psi\rangle$ is its matrix elements in the position basis. The quantity (4.6) has a measure of length and depends on off-diagonal elements of the density matrix. It effectively measures the spatial extension of a superposition of localized states, ranging from 0 for a particle localized on a single site to $(L-1)$ for a highly non-classical state of the form

$$|\Psi_Q\rangle = (1/\sqrt{2})(a_1^\dagger + a_L^\dagger)|F\rangle, \tag{4.7}$$

where $|F\rangle$ is some state of N fermions. If the coherence length is equal to zero, all the off-diagonal elements of the density matrix ρ^S are equal to zero. Larger values of $|i-j|$ for non-zero off-diagonal elements imply longer coherence length.

To simplify the terminology and notations, we will attribute coherence length also to pure many-body states, implying $l(|\Psi\rangle) \equiv l\,(\mathrm{tr}_{\mathcal{B}}|\Psi\rangle\langle\Psi|)$.

Importantly, while l for non-classical states can be on the order of the size of the system L, as in eq. (4.7), for classical-like states l is independent on the system size. In particular, for the model (4.2) we expect that l for classical-like states is bounded from above by the average interparticle distance L/N times the probability for the scattering of a fermion off the particle.

4.3.2 Test of EDH

To test the EDH we numerically diagonalize the Hamiltonian (4.2) for finite system sizes and calculate the coherence length $l(|\Phi_E\rangle)$ for each eigenstate $|\Phi_E\rangle$. The range of system sizes is $L = 8, 9, \ldots 12$. We use half-filling to keep the fermion density N/L independent of the system size. Namely, we take $N = L/2$ for even L and $N = (L-1)/2$ for odd L. We consider both unbiased ($\varepsilon = 0$) and biased ($\varepsilon = 0.1$) versions of the Hamiltonian (4.2).

The coherence lengthes of all eigenstates are presented in Fig. 4-1. Most of the states have coherence length on the order of the average interparticle distance, $L/N \simeq 2$, in accordance with the expectation discussed above. In particular, the coherence length averaged over all states reads $l_{\mathrm{av}} = 2.63$. However, one can clearly see that there exists a number of "outlier" eigenstates with a large coherence length well exceeding this value. Such outliers are mostly concentrated at the edges of the spectrum, however, they also can be found in the middle of the spectrum.

As discussed above, a decisive signature of violation of the EDH is the growth of the coherence length with the system size. In Fig. 4-2 we show the finite-size scaling

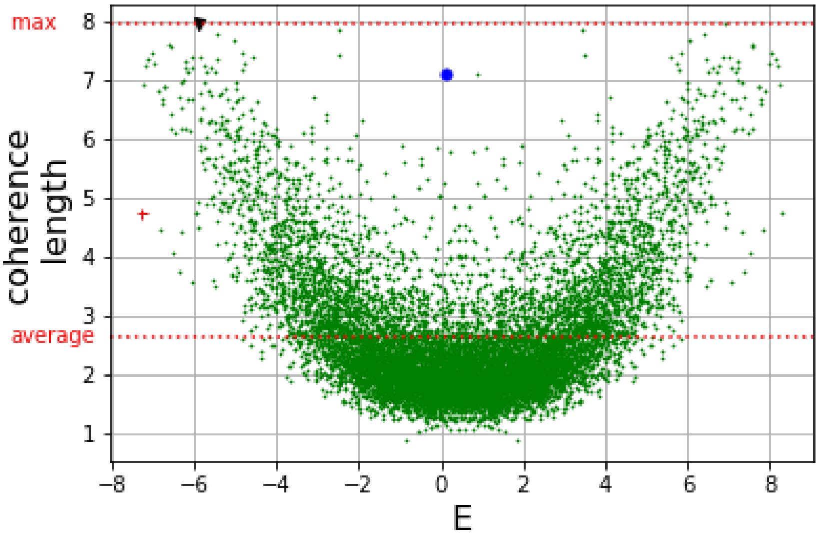

Figure 4-1: The coherence length for eigenstates of the nonintegrable Hamiltonian (4.2) with $J = 1$, $J' = 0.2$, $U = 1$, $N = 6$, $L = 12$, $\delta H = 0$. The ground state, the state with the maximal coherence length and a state in the middle of the spectrum with a large coherence length are marked with the red cross, black triangle and blue circle, respectively. Fig. from ref [2]

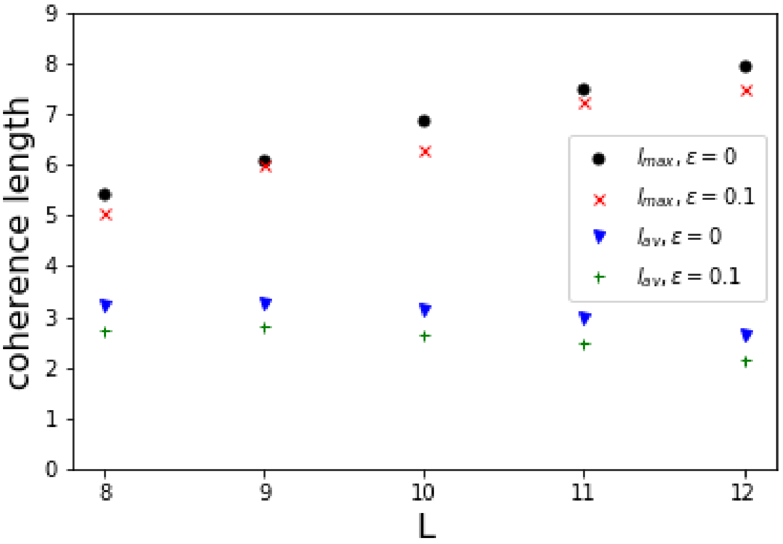

Figure 4-2: The maximal l_{max} and average l_{av} coherence lengths for eigenstates of the nonintegrable Hamiltonian for the cases of the presence ($\epsilon = 0$) and absence ($\epsilon = 0.1$) of the spatial reflection symmetry. The system is half-filled with fermions, with $N = L/2$ for even L and $N = (L-1)/2$ for odd L. Other parameters of the Hamiltonian are the same as in Fig. 4-1. Fig. from ref [2].

of the average and maximal (over all eigenstates) coherence lengths. The scaling of these two quantities is drastically different: while the former vanishes with the system size, the latter grows linearly with L. Thus we conclude that our numerical data support the weak EDH, but suggest the violation of the strong EDH.

We have performed numerical calculations with various fermion densities (where we can access slightly larger system sizes, up to $L = 13$), coupling strengths, as well as next-to-nearest neighbor interactions and obtained similar results. Note that, the potential bias δH does not quantitatively alter the result, as is clear from Fig. 4-2

4.3.3 EDH: Conclusions

In this section, we have tested the eigenstate decoherence hypothesis (EDH) for a system consisting of a heavy particle immersed in a one-dimensional Fermi gas. Our numerical data suggest that while the weak EDH holds, the strong EDH is violated by rare non-classical outlier eigenstates with a particle coherence length on the order of the system size.

The existence of such outlier eigenstates is in stark contrast with the intuition based on the theory of collisional decoherence [81, 85, 88], which predicts rapid decoherence as soon as the particle experience a collision with the gas particles. A plausible resolution of this conundrum is that most initial states (in particular, product states of a particle and a gas often considered in this theory) have a vanishing overlap with outliers, and thus the latter typically do not affect the decoherence. Careful crafting of the state of a many-body system (e.g. in a cold atom simulator [89]) is required to unveil the non-classical eigenstates.

Relation with quantum many-body scars

Finally, we remark that the outlier non-classical eigenstates violating the EDH resemble the many-body scars violating the ETH. One may wonder if the scars, in fact, exist in the model described by (4.2). At $J = J'$ and $\delta H = 0$ the Hamiltonian (4.2) is a Hubbard Hamiltonian, which is integrable in 1D and known to possess eigenstates violating ETH [90]. However, to the best of our knowledge, no scars have been reported away from this point. Furthermore, typically the scars are not robust with respect to perturbations of the Hamiltonian [91], while the violation of the EDH is. We, therefore, conclude that, anyway, the violation of EDH is not conditioned on the existence of quantum many-body scars.

Chapter 5

Conclusions and outlook

In the present thesis, we studies several classes of exceptional states in many-body systems. Chapters 2 and 3 focused on the special dynamics of certain strongly out-of-equilibrium states in spin systems. In Chapter 4, we studied unusually non-classical eigenstates in a model of collisional decoherence. We have presented corresponding conclusions at the end of each Chapter. Here we would like to share a broader and less specific look at the results of each Chapter and the future directions of research.

5.1 Periodic trajectories in many-spin systems

We have studied both classical and quantum evolution of initially fully polarized spin configurations. The classical dynamics of this configuration turned out to be surprisingly complex. Not only have we discovered irregular dependence of the stability of periodic trajectories on the system size, but we have also uncovered the existence of a intermediary quasiperiodic regime. Furthermore, we discovered that for certain system sizes when the periodic motion is always unstable, but the quasiperiodic regime exhibits good stability and is accompanied by translational symmetry breaking.

The quasiperiodic regime requires further research. We believe that study of periodic trajectories and quasiperiodic regime in different geometries can be a promising direction for future research.

While studying the quantum counterpart of the problem, we have discovered that for higher quantum spins, extra stable periodic trajectories manifest themselves as lower-entropy eigenstates in chains of small sizes. We refer to such eigenstates as "Finite size quantum scars" or FSQS. Although FSQS states so far has been observed for finite size systems it is an interesting question whether they survive thermodynamic limit.

Lastly, we have introduced the notion of "quantum separatrix" which distinguishes between oscillatory and non-oscillatory behavior. We demonstrated that analogously to the classical picture, states corresponding to periodic initial conditions are most unstable near separatrix. The parameters of the Hamiltonian corresponding to the quantum separatrix can be approximately predicted from classical ones. The existence of such a connection between quantum and classical problems might be useful in the understanding of quantum to classical transition.

5.2 Almost complete revivals

In Chapter 3, we have introduced a phenomenon of almost complete revivals. We provided a prescription on how to build an out-of-equilibrium state such that at a predetermined moment of time some selected local spin will undergo an almost complete revival to its full polarization. We also have generalized this method to the case when collapse and revival sites do not coincide.

We suggested several possible applications for this phenomenon. Namely, benchmarking of quantum simulators, entanglement-assisted sensing, and delayed disclosure of a secret. As we have demonstrated, such revivals can be obtained in systems of 5-25 spins. These suggestions rightly raise the question of the experimental possibility of constructing almost complete reviving states, for example, by using existing quantum computers. In further research we must answer the following crucial question: how can one practically implement almost complete revivals with existing quantum hardware?

5.3 Non-classical eigenstates in many-body systems

In Chapter 4, we shifted our attention from special out-of-equilibrium states to special eigenstates. We have considered a heavy particle in a gas of light fermions and found that such a system possesses eigenstates for which the heavy particle is in a non-classical spatial superposition at two separate locations. One could expect such states to be cannot be stationary, because collisions would lead to quick decoherence of such state. Nevertheless, our calculations show a small subset of perfectly stable eigenstates corresponding to the highly non-local state of the heavy particle. On the other hand, we have also established that the vast majority of eigenstates are locally classical-like, thereby confirming the validity of the weak version of Eigenstate Decoherence Hypothesis.

Although we did our best to eliminate all obvious integrals of motion in the system, such as translational or mirror symmetry, our simulations were still conducted in one dimension. Therefore we must ask ourselves whether the observed non-classical eigenstates will remain in higher dimensions. We have not yet answered this question due to the high computational complexity of two-dimensional problem. We believe that this is an important question for further research.

Another direction of further research is to find more models to test Eigenstate Decoherence Hypothesis. So far, it has been tested only in the central spin model and in the model of collisional decoherence. It would also be interesting to test this hypothesis in models describing light-matter interaction, such as the Jaynes-Cummings-Hubbard model, which describes an array of coupled optical resonators. Studying such models might be advantageous because, in this case, one can relatively easily pick an appropriate measure of classicality. Furthermore, optical models often have the advantage of being experimentally realizable.

Bibliography

[1] Igor Ermakov and Boris V Fine. Almost complete revivals in quantum many-body systems. *Physical Review A*, 104(5):L050202, 2021.

[2] Ivan V Dudinets, Igor Ermakov, and Oleg Lychkovskiy. Testing eigenstate decoherence hypothesis in a model of collisional decoherence. *EPL (Europhysics Letters)*, 134(6):60004, 2021.

[3] Igor Ermakov. Generalized almost complete revivals in quantum spin chains. *arXiv preprint arXiv:2205.05584*, 2022.

[4] Eric J Heller. Bound-state eigenfunctions of classically chaotic hamiltonian systems: scars of periodic orbits. *Physical Review Letters*, 53(16):1515, 1984.

[5] Harvey R Brown and Jos Uffink. The origins of time-asymmetry in thermodynamics: The minus first law. *Studies in History and Philosophy of Science Part B: Studies in History and Philosophy of Modern Physics*, 32(4):525–538, 2001.

[6] Toshiya Kinoshita, Trevor Wenger, and David S Weiss. A quantum newton's cradle. *Nature*, 440(7086):900–903, 2006.

[7] Enrico Fermi, P Pasta, Stanislaw Ulam, and Mary Tsingou. Studies of the nonlinear problems. Technical report, Los Alamos National Lab.(LANL), Los Alamos, NM (United States), 1955.

[8] Hannes Bernien, Sylvain Schwartz, Alexander Keesling, Harry Levine, Ahmed Omran, Hannes Pichler, Soonwon Choi, Alexander S Zibrov, Manuel Endres, Markus Greiner, et al. Probing many-body dynamics on a 51-atom quantum simulator. *Nature*, 551(7682):579–584, 2017.

[9] Louk Rademaker and Dmitry A Abanin. Slow nonthermalizing dynamics in a quantum spin glass. *Physical Review Letters*, 125(26):260405, 2020.

[10] Zhe-Xuan Gong and Lu-Ming Duan. Prethermalization and dynamic phase transition in an isolated trapped ion spin chain. *New Journal of Physics*, 15(11):113051, 2013.

[11] Brian Neyenhuis, Jiehang Zhang, Paul W Hess, Jacob Smith, Aaron C Lee, Phil Richerme, Zhe-Xuan Gong, Alexey V Gorshkov, and Christopher Monroe. Observation of prethermalization in long-range interacting spin chains. *Science advances*, 3(8):e1700672, 2017.

[12] Marcos Rigol. Breakdown of thermalization in finite one-dimensional systems. *Physical review letters*, 103(10):100403, 2009.

[13] Vladimir E Korepin, Nicholay M Bogoliubov, and Anatoli G Izergin. *Quantum inverse scattering method and correlation functions*, volume 3. Cambridge university press, 1997.

[14] PP Kulish and EK Sklyanin. Quantum inverse scattering method and the heisenberg ferromagnet. *Physics Letters A*, 70(5-6):461–463, 1979.

[15] GP Berman, F Borgonovi, FM Izrailev, and A Smerzi. Irregular dynamics in a one-dimensional Bose system. *Physical review letters*, 92(3):030404, 2004.

[16] A Minguzzi and DM Gangardt. Exact coherent states of a harmonically confined tonks-girardeau gas. *Physical review letters*, 94(24):240404, 2005.

[17] Stefan Palzer, Christoph Zipkes, Carlo Sias, and Michael Köhl. Quantum transport through a tonks-girardeau gas. *Physical review letters*, 103(15):150601, 2009.

[18] Oleksandr Gamayun, O Lychkovskiy, and V Cheianov. Kinetic theory for a mobile impurity in a degenerate tonks-girardeau gas. *Physical Review E*, 90(3):032132, 2014.

[19] Oleg Lychkovskiy. Perpetual motion and driven dynamics of a mobile impurity in a quantum fluid. *Physical Review A*, 91(4):040101, 2015.

[20] JJ Mendoza-Arenas, S Al-Assam, SR Clark, and D Jaksch. Heat transport in the xxz spin chain: from ballistic to diffusive regimes and dephasing enhancement. *Journal of Statistical Mechanics: Theory and Experiment*, 2013(07):P07007, 2013.

[21] Balázs Pozsgay. Failure of the generalized eigenstate thermalization hypothesis in integrable models with multiple particle species. *Journal of Statistical Mechanics: Theory and Experiment*, 2014(9):P09026, 2014.

[22] Marcos Rigol, Vanja Dunjko, Vladimir Yurovsky, and Maxim Olshanii. Relaxation in a completely integrable many-body quantum system: an ab initio study of the dynamics of the highly excited states of 1d lattice hard-core bosons. *Physical review letters*, 98(5):050405, 2007.

[23] Amy C Cassidy, Charles W Clark, and Marcos Rigol. Generalized thermalization in an integrable lattice system. *Physical review letters*, 106(14):140405, 2011.

[24] Tim Langen, Sebastian Erne, Remi Geiger, Bernhard Rauer, Thomas Schweigler, Maximilian Kuhnert, Wolfgang Rohringer, Igor E Mazets, Thomas Gasenzer, and Jörg Schmiedmayer. Experimental observation of a generalized gibbs ensemble. *Science*, 348(6231):207–211, 2015.

[25] Rahul Nandkishore and David A Huse. Many-body localization and thermalization in quantum statistical mechanics. *Annu. Rev. Condens. Matter Phys.*, 6(1):15–38, 2015.

[26] Kai Xu, Jin-Jun Chen, Yu Zeng, Yu-Ran Zhang, Chao Song, Wuxin Liu, Qiujiang Guo, Pengfei Zhang, Da Xu, Hui Deng, et al. Emulating many-body localization with a superconducting quantum processor. *Physical review letters*, 120(5):050507, 2018.

[27] Daniel L Stein and Charles M Newman. *Spin glasses and complexity*, volume 4. Princeton University Press, 2013.

[28] Pierre Gaspard. Chaos, scattering and statistical mechanics. *Chaos*, 2005.

[29] Allan J Lichtenberg and Michael A Lieberman. *Regular and chaotic dynamics*, volume 38. Springer Science & Business Media, 2013.

[30] Tómas A Brody, Jorge Flores, J Bruce French, PA Mello, A Pandey, and Samuel SM Wong. Random-matrix physics: spectrum and strength fluctuations. *Reviews of Modern Physics*, 53(3):385, 1981.

[31] Thomas Guhr, Axel Müller-Groeling, and Hans A Weidenmüller. Random-matrix theories in quantum physics: common concepts. *Physics Reports*, 299(4-6):189–425, 1998.

[32] Madan Lal Mehta. *Random matrices*. Elsevier, 2004.

[33] Mohit Pandey, Pieter W Claeys, David K Campbell, Anatoli Polkovnikov, and Dries Sels. Adiabatic eigenstate deformations as a sensitive probe for quantum chaos. *Physical Review X*, 10(4):041017, 2020.

[34] Josh M Deutsch. Quantum statistical mechanics in a closed system. *Physical Review A*, 43(4):2046, 1991.

[35] Mark Srednicki. Chaos and quantum thermalization. *Physical Review E*, 50(2):888, 1994.

[36] Marcos Rigol, Vanja Dunjko, and Maxim Olshanii. Thermalization and its mechanism for generic isolated quantum systems. *Nature*, 452(7189):854–858, 2008.

[37] Fausto Borgonovi, Felix M Izrailev, Lea F Santos, and Vladimir G Zelevinsky. Quantum chaos and thermalization in isolated systems of interacting particles. *Physics Reports*, 626:1–58, 2016.

[38] Luca D'Alessio, Yariv Kafri, Anatoli Polkovnikov, and Marcos Rigol. From quantum chaos and eigenstate thermalization to statistical mechanics and thermodynamics. *Advances in Physics*, 65(3):239–362, 2016.

[39] Joshua M Deutsch. Eigenstate thermalization hypothesis. *Reports on Progress in Physics*, 81(8):082001, 2018.

[40] Hyungwon Kim, Tatsuhiko N Ikeda, and David A Huse. Testing whether all eigenstates obey the eigenstate thermalization hypothesis. *Physical Review E*, 90(5):052105, 2014.

[41] Robin Steinigeweg, Jacek Herbrych, and Peter Prelovšek. Eigenstate thermalization within isolated spin-chain systems. *Physical Review E*, 87(1):012118, 2013.

[42] Wouter Beugeling, Roderich Moessner, and Masudul Haque. Finite-size scaling of eigenstate thermalization. *Physical Review E*, 89(4):042112, 2014.

[43] Nobuyuki Yoshioka Shibata, Naoyuki and Hosho Katsura. Eigenstate thermalization hypothesis and integrability in quantum spin chains. *Physical Review Letters*, 124(18):180604, 2020.

[44] Naoto Shiraishi and Takashi Mori. Systematic construction of counterexamples to the eigenstate thermalization hypothesis. *Physical review letters*, 119(3):030601, 2017.

[45] Eugene P Wigner. On the distribution of the roots of certain symmetric matrices. *Annals of Mathematics*, pages 325–327, 1958.

[46] Eugene P Wigner. Characteristic vectors of bordered matrices with infinite dimensions i. In *The Collected Works of Eugene Paul Wigner*, pages 524–540. Springer, 1993.

[47] Oriol Bohigas, Marie-Joya Giannoni, and Charles Schmit. Characterization of chaotic quantum spectra and universality of level fluctuation laws. *Physical review letters*, 52(1):1, 1984.

[48] Michael Victor Berry and Michael Tabor. Level clustering in the regular spectrum. *Proceedings of the Royal Society of London. A. Mathematical and Physical Sciences*, 356(1686):375–394, 1977.

[49] Vadim Oganesyan and David A Huse. Localization of interacting fermions at high temperature. *Physical review b*, 75(15):155111, 2007.

[50] YY Atas, Eugene Bogomolny, O Giraud, and G Roux. Distribution of the ratio of consecutive level spacings in random matrix ensembles. *Physical review letters*, 110(8):084101, 2013.

[51] Christopher J Turner, Alexios A Michailidis, Dmitry A Abanin, Maksym Serbyn, and Zlatko Papić. Weak ergodicity breaking from quantum many-body scars. *Nature Physics*, 14(7):745–749, 2018.

[52] Cheng-Ju Lin and Olexei I. Motrunich. Exact quantum many-body scar states in the rydberg-blockaded atom chain. *Phys. Rev. Lett.*, 122:173401, Apr 2019.

[53] Thomas Iadecola and Michael Schecter. Quantum many-body scar states with emergent kinetic constraints and finite-entanglement revivals. *Physical Review B*, 101(2):024306, 2020.

[54] Michael Schecter and Thomas Iadecola. Weak ergodicity breaking and quantum many-body scars in spin-1 x y magnets. *Physical review letters*, 123(14):147201, 2019.

[55] Sambuddha Chattopadhyay, Hannes Pichler, Mikhail D Lukin, and Wen Wei Ho. Quantum many-body scars from virtual entangled pairs. *Physical Review B*, 101(17):174308, 2020.

[56] Vincenzo Alba. Onsager's scars in disordered spin chains. *Physical Review B*, 91(15):155123, 2015.

[57] Hongzheng Zhao, Joseph Vovrosh, Florian Mintert, and Johannes Knolle. Quantum many-body scars in optical lattices. *Physical Review Letters*, 124(16):160604, 2020.

[58] Andreas Klümper. Integrability of quantum chains: theory and applications to the spin-1/2 xxz chain. *Quantum magnetism*, pages 349–379, 2004.

[59] AS De Wijn, B Hess, and BV Fine. Lyapunov instabilities in lattices of interacting classical spins at infinite temperature. *Journal of Physics A: Mathematical and Theoretical*, 46(25):254012, 2013.

[60] John Z Imbrie. On many-body localization for quantum spin chains. *Journal of Statistical Physics*, 163(5):998–1048, 2016.

[61] Sandro Wimberger. Nonlinear dynamics and quantum chaos. *Series: Graduate Texts in Physics (Cham: Springer)*, 2014.

[62] Astrid S de Wijn, B Hess, and BV Fine. Largest Lyapunov exponents for lattices of interacting classical spins. *Physical review letters*, 109(3):034101, 2012.

[63] Wm G Hoover, Harald A Posch, Christina Forster, Christoph Dellago, and Mary Zhou. Lyapunov modes of two-dimensional many-body systems; soft disks, hard disks, and rotors. *Journal of Statistical Physics*, 109(3-4):765–776, 2002.

[64] Vito Latora, Andrea Rapisarda, and Stefano Ruffo. Lyapunov instability and finite size effects in a system with long-range forces. *Physical review letters*, 80(4):692, 1998.

[65] Ch Dellago and HA Posch. Kolmogorov-Sinai entropy and Lyapunov spectra of a hard-sphere gas. *Physica A: Statistical Mechanics and its Applications*, 240(1-2):68–83, 1997.

[66] Andrei E Tarkhov, Sandro Wimberger, and Boris V Fine. Extracting Lyapunov exponents from the echo dynamics of Bose-Einstein condensates on a lattice. *Physical Review A*, 96(2):023624, 2017.

[67] Boris V Fine. Typical state of an isolated quantum system with fixed energy and unrestricted participation of eigenstates. *Physical Review E*, 80(5):051130, 2009.

[68] Tarek A Elsayed, Benjamin Hess, and Boris V Fine. Signatures of chaos in time series generated by many-spin systems at high temperatures. *Physical Review E*, 90(2):022910, 2014.

[69] Anatoly Dymarsky. Mechanism of macroscopic equilibration of isolated quantum systems. *Physical Review B*, 99(22):224302, 2019.

[70] The r-value defined in Ref. [50] is equal to $r_{L=12} = 0.5474$, while, for the Gaussian Orthogonal Ensemble, it is $r_{\mathrm{GOE}} = 0.5359$, and for the Poisson Ensemble, it is $r_{\mathrm{P}} = 0.3862$.

[71] Jochen Gemmer, Mathias Michel, and Günter Mahler. *Quantum thermodynamics: Emergence of thermodynamic behavior within composite quantum systems*, volume 784. Springer, 2009.

[72] MI Dykman and IB Schwartz. Large rare fluctuations in systems with delayed dissipation. *Physical Review E*, 86(3):031145, 2012.

[73] Hyungwon Kim and David A Huse. Ballistic spreading of entanglement in a diffusive nonintegrable system. *Physical review letters*, 111(12):127205, 2013.

[74] Matteo Paris and Jaroslav Rehacek. *Quantum state estimation*, volume 649. Springer Science & Business Media, 2004.

[75] John J Bollinger, Wayne M Itano, David J Wineland, and Daniel J Heinzen. Optimal frequency measurements with maximally correlated states. *Physical Review A*, 54(6):R4649, 1996.

[76] Boris V Fine, Tarek A Elsayed, Chahan M Kropf, and Astrid S de Wijn. Absence of exponential sensitivity to small perturbations in nonintegrable systems of spins 1/2. *Physical Review E*, 89(1):012923, 2014.

[77] H Dieter Zeh. On the interpretation of measurement in quantum theory. *Foundations of Physics*, 1(1):69–76, 1970.

[78] H Dieter Zeh. Toward a quantum theory of observation. *Foundations of Physics*, 3(1):109–116, 1973.

[79] Wojciech H Zurek. Pointer basis of quantum apparatus: Into what mixture does the wave packet collapse? *Physical review D*, 24(6):1516, 1981.

[80] Wojciech H Zurek. Environment-induced superselection rules. *Physical review D*, 26(8):1862, 1982.

[81] Eric Joos and H Dieter Zeh. The emergence of classical properties through interaction with the environment. *Zeitschrift für Physik B Condensed Matter*, 59(2):223–243, 1985.

[82] Maximilian A Schlosshauer. *Decoherence: and the quantum-to-classical transition*. Springer Science & Business Media, 2007.

[83] Oleg Lychkovskiy. Dependence of decoherence-assisted classicality on the way a system is partitioned into subsystems. *Physical Review A*, 87(2):022112, 2013.

[84] Oleg Lychkovskiy. Entanglement, decoherence and thermal relaxation in exactly solvable models. In *Journal of Physics: Conference Series*, volume 306, page 012028. IOP Publishing, 2011.

[85] Bassano Vacchini and Klaus Hornberger. Quantum linear Boltzmann equation. *Physics Reports*, 478(4-6):71–120, 2009.

[86] Stephen M Barnett, Sonja Franke-Arnold, Aidan S Arnold, and Colin Baxter. Coherence length for a trapped Bose gas. *Journal of Physics B: Atomic, Molecular and Optical Physics*, 33(19):4177, 2000.

[87] Sonja Franke-Arnold, Guillaume Huyet, and Stephen M Barnett. Measures of coherence for trapped matter waves. *Journal of Physics B: Atomic, Molecular and Optical Physics*, 34(5):945, 2001.

[88] Michael R Gallis and Gordon N Fleming. Environmental and spontaneous localization. *Physical Review A*, 42(1):38, 1990.

[89] L Amico, M Boshier, G Birkl, Anna Minguzzi, C Miniatura, L-C Kwek, D Aghamalyan, V Ahufinger, D Anderson, Natan Andrei, et al. Roadmap on atomtronics: State of the art and perspective. *AVS Quantum Science*, 3(3):039201, 2021.

[90] Sanjay Moudgalya, Nicolas Regnault, and B Andrei Bernevig. η-pairing in hubbard models: From spectrum generating algebras to quantum many-body scars. *Physical Review B*, 102(8):085140, 2020.

[91] Cheng-Ju Lin, Anushya Chandran, and Olexei I Motrunich. Slow thermalization of exact quantum many-body scar states under perturbations. *Physical Review Research*, 2(3):033044, 2020.